

ALMA MATER STUDIORUM – UNIVERSITÀ DI BOLOGNA

**DOTTORATO DI RICERCA IN
CHIMICA**

Ciclo XXXI

Settore Concorsuale: 03/B1

Settore Scientifico Disciplinare: CHIM/03

**EXPLORING THE STRUCTURAL LANDSCAPE OF
MOLECULAR MATERIALS: MULTIPLE CRYSTAL FORMS,
SOLID-STATE PROPERTIES AND PATENTING ISSUES**

Presentata da: Oleksii Shemchuk

**Coordinatore Dottorato:
Prof. Aldo Roda**

**Supervisore:
Prof.ssa Fabrizia Grepioni**

Esame finale anno 2019

INDEX

INDEX.....	i
ABSTRACT	iii
LIST OF ABBREVIATIONS AND ACRONYMS.....	iv
LIST OF SCHEMES, FIGURES AND TABLES	v
1. CHAPTER I - INTRODUCTION.....	1
1.1. Crystal engineering.....	1
1.2. Polymorphism	7
1.3. Multicomponent systems.....	9
1.4. Methods and techniques used for the characterization of solid products:.....	13
1.5. References.....	15
2. CHAPTER II - MOLECULAR SOLID SOLUTIONS.....	18
2.1. Overview	18
2.2. Alloying barbituric and thiobarbituric acids: from solid solutions to a highly stable keto co-crystal form	22
2.2.1. Supporting Information.....	23
2.3. References.....	34
3. CHAPTER III - IONIC CO-CRYSTALS.....	35
3.1. Overview	35
3.2. Ionic co-crystals of cyanuric acid with alkali halides	38
3.2.1. Introduction.....	38
3.2.2. Anhydrous ionic co-crystals of cyanuric acid with LiCl and NaCl.....	42
3.2.2.1. Supplementary Information.....	43
3.2.3. Ionic co-crystals of cyanuric acids with the rest of alkali halides.....	48
3.2.4.1 Supporting Information.....	58
3.2.4. Conclusions.....	72
3.3. Mechanochemical preparation of molecular and ionic co-crystals of the hormone melatonin	73
3.3.1. Overview	73
3.3.2. Introduction.....	73
3.3.3. Experimental part.....	76
3.3.4. Results and Discussion	79
3.3.5. Supporting information.....	86
3.3.6. Conclusions.....	95
3.4. Exploring chiral resolution in the solid-state via ionic co-crystal formation.....	96

3.4.1.	Ionic Co-crystals of Racemic and Enantiopure Histidine: An Intriguing Case of Homochiral Preference	98
3.4.2.	Ionic Co-crystals of Racemic and Enantiopure Histidine: An Intriguing Case of Homochiral Preference	100
3.4.3.	Ionic Co-crystal Formation as a Path Towards Chiral Resolution in the Solid State	102
3.4.4.	Solid-state chiral resolution mediated by stoichiometry: crystallizing etiracetam with ZnCl ₂	104
3.4.4.1	Supplementary Information	106
4.	SUMMARY	126
4.1.	Investigation of solid solutions consisting of organic molecules	126
4.2.	Co-crystallization as a tool to modify physicochemical properties of interest.....	127
4.3.	The effect of co-crystallization on chirality and its possible application for chiral resolution.	128
	ACKNOWLEDGMENT	viii

ABSTRACT

The concept of crystal engineering is *making crystals with a purpose* and it is an indisputable fact that multicomponent molecular solids such as co-crystals, metal-organic frameworks (MOFs), and solid solutions are at the forefront of crystal engineering research. Multicomponent crystalline systems are important targets in the quest for novel solid forms that can show improvement of physical and chemical properties (solubility, intrinsic dissolution rate, morphology, thermal and hydration stability, etc.) compared to those of the parent components. As a result, multicomponent solids can find application in a variety of industrial fields.

The research activity performed in my PhD was mainly dedicated to the investigations of multicomponent crystalline assemblies, namely molecular and ionic co-crystals and molecular solid solutions. The project can be subdivided into the following topics:

1. Investigation of solid solutions consisting of organic molecules.
2. Co-crystallization as a tool to modify physicochemical properties of interest.
3. The effect of co-crystallization on chirality and its possible application for chiral resolution.

The first two parts of the project were focused on the search for novel multicomponent crystalline assemblies capable of modifying the physicochemical properties of interest: thermostability for the obtained molecular solid solutions and enhancement of the solubility and intrinsic dissolution rate characteristics for the ionic co-crystals. The final chapter of this project was dedicated to the investigation of the influence of co-crystallization of chiral molecules of pharmaceutical interest with inorganic salts.

LIST OF ABBREVIATIONS AND ACRONYMS

API(s) – Active Pharmaceutical Ingredient(s)

BA – Barbituric Acid

CA – Cyanuric Acid

CSD – Cambridge Structural Database

DABCO - 1,4-DiAzaBiCyclo[2.2.2]Octane

DSC – Differential Scanning Calorimetry

FDA – Food and Drug Administration

GRAS – Generally Regarded As Safe

HSM – Hot-Stage Microscopy

ICC(s) – Ionic Co-Crystal(s)

IDR – Intrinsic Dissolution Rate

SC XRD – Single Crystal X-Ray Diffraction

TBA – ThioBarbituric Acid

TCA – Trithiocyanuric Acid

TGA – Thermal Gravimetric Analysis

TPD – Ternary Phase Diagram

VT XRPD – Variable Temperature X-Ray Powder Diffraction

XRPD – X-Ray Powder Diffraction

LIST OF SCHEMES, FIGURES AND TABLES

Scheme 1.1-1	<i>Supramolecular synthons formed via hydrogen bonds.</i>	3
Scheme 1.1-2	<i>Typical halogen bond motifs in supramolecular synthons. X = Br/I.</i>	6
Figure 1.1-1	<i>Schematic representation of the structural relationship between polymorphs, hydrates, solvates, co-crystals, salts, amorphous and solid solutions.</i>	7
Figure 2.1-1	<i>o-methylbenzoic and o-chlorobenzoic acids (top) and the disordered co-crystal formed by their interaction (bottom)</i>	19
Figure 2.1-2	<i>Compounds used for the preparation of binary and ternary solid solutions.</i>	21
Figure 2.1-3	<i>a) Barbituric acid (BA); b) Thiobarbituric acid (TBA); c) Cyanuric acid (CA); d) Trithiocyanuric acid (TCA).</i>	21
Figure 3.2.1-1	<i>a) Barbituric acid (BA); b) Thiobarbituric acid (TBA); c) Cyanuric acid (CA); d) Trithiocyanuric acid (TCA).</i>	38
Figure 3.2.1-2	<i>The ionic co-crystal formed by barbituric acid and KBr - BA·KBr·2H₂O</i>	39
Figure 3.2.3-1	<i>XRPD of CA₂·RbCl and CA₂·CsCl</i>	49
Figure 3.2.3-2	<i>CA₂·RbCl. View down crystallographic a-axis (top); hydrogen bonds between CA₂ molecules.</i>	49
Figure 3.2.3-3	<i>CA₂·CsCl. The comparison between XRPD patterns of CA₂·CsCl analysed immediately after being synthesized (red) and in 24h (black).</i>	50
Figure 3.2.3-4	<i>TGA traces of CA·LiBr·nH₂O</i>	52
Figure 3.2.3-5	<i>(a) XRPD of CA·NaCl and CA·NaBr; (b) Na⁺ coordination in CA·NaBr</i>	53
Figure 3.2.3-6	<i>Na⁺ coordination in CA·NaBr·2H₂O.</i>	54
Figure 3.2.3-7	<i>K⁺ coordination in CA·KBr</i>	54
Figure 3.2.3-8	<i>CA·RbBr. View down crystallographic a axis</i>	55
Figure 3.2.3-9	<i>CA·KI·H₂O.</i>	56
Figure 3.2.3-10	<i>XRPD of CA·RbI and CA·KBr</i>	57
Figure 3.2.4.1-1	<i>The crystal packing of CA·RbI.</i>	58
Figure 3.2.4.1-2	<i>CA·CsBr.</i>	59
Figure 3.2.4.1-3	<i>CA₂·CsCl. Some traces of cyanuric acid are present in the XRPD pattern.</i>	59
Figure 3.2.4.1-4	<i>CA·KBr. Some traces of KBr are present in the XRPD pattern.</i>	60
Figure 3.2.4.1-5	<i>CA·NaBr. Some traces of cyanuric acid are present in the XRPD pattern.</i>	60
Figure 3.2.4.1-6	<i>CA·NaBr·2H₂O. Some traces of cyanuric acid are present in the XRPD pattern.</i>	61
Figure 3.2.4.1-7	<i>CA·RbBr. Some traces of RbBr are present in the XRPD pattern.</i>	61
Figure 3.2.4.1-8	<i>CA₂·RbCl, Some traces of RbCl are present in the XRPD pattern.</i>	62
Figure 3.2.4.1-9	<i>CA·RbI</i>	62
Figure 3.2.4.1-10	<i>DSC trace for cyanuric acid.</i>	63
Figure 3.2.4.1-11	<i>DSC trace for CA₂·RbCl.</i>	63
Figure 3.2.4.1-12	<i>DSC trace for CA₂·CsCl</i>	64
Figure 3.2.4.1-13	<i>DSC trace for CA·NaBr·2H₂O.</i>	64
Figure 3.2.4.1-14	<i>DSC trace for CA·NaBr</i>	65
Figure 3.2.4.1-15	<i>DSC trace for CA·KBr.</i>	65
Figure 3.2.4.1-16	<i>DSC trace for CA·RbBr.</i>	66
Figure 3.2.4.1-17	<i>DSC trace for CA·CsBr.</i>	66
Figure 3.2.4.1-18	<i>DSC trace for CA·NaI.</i>	67
Figure 3.2.4.1-19	<i>DSC trace for CA·NaI.</i>	67
Figure 3.2.4.1-20	<i>TGA trace for CA₂·RbCl.</i>	68
Figure 3.2.4.1-21	<i>TGA trace for CA₂·CsCl.</i>	68
Figure 3.2.4.1-22	<i>TGA trace for CA·NaBr·2H₂O.</i>	69
Figure 3.2.4.1-23	<i>TGA trace for CA·NaBr.</i>	69
Figure 3.2.4.1-24	<i>TGA trace for CA·KBr.</i>	700
Figure 3.2.4.1-25	<i>TGA trace for CA·RbBr.</i>	70
Figure 3.2.4.1-26	<i>TGA trace for CA·CsBr.</i>	71
Figure 3.2.4.1-27	<i>TGA trace for CA·RbI.</i>	71
Figure 3.3.2-1	<i>Melatonin.</i>	75

Figure 3.3.4-1	<i>HB-pattern in crystalline melatonin.....</i>	<i>80</i>
Figure 3.3.4-2	<i>The DABCO (a) and piperazine (b) molecules bridge pairs of melatonin molecules via hydrogen bonds of the $N\cdots(H)N_{\text{melatonin}}$ type.....</i>	<i>82</i>
Figure 3.3.4-3	<i>The coordination of melatonin, water molecules (blue) and chlorides to Ca^{2+}.....</i>	<i>83</i>
Figure 3.3.4-4	<i>The crystal packing of $mel_2\cdot CaCl_2\cdot 2H_2O$. Top: view along the c-axis; bottom: layer, view along the a-axis.....</i>	<i>84</i>
Figure 3.3.4-5	<i>Comparison of the solubility in water at 293 K for melatonin and the ionic co-crystal $mel_2\cdot CaCl_2\cdot 2H_2O$, in $g\cdot L^{-1}$ (left) and in $mol\cdot L^{-1}$ (right).</i>	<i>85</i>
Figure 3.3.5-1	<i>TGA of melatonin.....</i>	<i>86</i>
Figure 3.3.5-2	<i>DSC of melatonin.</i>	<i>86</i>
Figure 3.3.5-3	<i>TGA of $mel_2\cdot DABCO$.</i>	<i>87</i>
Figure 3.3.5-4	<i>DSC of $mel_2\cdot DABCO$.....</i>	<i>87</i>
Figure 3.3.5-5	<i>TGA of $mel_2\cdot pip$.....</i>	<i>88</i>
Figure 3.3.5-6	<i>DSC of $mel_2\cdot pip$.</i>	<i>88</i>
Figure 3.3.5-7	<i>TGA of $mel_2\cdot CaCl_2\cdot 2H_2O$.</i>	<i>89</i>
Figure 3.3.5-8	<i>DSC of $mel_2\cdot CaCl_2\cdot 2H_2O$. XRPD: comparison between reagents and products</i>	<i>89</i>
Figure 3.3.5-9	<i>XRPD comparison between $mel_2\cdot DABCO$ and starting materials.</i>	<i>90</i>
Figure 3.3.5-10	<i>XRPD comparison between $mel_2\cdot pip$ and starting materials.</i>	<i>90</i>
Figure 3.3.5-11	<i>Comparison between the XRPD patterns of the $mel_2\cdot pip$ and $mel_2\cdot DABCO$ co-crystals.</i>	<i>91</i>
Figure 3.3.5-12	<i>XRPD comparison between $mel_2\cdot CaCl_2\cdot 2H_2O$ and starting materials.</i>	<i>91</i>
Figure 3.3.5-13	<i>Rietveld refinement of $mel_2\cdot CaCl_2\cdot 2H_2O$.</i>	<i>92</i>
Figure 3.3.5-14	<i>Rietveld refinement of $mel_2\cdot pip$.</i>	<i>92</i>
Table 3.2.1-1	<i>Mechanochemical preparation of ICCs of CA with alkali halides.....</i>	<i>40</i>
Table 3.2.4.1-1	<i>Structural data for ICCs solved from XRPD data.</i>	<i>58</i>
Table 3.3.3-1	<i>Structural data for melatonin co-crystals and ionic co-crystals.</i>	<i>77</i>
Table 3.3.5-1	<i>Organic acids.</i>	<i>93</i>
Table 3.3.5-2	<i>Amino acids.</i>	<i>93</i>
Table 3.3.5-3	<i>Inorganic salts.</i>	<i>93</i>
Table 3.3.5-4	<i>Phenols.</i>	<i>94</i>
Table 3.3.5-5	<i>Nitrogen containing compounds.</i>	<i>94</i>
Table 3.3.5-6	<i>Various.....</i>	<i>95</i>

1. CHAPTER I - INTRODUCTION

1.1. Crystal engineering

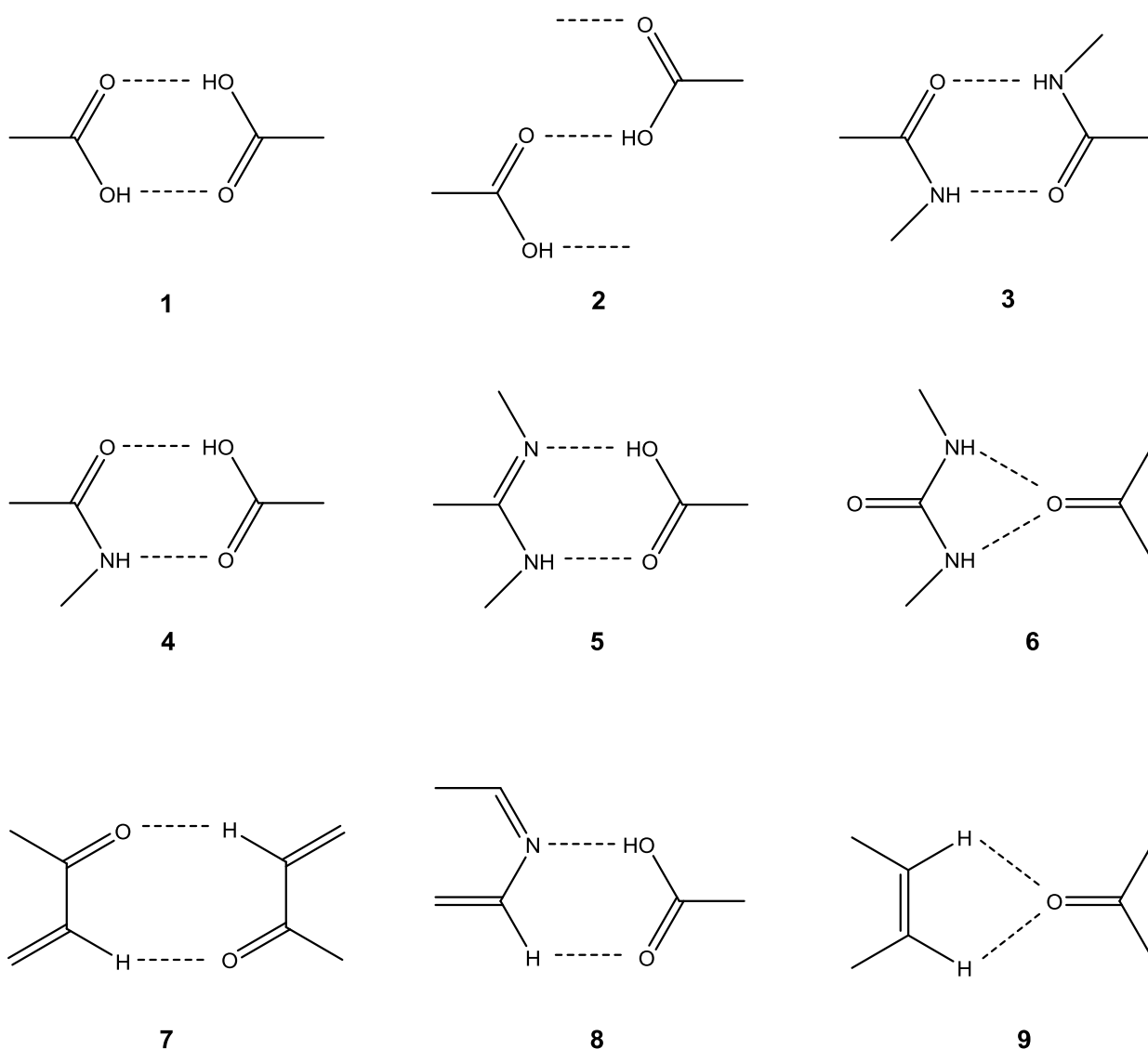
Crystal engineering has been defined by Desiraju in 1989 as “*the understanding of intermolecular interactions in the context of crystal packing and in the utilisation of such understanding in the design of new solids with desired physical and chemical properties*”.¹ Substantially, crystal engineering is a powerful tool to gain control on the arrangement of the molecules/ions in the solid state via non-covalent interactions such as hydrogen and halogen bonding, as well as ionic, van der Waals and π -interactions.² Obviously, the solid-state packing arrangement of the building blocks (molecular and/or ionic) can dramatically affect the materials properties. Thus, the scientists in the field of crystal engineering aim at the development of the solids with the desired properties using the knowledge of the properties of their components. This rather challenging goal can be achieved via understanding and/or prediction of the spatial distribution and intermolecular interactions of the components in the solid.

Apparently, most materials that find some practical application are crystalline solids. Crystals *per se* are supramolecular entities composed of molecular and/or ionic building blocks. According to Dunitz: “*A crystal is, in a sense, the supramolecule par excellence: a lump of matter, of macroscopic dimensions, millions of molecules long, held together in a periodic arrangement by just the same kind of interactions as are responsible for molecular recognition and complexation at all levels - ion-ion, ion-dipole, dipole-dipole interactions, hydrogen bonding, London forces, and so on*”.³ This defines a crystal as a “*supramolecule*”- an assembly of molecules via mutual recognition. The molecules are composed of atoms connected via covalent bonds, whereas the

molecules/ions making up such a “*supramolecule*” are held together via intermolecular interactions.⁴ Consequently, “*making crystals by design*”⁵ has become the paradigm of crystal engineering. Crystal engineering, as such, can be considered as a subject at the intersection of materials science and supramolecular chemistry.⁵ Supramolecular chemistry has been defined as a science “*beyond the chemistry of the molecule*” or as “*the chemistry of the intermolecular bond*”.⁶

In fact, the process of crystal making essentially resembles the classical chemical experiments for the development of a new molecule: the modelling of a molecule, development of the most appropriate synthetic route, characterization of the obtained products, assessment of its properties.⁵ The crystal making process also requires the existence of a project – a goal for the formulation of new crystalline materials, the elaboration of a suitable design strategy, characterization of the obtained materials and the evaluation of its performance.^{5, 7} In addition, in organic synthesis a retrosynthetic approach is employed to develop a synthetic strategy.⁸ The idea of this approach is to simplify the molecular structure into basic units – synthons^{8, 9} that could be used as a synthetic tool in the synthesis of complex organic molecules. In the crystal making process, in turn, “*supramolecular synthons*” are typically involved. Desiraju defined supramolecular synthons as “*structural units within supermolecules which can be formed and/or assembled by known or conceivable synthetic operations involving intermolecular interactions*”.⁴ Put it differently, supramolecular synthons are spatial arrangements of intermolecular interactions and the main goal of crystal engineering is to recognize and to use them wisely in the design of materials.¹⁰ Scheme 1.1-1 represents several examples of supramolecular synthons formed via hydrogen bonding.^{4, 11, 12} Synthons **1-3** are homosynthons exhibited by carboxylic acid (**1** and **2**) and amide dimers (**3**), correspondingly. Synthons **1** and **2** show the possibility of different arrangements of the same

chemical group. Synthons **4-6** are examples of heterosynthons. Synthons **1-6** have strong C=O...H-O; N-H...O; and O-H...N interactions. Synthons **7-9** are less favoured synthon with either one weak C-H...O=C and one strong O-H...N (**8**) or both weak C-H...O=C hydrogen bonds (**7** and **9**).



Scheme 1.1-1 Supramolecular synthons formed via hydrogen bonds.

Hydrogen bonding the most frequently occurring noncovalent interaction in recognition processes.¹³ Etter has defined hydrogen bond as “an interaction that directs the association of a covalently bound hydrogen atom with one or more

other atoms, groups of atoms, or molecules into an aggregate structure that is sufficiently stable to make it convenient for the chemist to consider it as an independent chemical species"¹⁴. Hydrogen bonds can be either intermolecular - between molecules or intramolecular when the interaction takes place within different parts of a single molecule. The energy of a hydrogen bond depends on a number of parameters such as the nature of the donor and acceptor atoms which constitute the bond, their geometry, and environment.¹⁵ The energy of a hydrogen bond can vary between 0.2 and 40 kcal/mol.¹⁵ Based on the energies of hydrogen bonds they can be subdivided into three groups: weak hydrogen bonds (the energy is less than 4 kcal/mol), moderate (4-15 kcal/mol) and strong (>15 kcal/mol).¹⁶ The importance of weak and moderate hydrogen bonds should not be underestimated since they can play a significant role in the landscape of the non-covalent interactions in the lack of strong hydrogen bonds. To the most typically observed weak hydrogen bonds belong such interactions as C-H...N, C-H...O, C-H...X (X= Cl, F), and N-H...π.¹⁷ This fact indicates that a hydrogen bond is to some extent stronger than a van der Waals interaction, but it is weaker than covalent or ionic bonds.

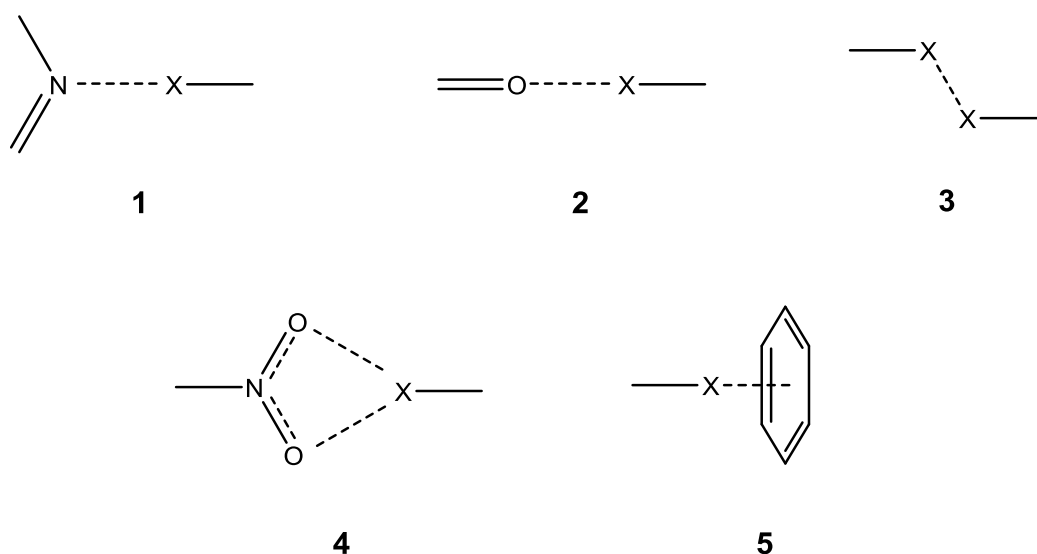
One more important aspect that influences the strength of a hydrogen bond is the pKa values of both hydrogen bond donor and acceptor.¹⁸⁻²⁰ If the ionic charge is present on the donor and acceptor of a hydrogen bond, the electrostatic dipole-dipole component of hydrogen bonding is enhanced. The hydrogen bonds of this type are called "*Charge Assisted hydrogen Bonds*"²¹⁻²³ They are usually obtained via proton transfer in acid-base reactions. "*Charge-Assisted Hydrogen Bonds*" integrate the directionality of a hydrogen bond with the strength of Coulombic forces.

It is an inevitable fact that hydrogen bonds being both an electrostatic and a directional interaction play a crucial role in crystal engineering.^{16, 24-26} However,

this is not the only type of interactions that can be used in the construction of new crystalline solids. Halogen atoms can work as acceptor sites resulting in the interaction called halogen bonding.^{13, 27, 28}

According to Metrangolo *et al.* "a halogen bond occurs when there is evidence of a net attractive interaction between an electrophilic region associated with a halogen atom in a molecular entity and a nucleophilic region in another, or the same, molecular entity".²⁹ Thus, halogen bonding is a particular non-covalent interaction in which a halogen atom acts as electrophilic species with electron donors.²⁷

Like hydrogen bonds, halogen bonds can be also used to control recognition, self-assembly, and aggregation processes in the solid.²⁷ The energies of halogen bonds are dependent on the interacting partners and vary significantly from ~2.5 kcal/mol for weak interactions (for instance N...Cl contacts³⁰) to ~36 kcal/mol – the very strong interaction (in the I₂...I⁻ adduct³¹).²⁸ The notable energies of certain halogen bonds allow these interactions to prevail over other non-covalent interactions such as dipole-dipole interactions, π-π stacking, etc.³² Halogen bonds are particularly directional interactions.³³ Some of the most common halogen bond synthons are given in scheme 1.1-2.^{34, 35}



Scheme 1.1-2 Typical halogen bond motifs in supramolecular synthons. X = Br/I.

The understanding of all the possible intra- and intermolecular interactions does not guarantee the predictability of the outcome of a crystallization process. Especially, the prediction becomes more difficult if more than one molecular and/or ionic building block is involved in the crystallization process. Figure 1.1-1 represents the possible outcomes. The crystallization may result in the formation of an amorphous product, polymorphs^{11, 26, 36-38}, hydrates^{37, 38}, solvates^{37, 38}, salts, molecular³⁹⁻⁴² or ionic⁴³⁻⁴⁵ co-crystals, and solid solutions.⁴⁶⁻⁴⁹

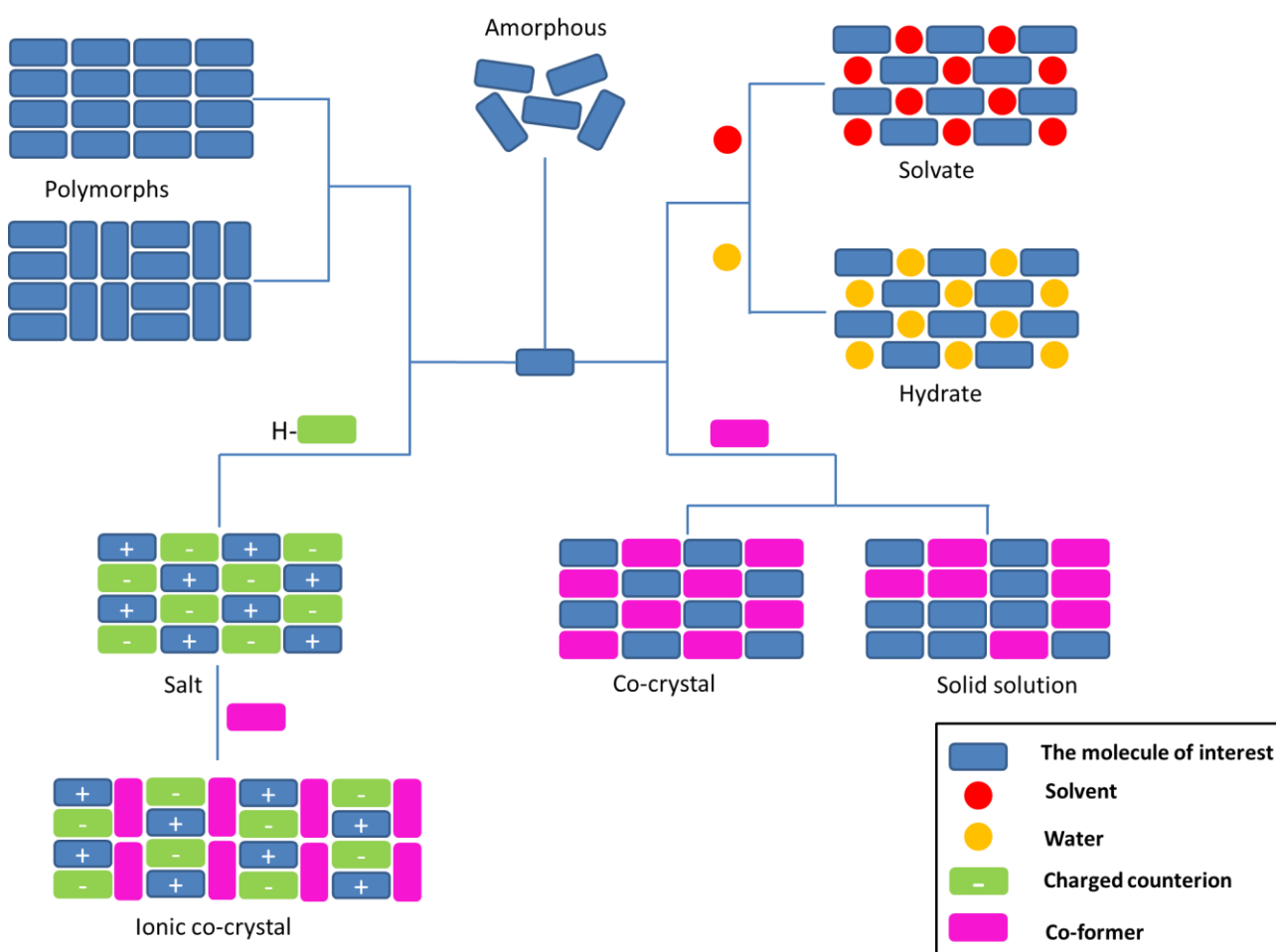


Figure 2.2.1-1 Schematic representation of the structural relationship between polymorphs, hydrates, solvates, co-crystals, salts, amorphous and solid solutions.

1.2. Polymorphism

The fundamental physicochemical properties of crystalline materials depend on the arrangement of the molecular/ionic building blocks within the solid. Consequently, changing the disposition and/or interactions between these components can have a direct influence on the properties of the particular solid.⁵⁰

In attempt to improve the solid-state properties of a given compound, the scientists working in the field of molecular crystal engineering have always been interested in such a phenomenon as crystal polymorphism: the ability of a solid material to exist in multiple forms or crystal structures⁵¹. Having different structures polymorphs can possess different thermal, solubility, optical and electrical properties. The search for the solid form landscapes of molecules of interest is typically aimed to determine the crystalline form(s) performing predictably at the given conditions.³⁸ Industry is always interested in robust process development and usually gives preference to the most thermodynamically stable form that can be manufactured consistently.⁵² Currently, the computational prediction is not capable of foretelling the exact number of observable polymorphic forms of even the simplest molecules.⁵³ Therefore, for the search of new polymorphs high-throughput screening methods are commonly used.⁵⁴ Normally various crystallization techniques are used to search for all the possible solid forms of the investigated compounds (polymorphs, hydrates, and solvates) and afterwards the most stable crystal form is determined.⁵⁵ Unfortunately, even enormous efforts invested into a properly elaborated and implemented screening test do not guarantee that a new crystal form will not suddenly emerge afterwards.⁵¹ And sometimes the unexpected discovery of such a form can create a lot of problems for the manufacturer since its physicochemical properties might be significantly different from the produced form. The lack of predictability of formation of new polymorphs, hydrates and

solvates can be explained by insufficient level of comprehension of the mechanisms of nucleation and crystal growth.⁵⁶

However, the existence of more than one polymorphic form of the investigated compound can be of use for the industry. Since the phenomenon of polymorphism is not predictable, it meets all the requirements of a patent: novelty, non-obviousness, and usefulness for the industrial application.⁵⁷⁻⁶⁰ Due to this fact, polymorphism has recently become the principal investigation area for the solid-state scientific community in the pharmaceutical, agrochemical and pigment industries.^{11, 58, 61-64}

The extent of polymorphism of the compound of interest is limited to the handful of its various crystalline forms.⁶⁵ Despite the fact that different polymorphic forms can vary in some physicochemical properties this variation rate is limited due to the presence of only one component.⁶⁶ However, in some cases even relatively minor changes can have a crucial effect on a particular property of the investigated compound. Perhaps, the most famous case of the effect of polymorphism is the case of about the Norvir® (ritonavir) – antiretroviral medication used to treat AIDS.⁶⁷ In the development process of this drug only one polymorphic form was found. However, during the dissolution tests some lots of capsules showed much lower solubility characteristics. As it was found out, this phenomenon was caused by a “spontaneous” appearance of a more stable polymorphic form.⁶⁸ As a result, the medication was removed from the market causing the loss of millions of dollars and heavy consequences on patients.⁶⁹ After this dramatic case took place polymorphism has become a serious concern for the pharmaceutical industry.⁷⁰

1.3. Multicomponent systems

Multicomponent crystalline assemblies are relevant targets in the quest for novel solid forms exhibiting enhancement of physicochemical properties such as solubility, intrinsic dissolution rate, morphology, thermal and hydration stability compared to those of the separate components. Due to their potential to tune these crucial properties, multicomponent crystalline solids are of interest in a variety of applications (pharmaceuticals, pigments, high energetic materials, nutraceuticals, agrochemicals, cosmetics etc.).⁷¹⁻⁷⁴ To date, solid-state chemists can employ a number of strategies to modify the chemical and physical solid-state properties of materials of interest (see fig. 1.1-1): the formation of polymorphs, salts, hydrates, solvates, molecular and ionic co-crystals, and solid solutions.⁵⁰ The use of multicomponent systems can provide a large variety of constituents in the solid form and each of them has a direct impact on the properties of the particular solid.⁵⁰

The most well-established approach in the formulation of a new multicomponent crystalline solid with enhanced physicochemical properties is the formation of a salt.⁷⁵⁻⁷⁸ The main limitation of salts is that the compound of interest must contain ionizable (basic or acidic) moieties.^{79, 80} A different pathway can be the formation of a co-crystal.^{36, 40, 50, 81, 82} The exact definition of a co-crystal is still a matter of debate.^{41, 42, 82} However, there are, at least, three broad commonalities that are agreed upon by the majority of the scientists working in the field of crystal engineering.⁴⁰ First, co-crystals are constructed from discrete neutral molecular species. This statement excludes all solids containing ions, namely salts and complexes of transition-metal ions. Second, co-crystals are constituted of reagents that are solids at ambient conditions. This assertion allows to distinguish co-crystals from solvates and hydrates as well as from clathrates or inclusion compounds with a solvent/gas molecule as a guest component.⁴⁰ Finally, the

components of co-crystals should be present in well-defined stoichiometric amounts forming structurally homogeneous crystalline solids.⁴⁰ This statement allows drawing a borderline between co-crystals and solid solutions. The main advantage of co-crystals over salts is the fact that, in principle, any molecule could potentially form a co-crystal regardless of the presence of any ionizable moieties in its structure.⁵⁰

Depending on the nature of a co-former, the co-crystals can be divided into “molecular” or “ionic”.⁷⁶ The former are composed of at least two neutral co-formers in a stoichiometric ratio. The components of such a co-crystal are typically held together by hydrogen and/or halogen bonds and π - π stacking. The term “ionic co-crystal” (ICC) was introduced by our research group.⁴³ Initially the term was used to define the co-crystals formed by a neutral organic molecule and an inorganic salt of a non-transition metal. The main interactions in such organic–inorganic systems are those established by metal cations with the organic moieties (typically, oxygen or nitrogen atoms donate electrons towards the metal cation). The anions, typically but not exclusively halides, form hydrogen bonds with the hydrogen donor groups on the organic moieties.⁴⁴ The interactions of ions with the organic molecules resemble the ones between solvent and ions in solution or in solid solvates.⁴³ These ICCs could be considered as complexes of organic type ligands and metal cations.⁴⁴

To date, the use of this term has been extended towards the co-crystals of neutral molecules with organic or organic-inorganic salts.⁴⁴ Generally speaking, ICCs do not meet the requirements of the co-crystals mentioned above since one of the co-formers is not neutral. However, they do not meet the requirements of the salts either since no proton transfer took place between the molecule of interest and the co-former. Consequently, the ICCs lie on the borderline between salts and co-crystals. As a result, in the literature we can often meet the compounds of

such a type with different names such as a “*co-crystal of a salt*” of “*salt co-crystal*”.⁸⁰

Even the distinction between a salt and a co-crystal is not always straightforward. Thus, if there is a hydrogen bond between the molecule of interest and the co-former sometimes it is not possible to determine the position of the proton in a base – acid pair system. For instance, in the hydrogen bond formed by a carboxylic group and an amine the position of a proton depends on the relative acid– base strength and, obviously, on the temperature. The main condition for the formation of a salt in the acid-base reaction is that the value of $\Delta pK_a = pK_a(\text{Acid}) - pK_a(\text{Base})$ should be greater than 2 or 3, whereas for $\Delta pK_a < 0$ a co-crystal is generally formed.^{79, 83-86}

An alternative route in the design of crystalline materials with desired properties is to prepare multicomponent systems of variable stoichiometric ratios – solid solutions.^{47, 48, 87-90} These multicomponent solids are considered a useful tool for modifying physicochemical properties.⁹¹⁻⁹³ Crystalline solid solutions or organic alloys can be characterized by a structural disorder that permits the variation of the ratios of their components in continuum.⁴⁹ Consequently, the stoichiometric ratio of solid solutions is not usually limited to an integer or rational number. Since the stoichiometry of the components of such systems can be varied *in continuum*, at least in a certain composition range, taking control over their ratios becomes the crucial aspect not only for a fine tuning of solid-state physicochemical properties, but also for their predictability.⁴⁹ Especially, the continuous variation of the amount of components of a solid solution can impact on the thermal properties. Quite often a solid solution exhibits properties which are between those of the pure components. However, sometimes new unexpected properties can arise.^{49, 87} Solid solutions are good candidates to understand structure – properties relationship. In principle, it should be possible

to follow the change of the physicochemical properties upon varying the stoichiometric ratio of the components.

Unlike co-crystals which can be formed by a virtually infinite amount of molecular and/or ionic building blocks, solid solutions required a number of prerequisites. In this respect, the similarity in chemical structure and, preferably, in supramolecular arrangement in the crystals of a single component is typically the major precondition to obtain a solid solution.^{47, 48, 89, 90} If the molecules are quite similar in size and shape, there is a chance that they can become miscible in a range of compositions.²

1.4. Methods and techniques used for the characterization of solid products:

- Single Crystal X-ray Diffraction (SCXRD), the main technique used for structure determination;
- X-ray Powder Diffraction (XRPD). This technique allowed characterizing the bulk material. In co-crystallization experiments it was mainly used to determine whether the change of the phase took place, whether there were any new peaks different from those of the starting materials and, if so, whether some traces of the starting materials were still present in the bulk. When it was not possible to grow the single crystal of suitable quality to solve the structure using SCXRD, XRPD was applied for this purpose.
- Variable Temperature X-ray Powder Diffraction (VT XRPD). This technique was used to follow the possible changes in the crystalline structure of the investigated solids upon change of the temperature;
- Differential Scanning Calorimetry (DSC), a thermoanalytical technique used to detect phase changes (dehydration/desolvation, polymorphic transition, melting);
- Thermogravimetric Analysis (TGA). This technique applied to quantify the mass loss of the sample upon heating;
- Hot-Stage Microscopy (HSM). The technique which was used for preparation of the crystals from melt and for visual estimation of the effect of the temperature on the investigated solids.
- Intrinsic dissolution rate (IDR) analysis. This technique was used to determine the speed with which the compound is released from the crystal lattice into solution;
- Solubility test. This technique was used to determine the maximum quantity of compounds capable of dissolving in a given amount of solvent.

- Ternary phase diagram (TPD) construction. This technique was used to determine the most thermodynamically stable phase for a given stoichiometric ratio of the molecule of interest, co-former and solvent.

1.5. References

1. G. R. Desiraju and G. W. Parshall, *Materials science monographs*, 1989, **54**.
2. D. Braga, F. Grepioni, L. Maini and S. d'Agostino, *IUCrJ*, 2017, **4**, 369-379.
3. J. D. Dunitz, *Pure Appl. Chem.*, 1991, **63**, 177-185.
4. G. R. Desiraju, *Angew. Chem. Int. Ed.*, 1995, **34**, 2311-2327.
5. D. Braga and F. Grepioni, *Making crystals by design: methods, techniques and applications*, John Wiley & Sons, 2007.
6. J.-M. Lehn, *Angewandte Chemie International Edition in English*, 1988, **27**, 89-112.
7. Z. Zhang and M. J. Zaworotko, *Chem. Soc. Rev.*, 2014, **43**, 5444-5455.
8. E. J. Corey, *Pure Appl. Chem.*, 1967, **14**.
9. E. J. Corey, *Chem. Soc. Rev.*, 1988, **17**, 111-133.
10. N. Blagden, M. de Matas, P. T. Gavan and P. York, *Adv. Drug Del. Rev.*, 2007, **59**, 617-630.
11. B. Moulton and M. J. Zaworotko, *Chem. Rev.*, 2001, **101**, 1629-1658.
12. L. J. Prins, D. N. Reinhoudt and P. Timmerman, *Angew. Chem. Int. Ed.*, 2001, **40**, 2382-2426.
13. P. Metrangolo, H. Neukirch, T. Pilati and G. Resnati, *Acc. Chem. Res.*, 2005, **38**, 386-395.
14. M. C. Etter, *Acc. Chem. Res.*, 1990, **23**, 120-126.
15. T. Steiner, *Angew. Chem. Int. Ed. Engl.*, 2002, **41**, 49-76.
16. G. A. Jeffrey and G. A. Jeffrey, *An introduction to hydrogen bonding*, Oxford university press New York, 1997.
17. D. R. Armstrong, S. Bennett, M. G. Davidson, R. Snaith, D. Stalke and D. S. Wright, *J. Chem. Soc., Chem. Commun.*, 1992, **0**, 262-264.
18. P. Gilli, L. Pretto, V. Bertolasi and G. Gilli, *Acc. Chem. Res.*, 2009, **42**, 33-44.
19. S. o. Shan and D. Herschlag, *Proceedings of the National Academy of Sciences*, 1996, **93**, 14474-14479.
20. C. B. Aakeroy, K. Epa, S. Forbes, N. Schultheiss and J. Desper, *Chem. Eur. J.*, 2013, **19**, 14998-15003.
21. J. Clare Speakman, 1972, **12**, 141-199.
22. S. J. Grabowski, *J. Mol. Model.*, 2013, **19**, 4713-4721.
23. D. Braga, L. Maini, F. Grepioni, A. De Cian, O. Felix, J. Fischer and M. W. Hosseini, *New J. Chem.*, 2000, **24**, 547-553.
24. S. Scheiner, *Hydrogen bonding: a theoretical perspective*, Oxford University Press on Demand, 1997.
25. G. R. Desiraju, *Angew. Chem. Int. Ed.*, 2011, **50**, 52-59.
26. C. B. Aakeröy and K. R. Seddon, *Chem. Soc. Rev.*, 1993, **22**, 397-407.
27. P. Metrangolo, F. Meyer, T. Pilati, G. Resnati and G. Terraneo, *Angew. Chem. Int. Ed.*, 2008, **47**, 6114-6127.
28. G. Cavallo, P. Metrangolo, R. Milani, T. Pilati, A. Priimagi, G. Resnati and G. Terraneo, *Chem. Rev.*, 2016, **116**, 2478-2601.
29. G. R. Desiraju, P. S. Ho, L. Kloo, A. C. Legon, R. Marquardt, P. Metrangolo, P. Politzer, G. Resnati and K. Rissanen, *Pure Appl. Chem.*, 2013, **85**, 1711-1713.
30. K. Xu, D. M. Ho and R. A. Pascal, *J. Am. Chem. Soc.*, 1994, **116**, 105-110.
31. M. Muller, M. Albrecht, V. Gossen, T. Peters, A. Hoffmann, G. Raabe, A. Valkonen and K. Rissanen, *Chem. Eur. J.*, 2010, **16**, 12446-12453.
32. K. Wendler, J. Thar, S. Zahn and B. Kirchner, *J. Phys. Chem. A*, 2010, **114**, 9529-9536.
33. M. Saccone, G. Cavallo, P. Metrangolo, A. Pace, I. Pibiri, T. Pilati, G. Resnati and G. Terraneo, *Crystengcomm*, 2013, **15**, 3102-3105.
34. B. K. Saha, A. Nangia and M. Jaskólski, *CrystEngComm*, 2005, **7**, 355.
35. V. Nemeč and D. Cincic, *Crystengcomm*, 2016, **18**, 7425-7429.
36. G. R. Desiraju, *Angew. Chem. Int. Ed.*, 2007, **46**, 8342-8356.
37. S. R. Vippagunta, H. G. Brittain and D. J. Grant, *Adv Drug Deliv Rev*, 2001, **48**, 3-26.
38. S. Byrn, R. Pfeiffer, M. Ganey, C. Hoiberg and G. Poochikian, *Pharm. Res.*, 1995, **12**, 945-954.

39. O. Almarsson and M. J. Zaworotko, *Chem. Commun.*, 2004, **0**, 1889-1896.
40. C. B. Aakeroy and D. J. Salmon, *CrystEngComm*, 2005, **7**, 439-448.
41. G. R. Desiraju, *CrystEngComm*, 2003, **5**, 466.
42. J. D. Dunitz, *CrystEngComm*, 2003, **5**, 506-506.
43. D. Braga, F. Grepioni, L. Maini, S. Prospero, R. Gobetto and M. R. Chierotti, *Chem. Commun.*, 2010, **46**, 7715-7717.
44. D. Braga, F. Grepioni and O. Shemchuk, *CrystEngComm*, 2018, **20**, 2212-2220.
45. D. Braga, F. Grepioni, G. I. Lampronti, L. Maini and A. Turrina, *Cryst. Growth Des.*, 2011, **11**, 5621-5627.
46. A. I. Kitaigorodskii, *Molecular crystals and molecules*, Academic Press, New York, 1973.
47. M. Paul, S. Chakraborty and G. R. Desiraju, *J. Am. Chem. Soc.*, 2018, **140**, 2309-2315.
48. A. J. Cruz-Cabeza, M. Lestari and M. Lusi, *Cryst. Growth Des.*, 2017, **18**, 855-863.
49. M. Lusi, *Cryst. Growth Des.*, 2018, **18**, 3704-3712.
50. N. Schultheiss and A. Newman, *Cryst. Growth Des.*, 2009, **9**, 2950-2967.
51. A. J. Cruz-Cabeza and J. Bernstein, *Chem. Rev.*, 2014, **114**, 2170-2191.
52. P. H. Karpinski, *Chem. Eng. Technol.*, 2006, **29**, 233-237.
53. W. D. Motherwell, H. L. Ammon, J. D. Dunitz, A. Dzyabchenko, P. Erk, A. Gavezzotti, D. W. Hofmann, F. J. Leusen, J. P. Lommerse, W. T. Mooij, S. L. Price, H. Scheraga, B. Schweizer, M. U. Schmidt, B. P. van Eijck, P. Verwer and D. E. Williams, *Acta Crystallogr. B*, 2002, **58**, 647-661.
54. W. Jones, W. D. S. Motherwell and A. V. Trask, *MRS Bull.*, 2011, **31**, 875-879.
55. D. K. Bucar, R. W. Lancaster and J. Bernstein, *Angew. Chem. Int. Ed. Engl.*, 2015, **54**, 6972-6993.
56. R. J. Davey, S. L. Schroeder and J. H. ter Horst, *Angew. Chem. Int. Ed.*, 2013, **52**, 2166-2179.
57. J. Bernstein, *Polymorphism in molecular crystals*, Oxford University Press, 2002.
58. R. Hilfiker, *Polymorphism: in the pharmaceutical industry*, John Wiley & Sons, 2006.
59. A. S. Raw, M. S. Furness, D. S. Gill, R. C. Adams, F. O. Holcombe, Jr. and L. X. Yu, *Adv Drug Deliv Rev*, 2004, **56**, 397-414.
60. G. R. Desiraju, *Cryst. Growth Des.*, 2008, **8**, 3-5.
61. D. Braga, F. Grepioni and L. Maini, *Chem. Commun.*, 2010, **46**, 6232-6242.
62. R. Purohit and P. Venugopalan, *Resonance*, 2009, **14**, 882-893.
63. J. Bernstein, *Cryst. Growth Des.*, 2011, **11**, 632-650.
64. D. S. Travis, J. K. Bowmaker and J. D. Mollon, *Vision Res.*, 1988, **28**, 481-490.
65. A. V. Yadav, A. S. Shete, A. P. Dabke, P. V. Kulkarni and S. S. Sakhare, *Indian J. Pharm. Sci.*, 2009, **71**, 359-370.
66. O. M. M. Santos, M. E. D. Reis, J. T. Jacon, M. E. d. S. Lino, J. S. Simões and A. C. Doriguetto, *Brazilian Journal of Pharmaceutical Sciences*, 2014, **50**, 1-24.
67. S. A. Danner, A. Carr, J. M. Leonard, L. M. Lehman, F. Gudiol, J. Gonzales, A. Raventos, R. Rubio, E. Bouza, V. Pintado, A. G. Aguado, J. Garcia de Lomas, R. Delgado, J. C. C. Borleffs, A. Hsu, J. M. Valdes, C. A. B. Boucher and D. A. Cooper, *New Engl. J. Med.*, 1995, **333**, 1528-1534.
68. S. R. Chemburkar, J. Bauer, K. Deming, H. Spiwek, K. Patel, J. Morris, R. Henry, S. Spanton, W. Dziki, W. Porter, J. Quick, P. Bauer, J. Donaubaue, B. A. Narayanan, M. Soldani, D. Riley and K. McFarland, *Organic Process Research & Development*, 2000, **4**, 413-417.
69. A. Y. Lee, D. Erdemir and A. S. Myerson, *Annu Rev Chem Biomol Eng*, 2011, **2**, 259-280.
70. J. Aaltonen, M. Alleso, S. Mirza, V. Koradia, K. C. Gordon and J. Rantanen, *Eur. J. Pharm. Biopharm.*, 2009, **71**, 23-37.
71. N. K. Duggirala, M. L. Perry, Ö. Almarsson and M. J. Zaworotko, *Chem. Commun.*, 2016, **52**, 640-655.
72. S. Golob, M. Perry, M. Lusi, M. R. Chierotti, I. Grabnar, L. Lassiani, D. Voinovich and M. J. Zaworotko, *J. Pharm. Sci.*, 2016, **105**, 3626-3633.
73. D.-K. Bučar, S. Filip, M. Arhangelskis, G. O. Lloyd and W. Jones, *CrystEngComm*, 2013, **15**, 6289-6291.
74. H. Oertling, *CrystEngComm*, 2016, **18**, 1676-1692.
75. S. M. Berge, L. D. Bighley and D. C. Monkhouse, *J. Pharm. Sci.*, 1977, **66**, 1-19.

76. N. K. Duggirala, M. L. Perry, O. Almarsson and M. J. Zaworotko, *Chem. Commun.*, 2016, **52**, 640-655.
77. P. H. Stahl and C. G. Wermuth, *Chem. Int*, 2002, **24**, 21.
78. N. J. Babu and A. Nangia, *Cryst. Growth Des.*, 2011, **11**, 2662-2679.
79. S. L. Childs, G. P. Stahly and A. Park, *Mol. Pharm.*, 2007, **4**, 323-338.
80. S. Aitipamula, R. Banerjee, A. K. Bansal, K. Biradha, M. L. Cheney, A. R. Choudhury, G. R. Desiraju, A. G. Dikundwar, R. Dubey, N. Duggirala, P. P. Ghogale, S. Ghosh, P. K. Goswami, N. R. Goud, R. R. K. R. Jetti, P. Karpinski, P. Kaushik, D. Kumar, V. Kumar, B. Moulton, A. Mukherjee, G. Mukherjee, A. S. Myerson, V. Puri, A. Ramanan, T. Rajamannar, C. M. Reddy, N. Rodriguez-Hornedo, R. D. Rogers, T. N. G. Row, P. Sanphui, N. Shan, G. Shete, A. Singh, C. C. Sun, J. A. Swift, R. Thaimattam, T. S. Thakur, R. Kumar Thaper, S. P. Thomas, S. Tothadi, V. R. Vangala, N. Variankaval, P. Vishweshwar, D. R. Weyna and M. J. Zaworotko, *Cryst. Growth Des.*, 2012, **12**, 2147-2152.
81. P. Vishweshwar, J. A. McMahon, J. A. Bis and M. J. Zaworotko, *J. Pharm. Sci.*, 2006, **95**, 499-516.
82. N. Shan and M. J. Zaworotko, *Drug Discov. Today*, 2008, **13**, 440-446.
83. D. Braga, L. Maini, G. de Sanctis, K. Rubini, F. Grepioni, M. R. Chierotti and R. Gobetto, *Chem. Eur. J.*, 2003, **9**, 5538-5548.
84. C. B. Aakeroy, M. E. Fasulo and J. Desper, *Mol. Pharm.*, 2007, **4**, 317-322.
85. B. Sarma, N. K. Nath, B. R. Bhogala and A. Nangia, *Cryst. Growth Des.*, 2009, **9**, 1546-1557.
86. O. Shemchuk, V. Andre, M. T. Duarte, P. Taddej, K. Rubini, D. Braga and F. Grepioni, *Cryst. Growth Des.*, 2017, **17**, 3379-3386.
87. O. Shemchuk, D. Braga and F. Grepioni, *Chem. Commun.*, 2016, **52**, 11815-11818.
88. S. Chakraborty, S. Joseph and G. R. Desiraju, *Angew. Chem. Int. Ed. Engl.*, 2018, **57**, 9279-9283.
89. A. K. S. Romasanta, D. Braga, M. T. Duarte and F. Grepioni, *CrystEngComm*, 2017, **19**, 653-660.
90. D. Braga, F. Grepioni, L. Maini, M. Polito, K. Rubini, M. R. Chierotti and R. Gobetto, *Chem. Eur. J.*, 2009, **15**, 1508-1515.
91. M. Lusi, I. J. Vitorica-Yrezabal and M. J. Zaworotko, *Cryst. Growth Des.*, 2015, **15**, 4098-4103.
92. E. Schur, E. Nauha, M. Lusi and J. Bernstein, *Chem. Eur. J.*, 2015, **21**, 1735-1742.
93. K. Suresh, M. K. C. Mannava and A. Nangia, *Chem. Commun.*, 2016, **52**, 4223-4226.

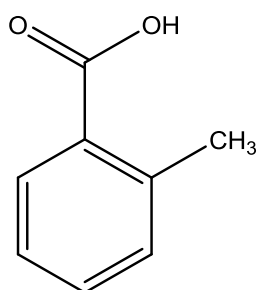
2. CHAPTER II - MOLECULAR SOLID SOLUTIONS

2.1. Overview

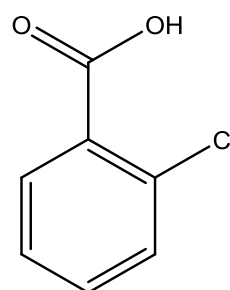
The investigation of multicomponent crystalline solids is a well-studied aspect of modern crystal engineering.¹⁻⁵ Solid solutions or organic alloys are nonstoichiometric multicomponent crystals in which two or more molecules are mutually miscible (at least in a certain composition range) in a solid. They are typically characterized by a structural disorder enabling the variation of the stoichiometric ratio of their components *in continuum*.⁴ These multicomponent solids are considered a useful tool for modifying physicochemical properties.^{3, 6, 7} Though solid solution often exhibit properties which are between those of the pure components, in some cases the formation of a solid solution may result into appearance of some new unexpected properties.^{4, 8}

To date, the solid solutions formation is still quite unpredictable. Typically, the solid solutions of organic molecules are formed by molecules similar in size. Concepts of isomorphicity and isostructurality are considered to be a prerequisite to identify potential solid solutions.

The investigation of solid solutions of organic molecules in our research group started with the preparation of disordered co-crystals between *o*-toluic acid and *o*-chlorobenzoic acid⁹ (fig. 2.1-1).



***o*-methylbenzoic acid**



***o*-chlorobenzoic acid**

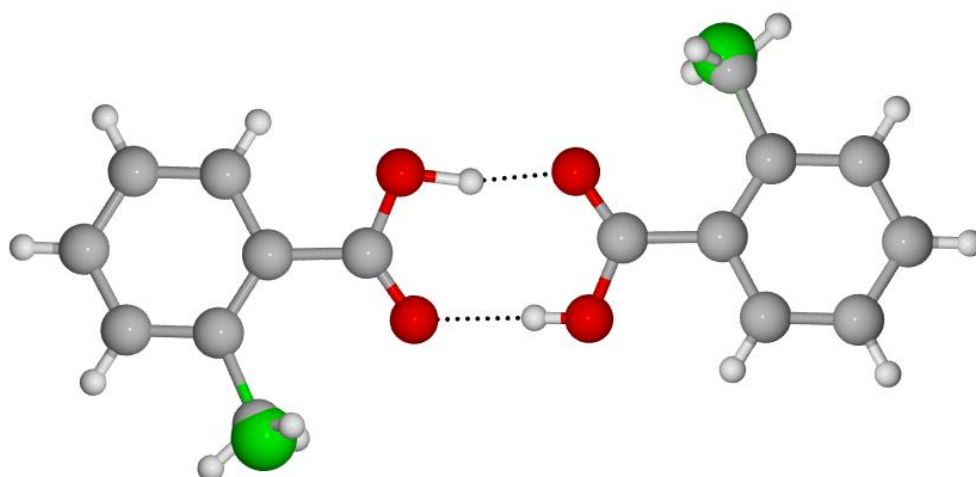


Figure 2.2.1-1 *o*-methylbenzoic and *o*-chlorobenzoic acids (top) and the disordered co-crystal formed by their interaction - TOJFUU⁹ (bottom)

Methyl and chloro- groups have similar shape and size with van der Waals volumes of ca. 19 \AA^3 and 21 \AA^3 correspondingly¹⁰. The obtained co-crystal is composed of quasi-isostructural molecules differing by a chlorine group replacing a methyl group or vice versa and it is characterized by the chloro-methyl exchange. A similar approach appeared to be useful also for *p*-methyl and *p*-chlorobenzyl alcohols (*p*-MeBA and *p*-ClBA correspondingly) (fig.2.1-2)¹¹. The quasi-isostructurality of the investigated molecules led to the formation of multicomponent solids isomorphous with one of the reagents - with the crystals of *p*-ClBA. Later on, this study has been extended with the bromine analogue(*p*-BrBA)¹²: the formation of binary and ternary solid solutions and the influence of composition variation on the melting point of the obtained multicomponent crystal form were described in details.

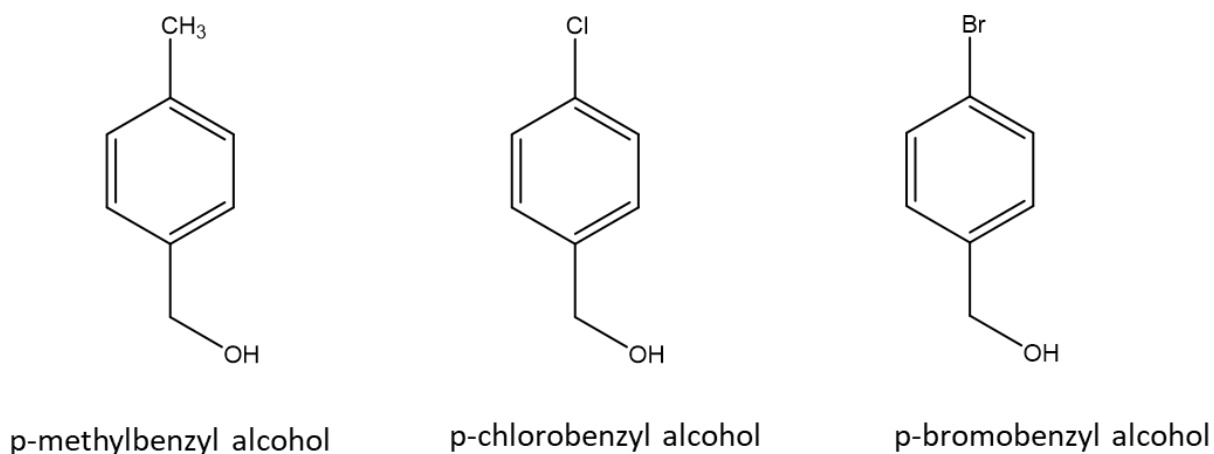


Figure 2.2.1-2 Compounds used for the preparation of binary and ternary solid solutions.

The following step in the investigation of the possibility to obtain solid solutions was to try and mix barbituric with thiobarbituric and cyanuric with trithiocyanuric acids (fig. 2.1-3). The idea was to use the relative similarity of carbonyl and thiocarbonyl groups to check whether they would be capable of forming solid solutions.

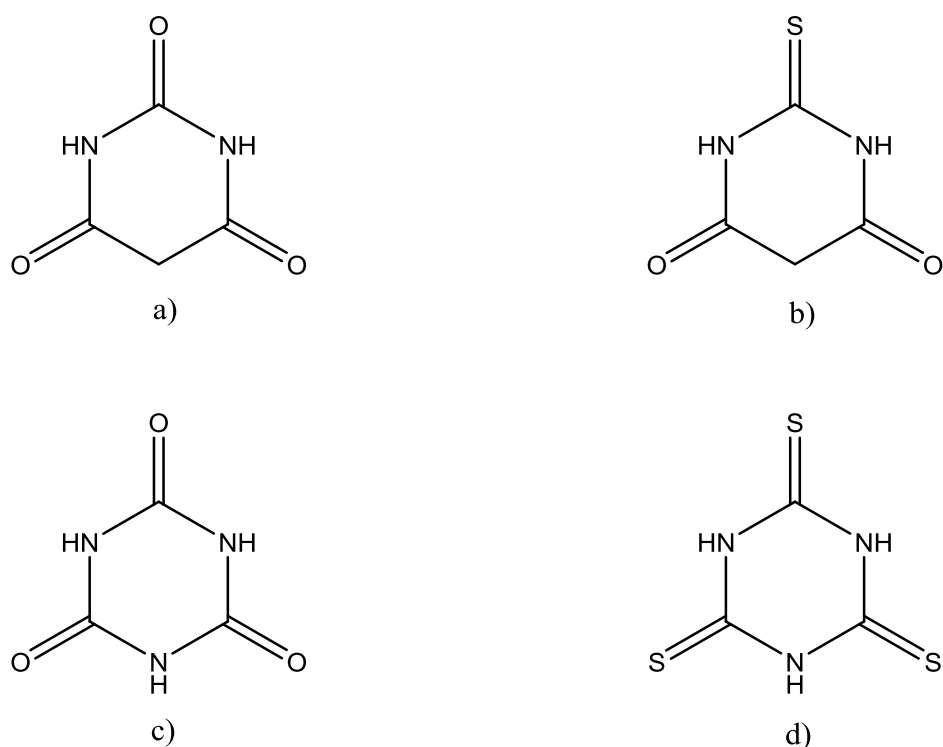


Figure 2.2.1-3 a) Barbituric acid (BA); b) Thiobarbituric acid (TBA); c) Cyanuric acid (CA); d) Trithiocyanuric acid (TCA).

The choice of the molecules was not random since both barbituric and thiobarbituric acids were widely investigated by our research group: the search for new polymorphic forms,¹³⁻¹⁵ molecular¹⁶ and ionic¹⁷⁻¹⁹ co-crystals.

The obtained results showed that it was possible to form solid solutions only with the first pair of the investigated acids – BA and TBA, whereas the mixing of CA with TCA regardless of the stoichiometry implied always led to the physical mixture of the starting materials. Actually, the obtained results lie within the concepts suggested by a latter study provided by Bucar et al.²⁰: isostructural crystals could be obtained via interchanging carbonyl with thiocarbonyl groups only if the exchanged atoms were not involved in hydrogen bonding.

2.2. Alloying barbituric and thiobarbituric acids: from solid solutions to a highly stable keto co-crystal form

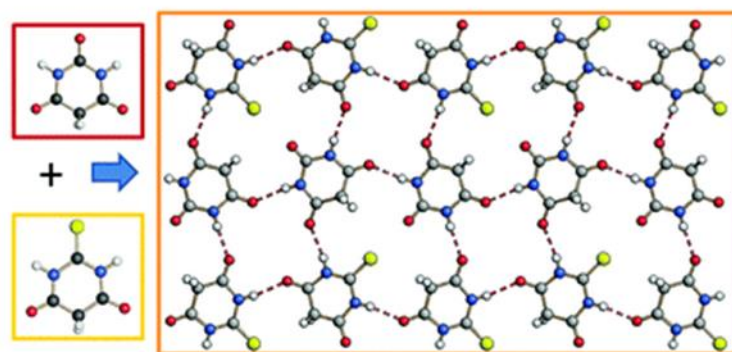
Alloying barbituric and thiobarbituric acids: from solid solutions to a highly stable keto co-crystal form

[O. Shemchuk](#)^a, [D. Braga](#)^a and [F. Grepioni](#)^{*a}

⊕ Author affiliations

Abstract

Alloying isomorphous crystals of barbituric acid (BA) and thiobarbituric acid (TBA) yields solid solutions of general formula BA_xTBA_{1-x} ($x < 0.8$); for $x = 0.5$ the stable co-crystal $BA_{0.5}TBA_{0.5}$, isomorphous with the parent keto forms, is observed, which melts at 265 °C, *i.e.* ca. 10 and 20 °C higher than the melting points of BA and TBA, respectively. While the BA_xTBA_{1-x} solid solutions with $x > 0.5$ are stable, those with $x < 0.5$ convert, with time or temperature, to the $BA_{0.5}TBA_{0.5}$ co-crystal.



For copyright reasons only the link to the original article is reported here:

<http://pubs.rsc.org/en/content/articlelanding/2016/cc/c6cc06615a#!divAbstract>

2.2.1. Supporting Information

The link to the supporting information is reported here:

<http://www.rsc.org/suppdata/c6/cc/c6cc06615a/c6cc06615a1.pdf>

EXPERIMENTAL PART

Solution Synthesis. All reactants and reagents were purchased from Sigma-Aldrich and used without further purification. Reagent grade solvents and bi-distilled water were used.

All the solid solutions of BA and TBA acids with general formula BA_xTBA_{1-x} were obtained by dissolution of the x and $1-x$ quantities of the starting materials (see SI-Table 1) in 20 mL of boiling EtOH; the solution was left to evaporate at room temperature.

SI-Table 1. Quantities of reagents employed in the crystallizations from solution.

BA:TBA ratio	BA, mg (mmol)	TBA, mg (mmol)
$BA_{0.2}TBA_{0.8}$	25.6 (0.2 mmol)	115.3 (0.8 mmol)
$BA_{0.3}TBA_{0.7}$	38.4 (0.3 mmol)	100.9 (0.7 mmol)
$BA_{0.4}TBA_{0.6}$	51.2 (0.4 mmol)	86.5 (0.6 mmol)
$BA_{0.5}TBA_{0.5}$	64.0 (0.5 mmol)	72.1 (0.5 mmol)
$BA_{0.6}TBA_{0.4}$	76.8 (0.6 mmol)	57.7 (0.4 mmol)
$BA_{0.7}TBA_{0.3}$	89.7 (0.7 mmol)	43.2 (0.3 mmol)
$BA_{0.8}TBA_{0.2}$	102.5 (0.8 mmol)	28.8 (0.2 mmol)

Solid State Synthesis. $BA_{0.5}TBA_{0.5}$ was also obtained by kneading either thiobarbituric acid form I (*keto*-form) with ethanol, or thiobarbituric acid form IV (*keto-enol* form) with acetonitrile. 1 mmol of BA and TBA were kneaded for 20 minutes in a Retsch MM200 ball miller, operated at a frequency of 20 Hz, in the presence of a few drops of the corresponding solvent.

Crystal structure determination. Single-crystal data for BA_xTBA_{1-x} ($x \geq 0.5$) was collected at RT on an Oxford X'Calibur S CCD diffractometer equipped with a graphite monochromator (Mo-K α radiation, $\lambda = 0.71073$ Å). Data collection and refinement details are listed in Table SI-S2. The program SHELX97²¹ was used for structure solution and refinement on F^2 . The program Platon²² was used to calculate intermolecular interactions. Schakal99²³ was used for molecular graphics. In BA_xTBA_{1-x} ($x \geq 0.5$) the S and O atoms (indicated by an arrow in Figure SI-1) of each

independent molecule were treated as disordered over two positions: the occupancy factor was first refined by keeping the isotropic thermal parameters fixed, then the occupancy factor was fixed and both oxygen and sulphur atoms were refined anisotropically. All non-hydrogen atoms were refined anisotropically. H_{CH} and H_{NH} atoms were added in calculated positions and refined riding on their respective carbon or nitrogen atoms.

Crystal data can be obtained free of charge *via* www.ccdc.cam.ac.uk/conts/retrieving.html (or from the Cambridge Crystallographic Data Centre, 12 Union Road, Cambridge CB21EZ, UK; fax: (+44)1223-336-033; or e-mail: deposit@ccdc.cam.ac.uk). CCDC numbers 1498572 (BA_{0.5}TBA_{0.5}), 149574 (BA_{0.6}TBA_{0.4}) and 149573 (BA_{0.7}TBA_{0.3}).

SI-Table 1. Single crystal data for the B_xTBA_{1-x} solid solutions with x ≥ 0.5, and comparison with data for BA form II at room temperature²⁴ and TBA form I [THBARB]²⁵ at room temperature.

	TBA form I (THBARB) ²⁵	BA _{0.5} TBA _{0.5}	BA _{0.6} TBA _{0.4}	BA _{0.7} TBA _{0.3}	BA _{0.8} TBA _{0.2} ^a	BA form II RT ²⁴
Formula	C ₄ H ₄ N ₂ O ₂ S	C ₄ H ₄ N ₂ O _{2.5} S _{0.5}	C ₄ H ₄ N ₂ O _{2.6} S _{0.4}	C ₄ H ₄ N ₂ O _{2.7} S _{0.3}	C ₄ H ₄ N ₂ O _{2.8} S _{0.2}	C ₄ H ₄ N ₂ O ₃
fw	144.15	136.12	134.52	132.91	131.31	128.09
Cryst. System	monoclinic	monoclinic	monoclinic	monoclinic	monoclinic	monoclinic
space group	P2 ₁ /c	P2 ₁ /c	P2 ₁ /c	P2 ₁ /c	P2 ₁ /c	P2 ₁ /c
Z, Z'	8, 2	8, 2	8, 2	8, 2	8, 2	8, 2
a (Å)	8.450(10)	8.533(1)	8.4662(13)	8.4569(9)	8.321(7)	8.199
b (Å)	13.140(20)	13.0141(10)	12.9681(12)	12.9400(10)	12.797(6)	12.613
c (Å)	10.420(10)	9.6918(12)	9.6819(11)	9.5593(9)	9.698(6)	9.823
α (deg)	90.00	90.0	90.0	90.0	90.0	90.00
β (deg)	92.70	92.131	92.490(14)	92.626(10)	93.70(6)	95.7
γ (deg)	90.00	90.0	90.0	90.0	90.0	90.00
V (Å³)	1155.679	1075.5(2)	1062.0(2)	1045.00(17)	1030.5(12)	1010.8
D_{calc} (g/cm³)	-	1.681	1.683	1.690	-	-
μ (mm⁻¹)	-	0.324	0.294	0.256	-	-
Measd reflns	-	4693	4603	4818	-	-
Indep reflns	-	2458	2431	2417	-	-
R1[on F_o², I > 2σ(I)]	-	0.0856	0.1059	0.0743	-	-
wR2 (all data)	-	0.1552	0.2839	0.1604	-	-

^a Unfortunately, despite many attempts at growing good quality single crystals of BA_{0.8}TBA_{0.2}, the quality of the best data set collected still does not reach the standard required for data deposition; however, the space group was ascertained with confidence, the sulphur contribution was evidenced and the cell volume was found to fit well within the trend from BA form II (room temperature data) to TBA form I (see below).

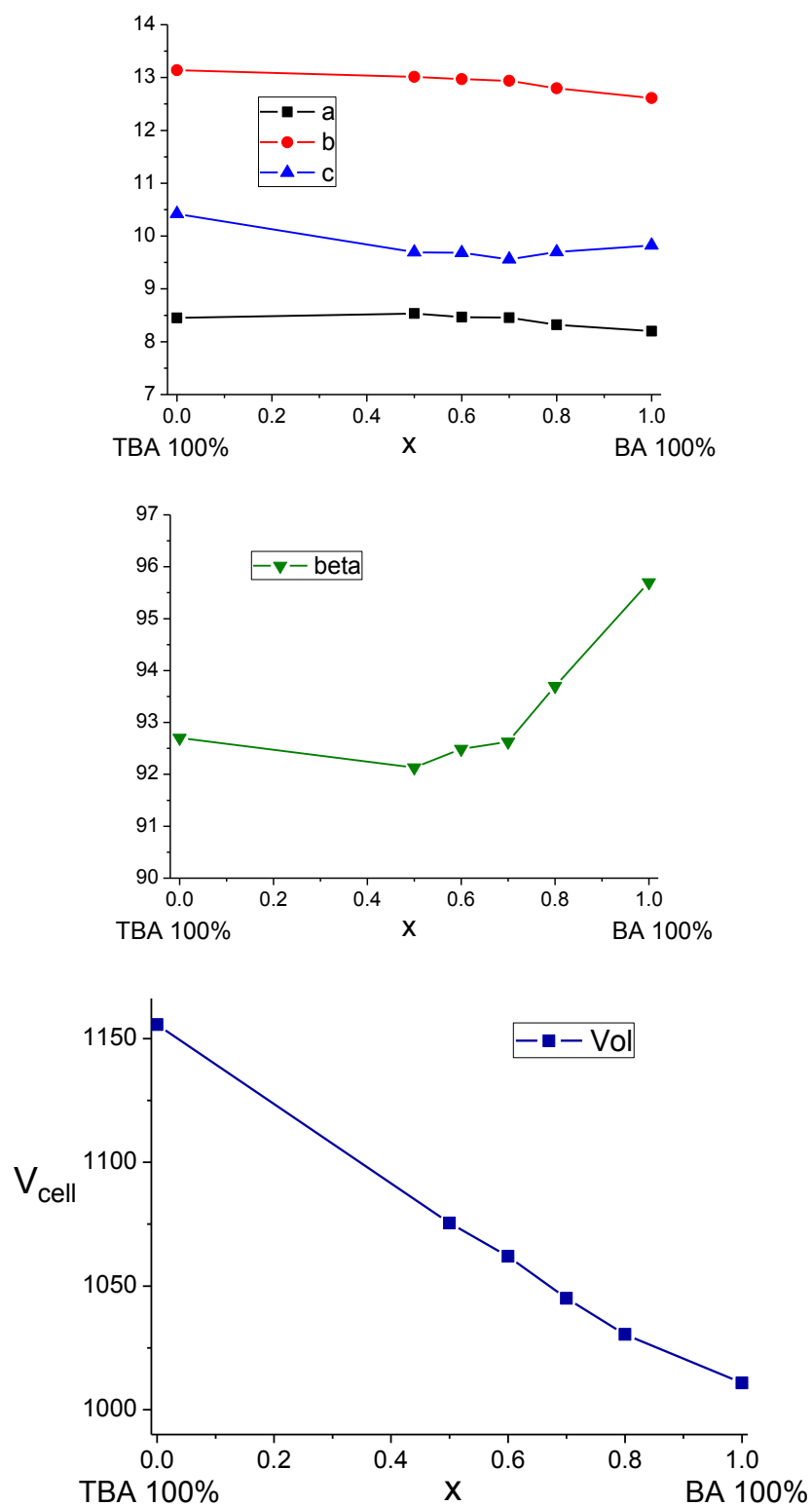


Figure SI-1. Cell parameters variation (single crystals, room temperature data) on passing from TBA form I to BA Form II: cell axes (top), monoclinic β angle (middle) and cell volume (bottom).

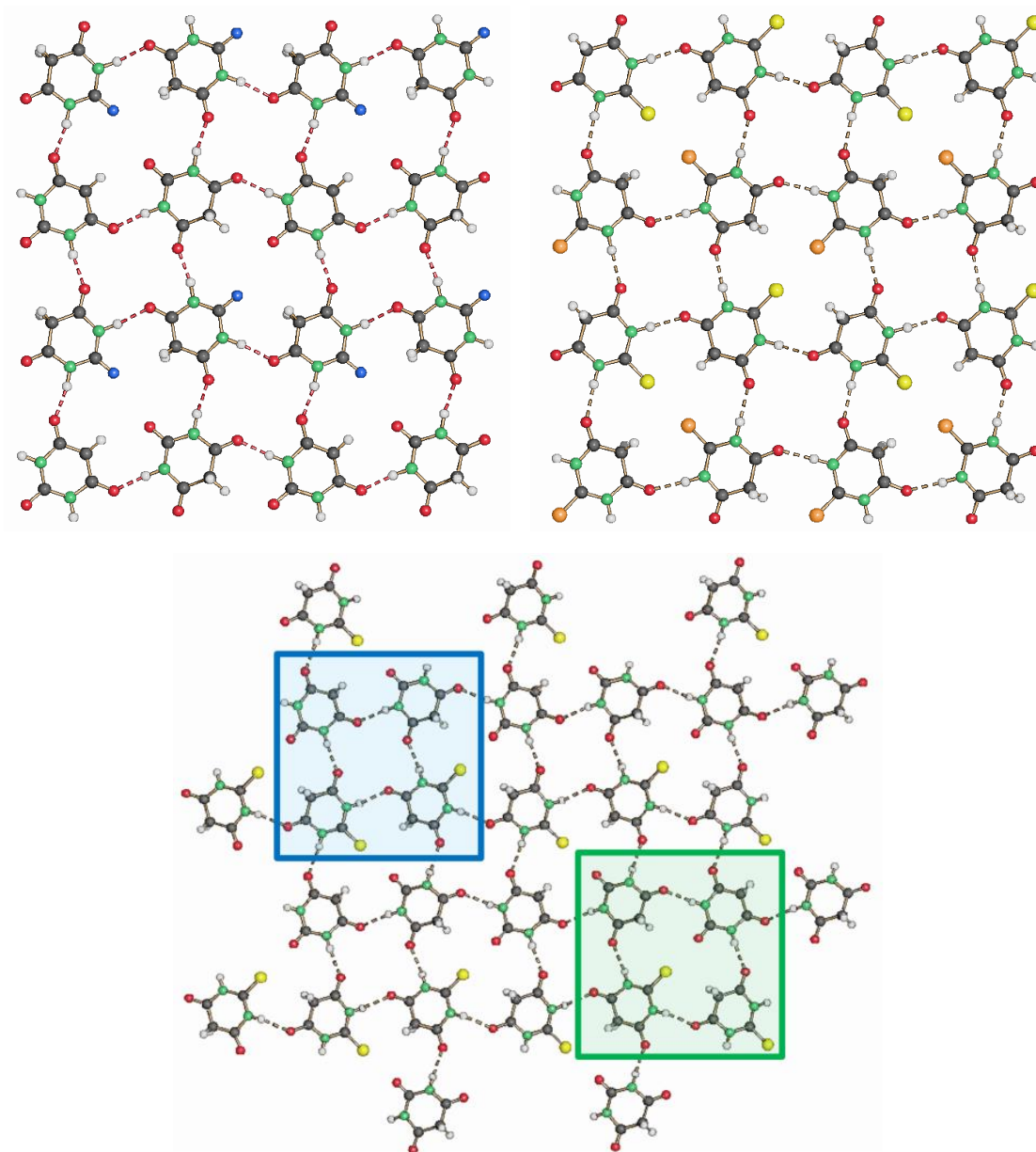


Figure SI-2. The hydrogen bonding pattern observed in BA form II (top left, BARBAC02, O atoms of independent molecules shown in red and blue) and in TBA form I (top right, THBARB, S atoms of independent molecules shown in yellow and orange) is also maintained in the solid solutions; here the packing for the $BA_{0.5}TBA_{0.5}$ co-crystal is shown (bottom), with the two large hydrogen bonded rings forming 2D parallel planes perpendicular to the crystallographic *ac*-plane.

X-ray powder diffraction. Room temperature X-ray powder diffraction (XRPD) patterns were collected on a PANalytical X'Pert PRO automated diffractometer equipped with a X'celerator detector in the 2θ range $3\text{--}50^\circ$ (step size 0.0334 , time/step 30.480 s, VxA 40×40). Data analyses were carried out using the Panalytical X'pert Highscore Plus program. The identity between the bulk material obtained via olution and solid-state processes was verified by comparing calculated and observed powder diffraction patterns. The program Mercury²⁶ was used for simulation of X-ray powder patterns on the basis of single crystal data, while the program

PowderCell²⁷ was used to simulate a powder pattern on the basis of cell parameters – thus to identify the angular position of relevant peaks – for $\text{BA}_{0.8}\text{TBA}_{0.2}$ and for BA form II at room temperature, for which only single crystal cell parameters were available.

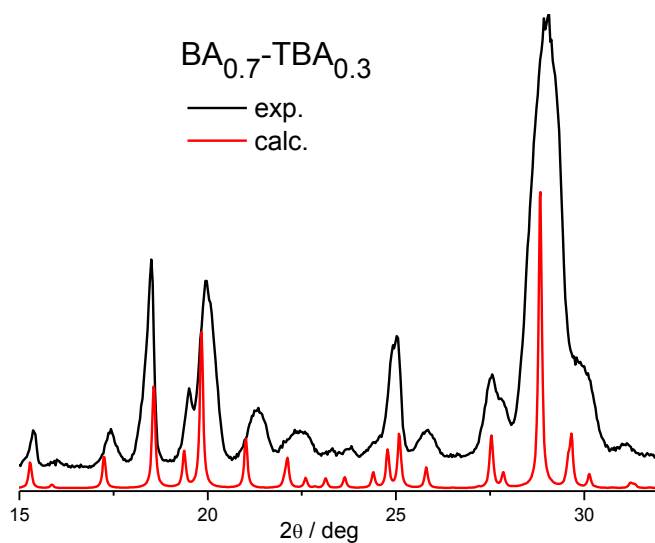
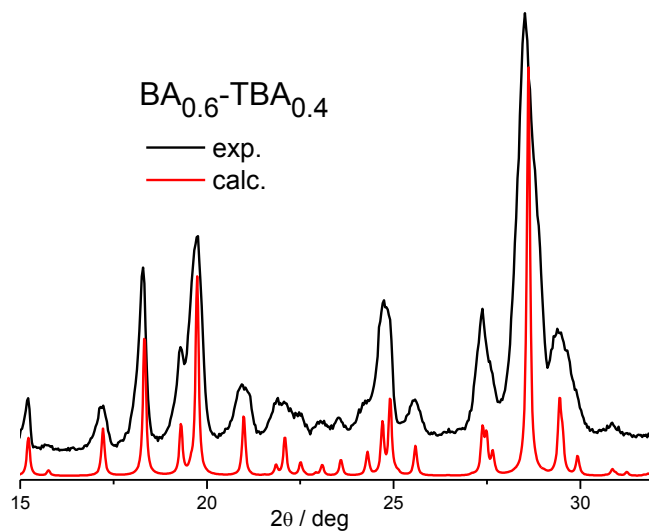
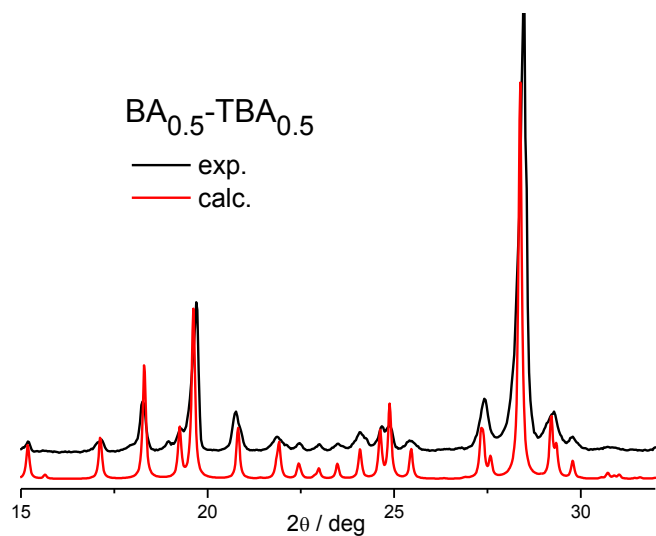


Figure SI-3. Comparison of experimental (crystallizations from solution) and simulated patterns (on the basis of single crystal data) for $BA_{0.5}TBA_{0.5}$, $BA_{0.6}TBA_{0.4}$ and $BA_{0.7}TBA_{0.3}$.

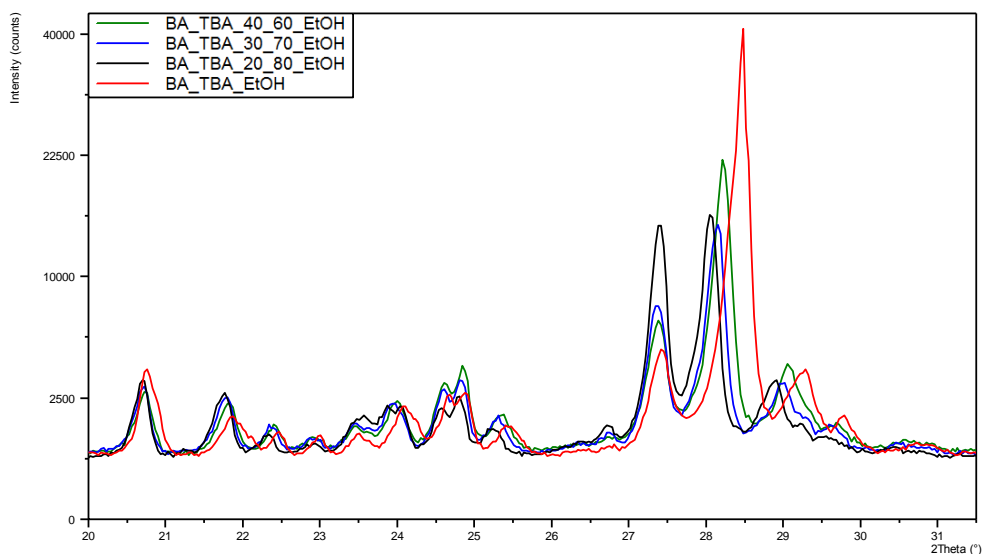


Fig. SI-4. Experimental XRPD patterns for BA_xTBA_{1-x} solid solutions with $x \leq 0.5$: expanded section showing a general shift (analogous to what observed for the solid solutions with $x > 0.5$) of the peaks towards *lower* angles, on increasing the percentage of TBA, with respect to the $BA_{0.5}TBA_{0.5}$ co-crystal (red line).

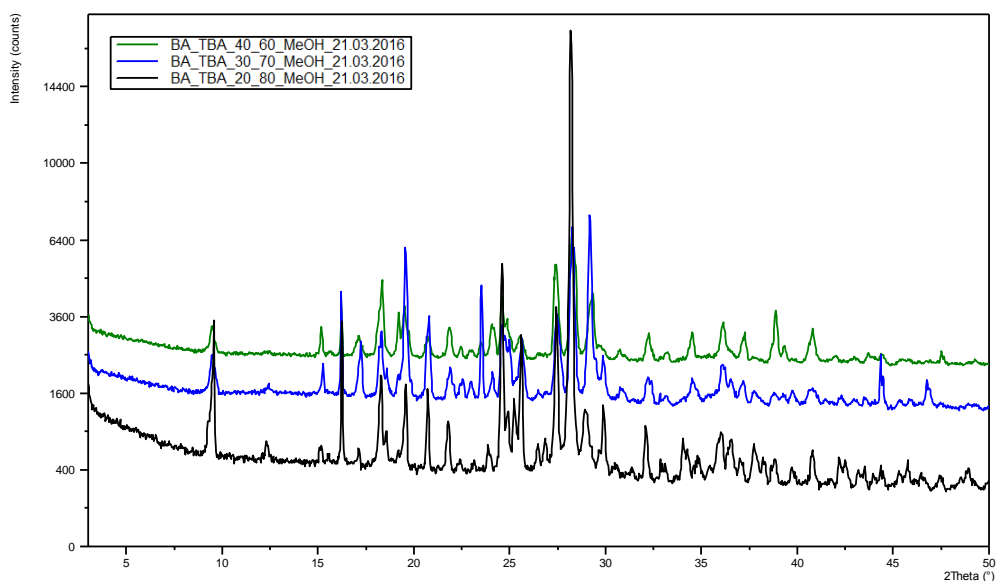


Figure SI-5. Comparison between the XRPD pattern measured on the products obtained by crystallizing from MeOH BA form II and THBARB form I in 40:60 (top, green line), 30:70 (middle, blue line) and 20:80 (bottom, black line) molar ratios: $BA_{0.5}TBA_{0.5}$ is formed in all cases, together with unreacted TBA.

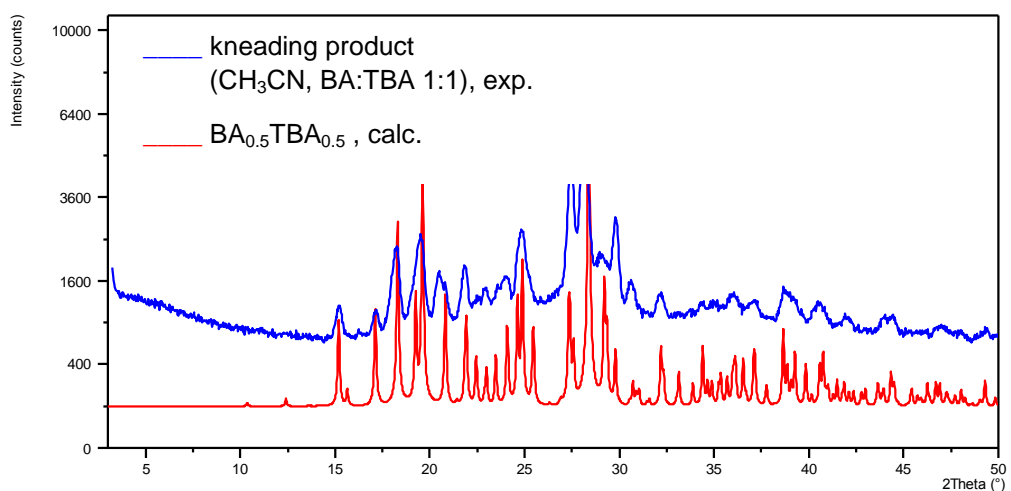


Figure SI-6 Comparison between the XRPD pattern measured on the product obtained by kneading BA form II and THBARB form I in 1:1 molar ratio in the presence of a few drops of CH₃CN and (top, blue line) and the simulated pattern pattern (on the basis of single crystal data) for BA_{0.5}TBA_{0.5}.

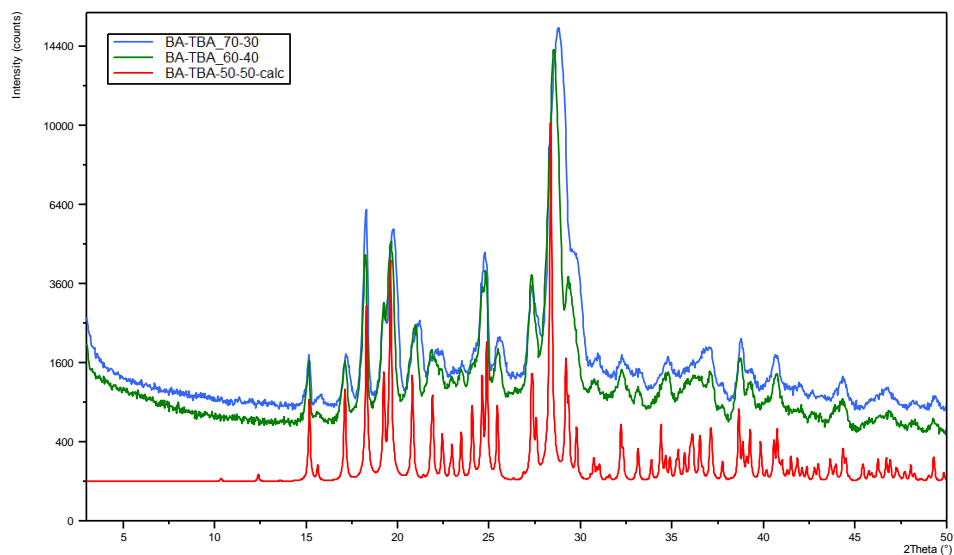


Figure SI-7. Comparison between the XRPD experimental patterns measured after 3 months of standing in open air at ambient conditions on BA_{0.7}TBA_{0.3} (blue line) and BA_{0.7}TBA_{0.3} (green line) and the calculated pattern for BA_{0.5}TBA_{0.5}; the solid solutions are still unchanged.

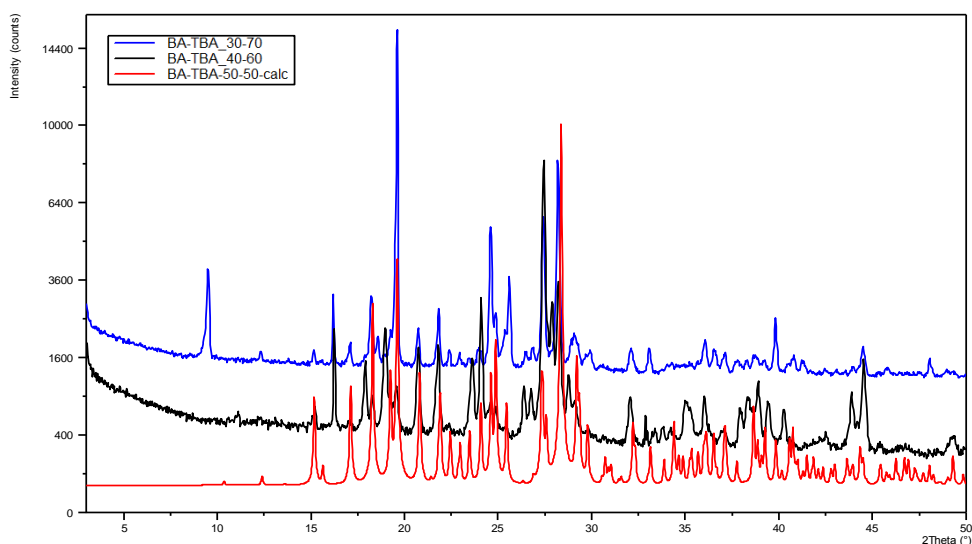


Figure SI-8. Comparison between the XRPD experimental patterns measured after 1 month of standing in open air at ambient conditions on $\text{BA}_{0.3}\text{TBA}_{0.7}$ (blue line) and $\text{BA}_{0.4}\text{TBA}_{0.6}$ (black line) and the calculated pattern for $\text{BA}_{0.5}\text{TBA}_{0.5}$; the solid solutions have converted into the co-crystal $\text{BA}_{0.5}\text{TBA}_{0.5}$ plus an excess of TBA form I.

Hot Stage Microscopy (HSM). HSM measurements were carried out using a Linkam TMS94 device connected to a Linkam LTS350 platinum plate. Images were collected with the imaging software Cell, from a Visicam 5.0 stereoscope. Images (100x) were taken with an Olympus optical microscope.

Differential Scanning Calorimetry (DSC)

DSC measurements were performed with a Perkin–Elmer Diamond. The samples (3-10 mg) were placed in open aluminum pans, and the heating was carried out at 10 °C min^{-1} in N_2 atmosphere.

Peak temperatures ($^{\circ}\text{C}$) are indicated in all DSC heating traces shown in the following.

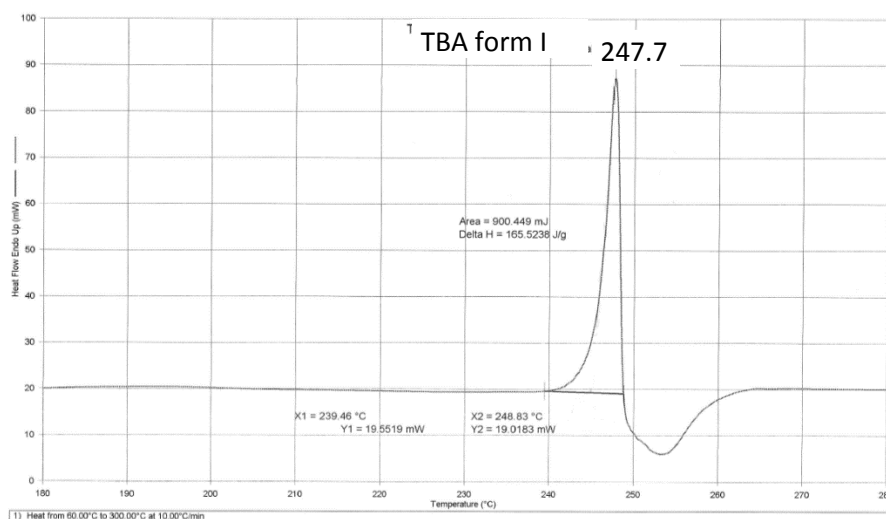


Figure SI-11. DSC trace of TBA form I

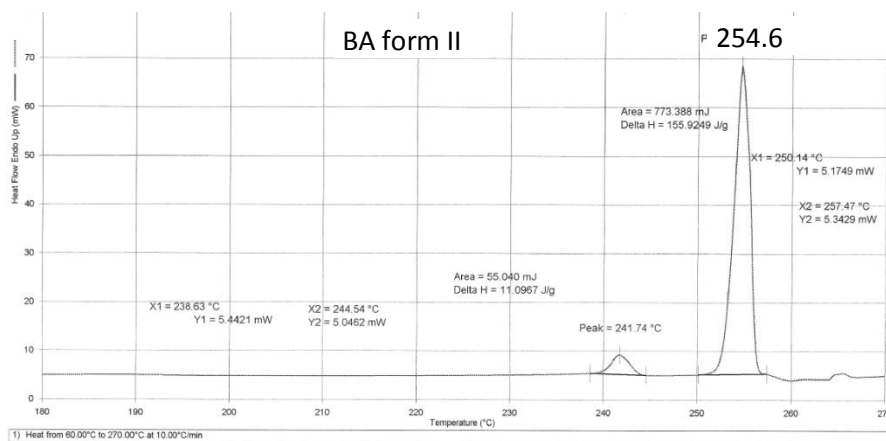


Figure SI-12. DSC trace of BA form II

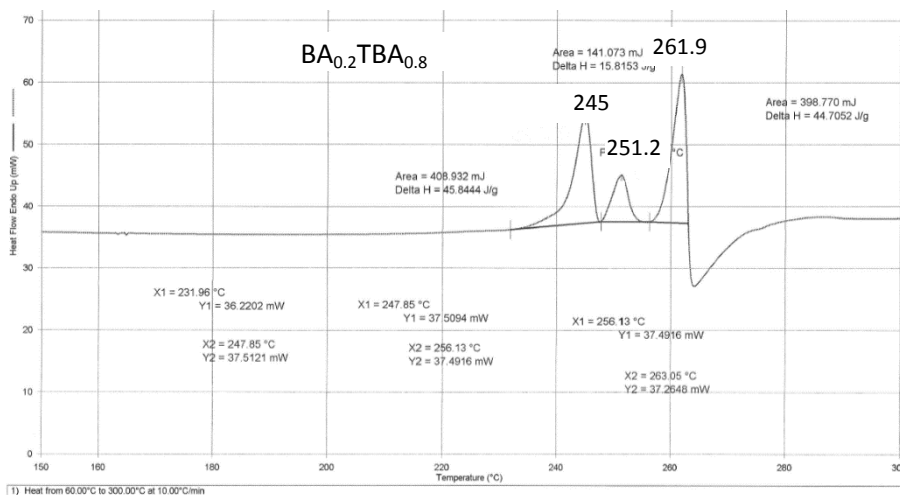


Figure SI-13. DSC trace of the product of crystallization of BA form II and TBA form I in 20:80 stoichiometric ratio.

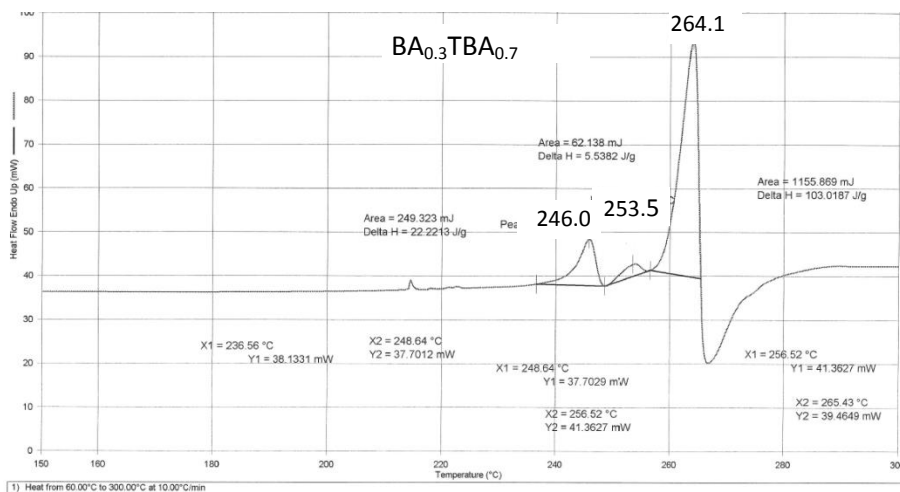


Figure SI-14. DSC trace of the product of crystallization of BA form II and TBA form I in 30:70 stoichiometric ratio.

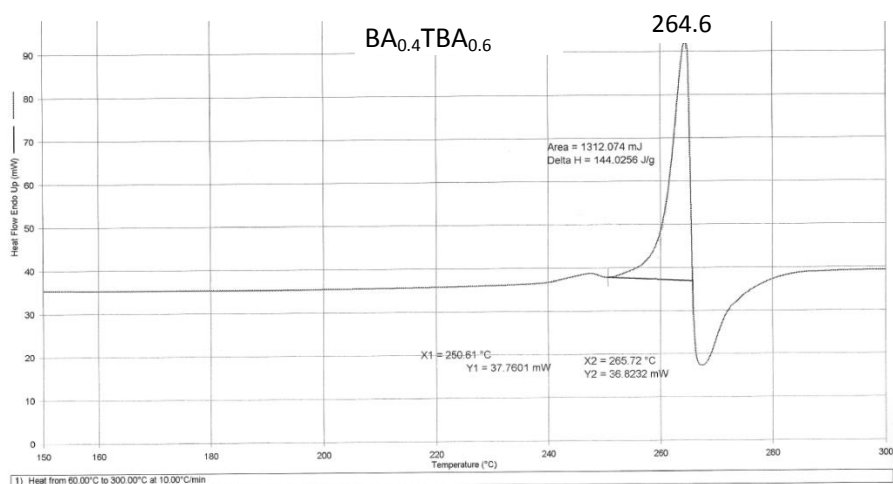


Figure SI-15. DSC trace of the product of crystallization of BA form II and TBA form I in 40:60 stoichiometric ratio.

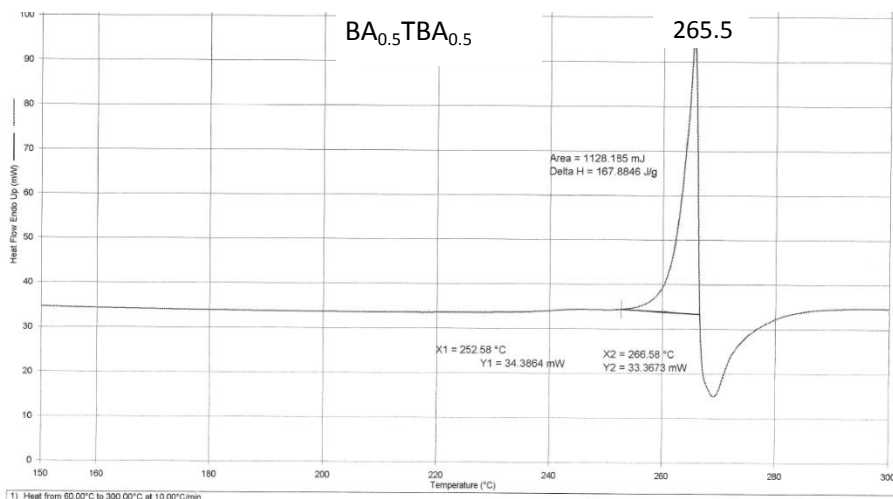


Figure SI-16. DSC trace of the product of crystallization of BA form II and TBA form I in 50:50 stoichiometric ratio.

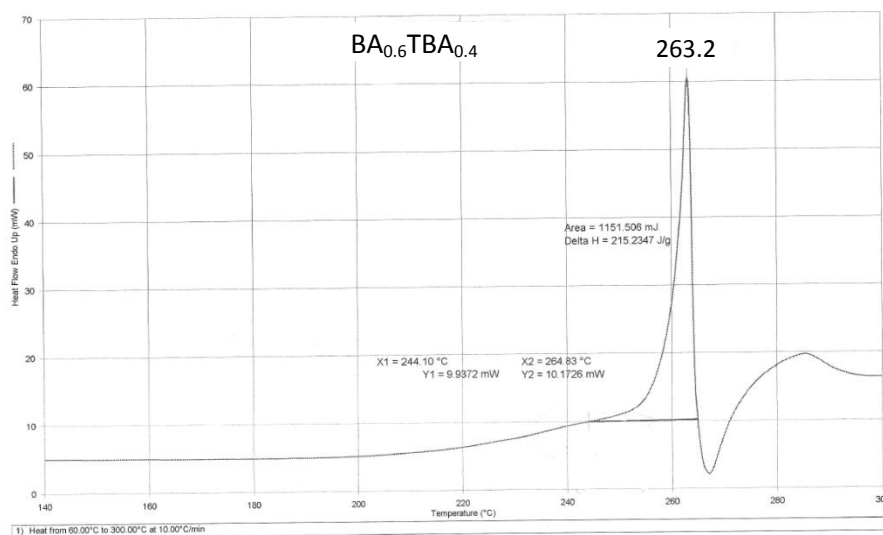


Figure SI-17. DSC trace of the product of crystallization of BA form II and TBA form I in 60:40 stoichiometric ratio.

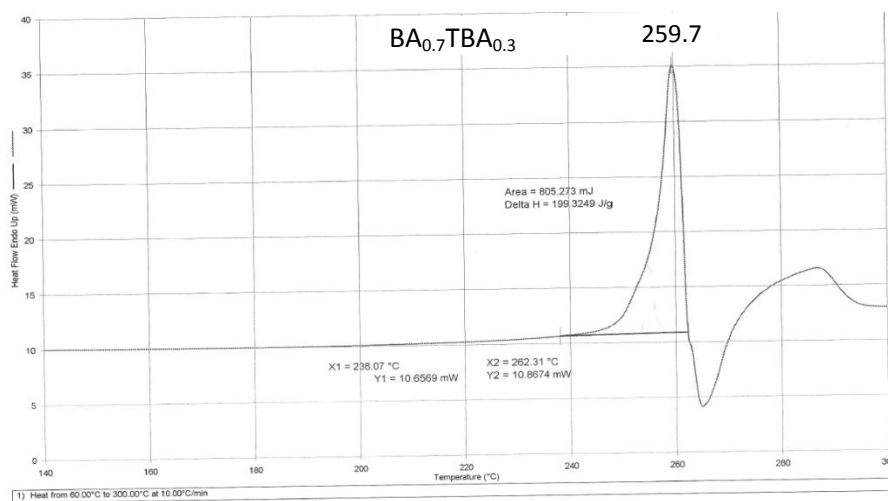


Figure SI-18. DSC trace of the product of crystallization of BA form II and TBA form I in 70:30 stoichiometric ratio.

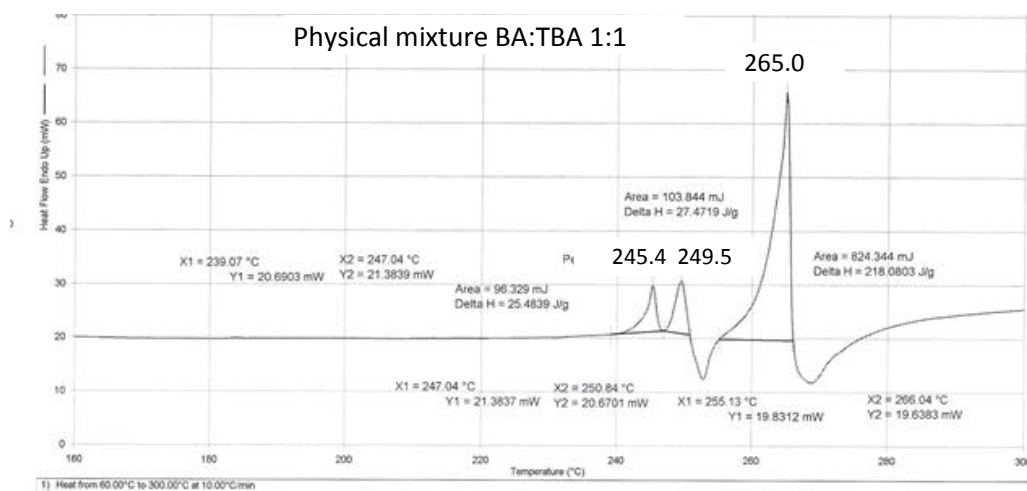


Figure SI-19. DSC of a 1:1 physical mixture of BA form II and TBA I, showing formation of the BA_{0.5}TBA_{0.5} co-crystal upon melting of the two components.

2.3. References

1. D. Braga, F. Grepioni, L. Maini and S. d'Agostino, *IUCrJ*, 2017, **4**, 369-379.
2. M. Paul, S. Chakraborty and G. R. Desiraju, *J. Am. Chem. Soc.*, 2018, **140**, 2309-2315.
3. M. Lusi, I. J. Vitorica-Yrezabal and M. J. Zaworotko, *Cryst. Growth Des.*, 2015, **15**, 4098-4103.
4. M. Lusi, *Cryst. Growth Des.*, 2018, **18**, 3704-3712.
5. A. J. Cruz-Cabeza, M. Lestari and M. Lusi, *Cryst. Growth Des.*, 2017, **18**, 855-863.
6. E. Schur, E. Nauha, M. Lusi and J. Bernstein, *Chem. Eur. J.*, 2015, **21**, 1735-1742.
7. K. Suresh, M. K. C. Mannava and A. Nangia, *Chem. Commun.*, 2016, **52**, 4223-4226.
8. O. Shemchuk, D. Braga and F. Grepioni, *Chem. Commun.*, 2016, **52**, 11815-11818.
9. M. Polito, E. D'Oria, L. Maini, P. G. Karamertzanis, F. Grepioni, D. Braga and S. L. Price, *CrystEngComm*, 2008, **10**, 1848.
10. A. I. Kitaigorodskii, *Molecular crystals and molecules*, Academic Press, New York, 1973.
11. D. Braga, F. Grepioni, L. Maini, M. Polito, K. Rubini, M. R. Chierotti and R. Gobetto, *Chem. Eur. J.*, 2009, **15**, 1508-1515.
12. A. K. S. Romasanta, D. Braga, M. T. Duarte and F. Grepioni, *CrystEngComm*, 2017, **19**, 653-660.
13. D. Braga, M. Cadoni, F. Grepioni, L. Maini and K. Rubini, *CrystEngComm*, 2006, **8**, 756-763.
14. M. R. Chierotti, L. Ferrero, N. Garino, R. Gobetto, L. Pellegrino, D. Braga, F. Grepioni and L. Maini, *Chem. Eur. J.*, 2010, **16**, 4347-4358.
15. M. U. Schmidt, J. Brüning, J. Glinnemann, M. W. Hützel, P. Mörschel, S. N. Ivashevskaya, J. van de Streek, D. Braga, L. Maini, M. R. Chierotti and R. Gobetto, *Angew. Chem. Int. Ed.*, 2011, **50**, 7924-7926.
16. M. R. Chierotti, K. Gaglioti, R. Gobetto, D. Braga, F. Grepioni and L. Maini, *CrystEngComm*, 2013, **15**, 7598.
17. D. Braga, F. Grepioni, L. Maini, S. Prospero, R. Gobetto and M. R. Chierotti, *Chem. Commun.*, 2010, **46**, 7715-7717.
18. D. Braga, F. Grepioni, G. I. Lampronti, L. Maini and A. Turrina, *Cryst. Growth Des.*, 2011, **11**, 5621-5627.
19. L. Maini, D. Braga, F. Grepioni, G. I. Lampronti, K. Gaglioti, R. Gobetto and M. R. Chierotti, *CrystEngComm*, 2016, **18**, 4651-4657.
20. M. K. Corpinot, R. Guo, D. A. Tocher, A. B. M. Buanz, S. Gaisford, S. L. Price and D.-K. Bučar, *Cryst. Growth Des.*, 2017, **17**, 827-833.
21. G. M. Sheldrick, *Acta Crystallographica Section C Structural Chemistry*, 2015, **71**, 3-8.
22. A. L. Spek, *Acta Crystallogr. Sect. D Biol. Crystallogr.*, 2009, **65**, 148-155.
23. E. Keller, *University of Freiburg, Germany*, 1999.
24. M. a. V. Roux, M. Temprado, R. Notario, C. n. Foces-Foces, V. N. Emel'yanenko and S. P. Verevkin, *J. Phys. Chem. A*, 2008, **112**, 7455-7465.
25. J. M. M.-R. Calas, *C.R.Acad.Sci., Ser. C (Chim)* 1967, **265**, 631.
26. C. F. Macrae, I. J. Bruno, J. A. Chisholm, P. R. Edgington, P. McCabe, E. Pidcock, L. Rodriguez-Monge, R. Taylor, J. van de Streek and P. A. Wood, *J. Appl. Crystallogr.*, 2008, **41**, 466-470.
27. W. Kraus and G. Nolze, *PowderCell 2.0*, (BAM Berlin) © subgroups derived by Ulrich Müller (Gh Kassel).

3. CHAPTER III - IONIC CO-CRYSTALS

3.1. Overview

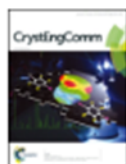
Crystalline solid materials formed by a neutral molecule and a salt have been known for long, however, only recently they have been defined as “ionic co-crystals” (ICCs). The term was coined by our research group.¹ Initially, the term was employed only for the co-crystals formed by a neutral organic molecule and an inorganic salt of an alkali or alkaline earth metals (mainly halides). Later on, this term has also been used for the co-crystals of neutral molecules with organic or organic-inorganic salts.²⁻⁴

This chapter is focused on the design, preparation and evaluation of co-crystals formed by organic molecules and inorganic salts –alkali and alkaline earth metal halides. The principal interactions in such systems are those established by metal cations with the organic groups – generally oxygen or nitrogen atoms capable of donating electrons. The anions (halides), in turn, form hydrogen bonds with the hydrogen donor groups on the organic moieties.² Solid materials formed by organic-inorganic systems are of interest for pharmaceutical, agrochemical, food and other industries since they could combine the physicochemical properties of the individual components.⁵⁻⁹ They have proved to be advantageous to obtain modified solid-state properties with respect to those of the separate components (improved thermal stability, different solubilities and intrinsic dissolution rates, reduced hygroscopicity, etc.).¹⁰⁻¹⁷ For these reasons ICCs are attracting the interest of researchers working in the field of co-crystals and utilizing the tools of crystal engineering to prepare multicomponent materials.

The investigation of ICCs formation performed during my PhD project can be subdivided into two general directions:

1. The formation of ICCs aimed at modification of the physicochemical properties of interest (mainly intrinsic dissolution rate and solubility).
2. The co-crystallization of inorganic salts with chiral compounds. The goal of this research was to investigate the possibility to apply co-crystallization as a tool to either separate a particular enantiomer from a racemic mixture or to prevent its possible transformation into a different form.

The detailed information on the ICCs formed by organic molecules and inorganic salts can be found in our recent highlight paper:²



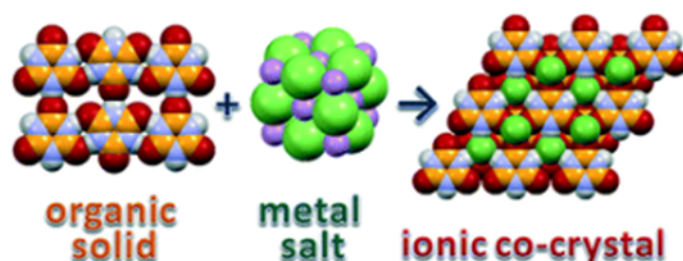
Organic–inorganic ionic co-crystals: a new class of multipurpose compounds

[Dario Braga](#),*^a [Fabrizia Grepioni](#)^a and [Oleksii Shemchuk](#)^a

⊕ Author affiliations

Abstract

In this highlight, the reasons for the widespread interest generated by ionic co-crystals, namely those formed by a neutral molecule and a salt, are addressed. In particular, the class of compounds obtained by co-crystallization of neutral organic molecules and inorganic salts (e.g. alkali and alkaline earth halides, sulfates, phosphates etc.) is discussed with the focus on their applications in diverse areas, such as pharmaceuticals, food and fertilizers, and also in chiral resolution. It is argued that, in terms of structure and intermolecular bonding features, these compounds do not differ from classical coordination compounds (complexes) and that their popularity arises from the effectiveness of the organic–inorganic assembly to enhance thermal stability, improve particle size and morphology and change significantly the solubility and dissolution rate with respect to those of the pure active ingredients.



For copyright reasons only the link to the original article is reported here:

<http://pubs.rsc.org/en/content/articlelanding/2018/ce/c8ce00304a#!divAbstract>

3.2. Ionic co-crystals of cyanuric acid with alkali halides

3.2.1. Introduction

The investigation of ICCs formation began with mechanochemical^{18, 19} co-crystallization of thiobarbituric, cyanuric and trithiocyanuric acids (fig. 3.2.1-1) with the alkali halides. As it was already mentioned in the second chapter, barbituric and thiobarbituric acids were extensively studied by our research group for the possibility of existence of new polymorphic forms,²⁰⁻²² molecular²³ and ionic^{1, 11, 24} co-crystals.

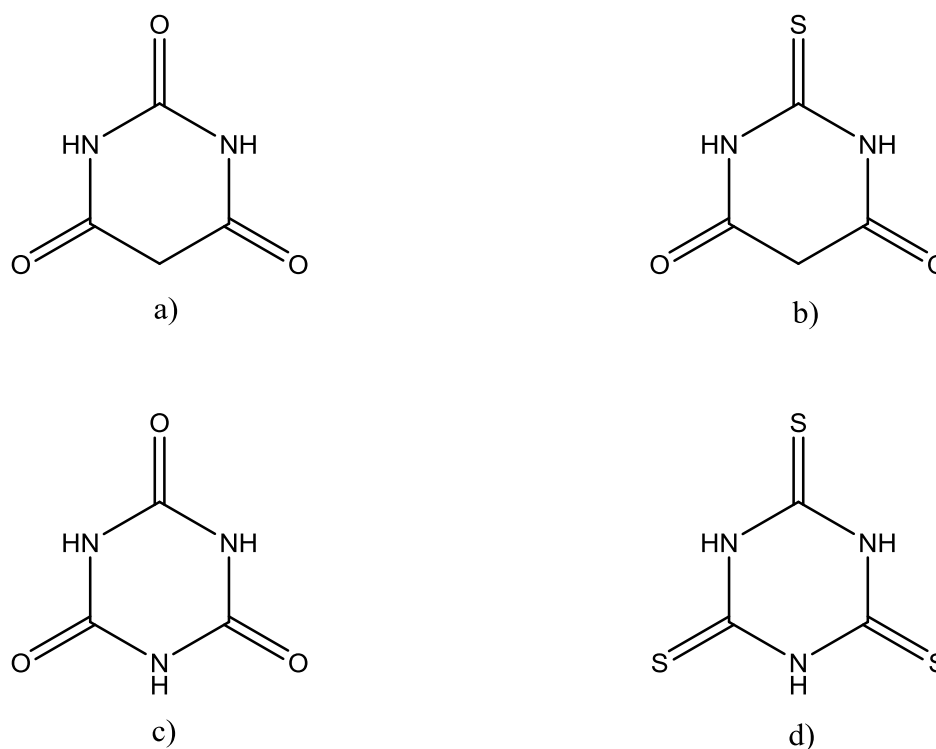


Figure 3.2.1-1 a) Barbituric acid (BA); b) Thiobarbituric acid (TBA); c) Cyanuric acid (CA); d) Trithiocyanuric acid (TCA).

In fact, the existence of the whole class of “ionic co-crystals” was accidentally discovered when pellets of barbituric acid (BA) with potassium bromide were prepared for IR spectroscopy.¹ Consequently, the crystal structures of the

whole family of ICCs of BA with alkali bromides as well as with caesium iodide were established. In the obtained ICCs all three carbonyl groups of barbituric acids are involved in coordination with metal cations (fig. 3.2.1-2, BA·KBr·2H₂O is given as an example). The bromides, in turn, form hydrogen bonds with NH-groups and water molecules.

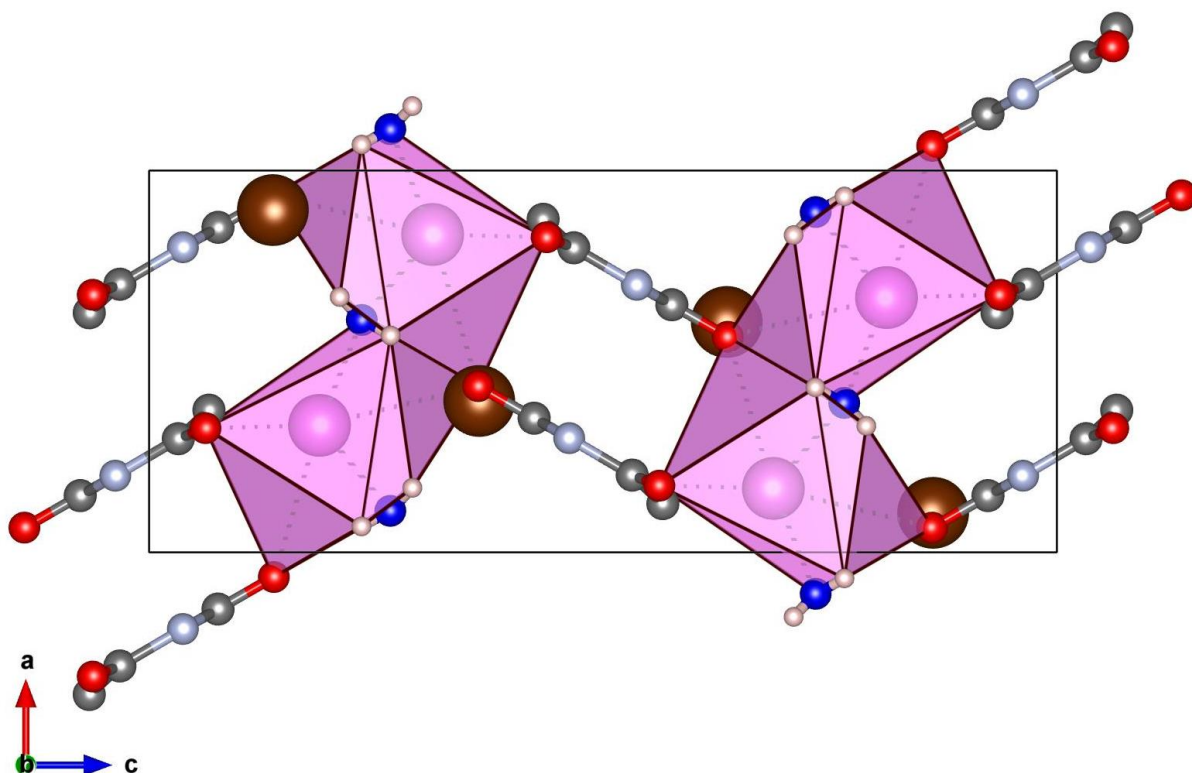


Figure 3.2.1-2 The ionic co-crystal formed by barbituric acid and KBr - BA·KBr·2H₂O (ref. code NAHQIY¹). Hydrogen atoms of cyanuric acid are omitted and water molecules are marked in blue for the sake of clarity.

The molecule of cyanuric acid (CA) could represent, in principle, an even more suitable target for ICCs formation compared to barbituric acid since it has three NH-groups which can form hydrogen bonds with halides. The obtained results (table 3.2.1-1) showed that our assumption was correct and CA formed ICCs with the absolute majority of the alkali halides.

Table 3.2.1-1 Mechanochemical preparation of ICCs of CA with alkali halides.

	Cl	Br	I
Li	CA·LiCl ¹²	New*	New*
Na	CA·NaCl ¹²	CA·NaBr CA·NaBr·2H ₂ O	New*
K	No ICC	CA·KBr	CA·KI·2H ₂ O Solved by SG
Rb	CA ₂ ·RbCl	CA·RbBr	CA·RbI
Cs	CA ₂ ·CsCl	CA·CsBr	No ICC

*New phase was detected using XRPD, but the structure was not solved.

Unfortunately, the co-crystallization of thiobarbituric and trithiocyanuric acids, in turn, was much less successful: only one ICC of TBA with caesium bromide was obtained and structurally characterized. The idea was to understand how the virtual substitution of one (TBA) and all three (TCA) carbonyl groups with thiocarbonyl could impact the co-crystallization propensity of the corresponding organic molecule. Especially, such comparison was considered valuable after the possibility of formation of solid solutions between BA and TBA was discovered.²⁵

The co-crystallization of cyanuric acid with the majority of alkali halides resulted into formation of ionic co-crystals (table 1). Quite surprisingly, the majority of the obtained ICCs appeared to be anhydrous. The anhydrous nature of ICCs with LiCl and NaCl is rather unusual. The majority of ICCs of alkali halides in the CSD²⁶ are hydrated, especially the ones formed by lithium or sodium cations - high to medium charge density alkali ions. Most likely, the formation of anhydrous ICCs can be explained by the peculiar structure of CA: it

is small, highly symmetrical and capable of both hydrogen bonding to the anions and cation complexation via O-atoms.

Cyanuric acid has a very low water solubility.¹² With the aim to increase its solubility NaCl·CA was chosen to perform the measurements of the intrinsic dissolution rate – the rate at which the compound is released from its crystal lattice into solution, and of the thermodynamic solubility.

3.2.2. Anhydrous ionic co-crystals of cyanuric acid with LiCl and NaCl

The results of the co-crystallization of CA with LiCl and NaCl and the impact of ICC formation on the solubility characteristics have been recently published:

Issue 10, 2017



From the journal:
CrystEngComm

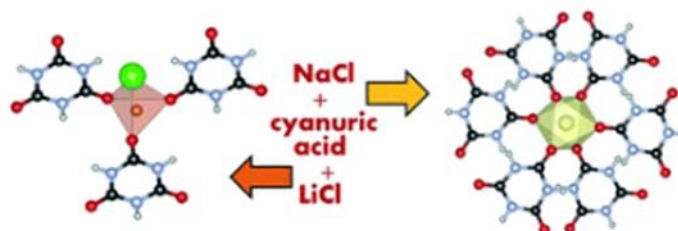
Anhydrous ionic co-crystals of cyanuric acid with LiCl and NaCl

Oleksii Shermchuk,^a Dario Braga,^a Lucia Maini^a and Fabrizia Grepioni^{*a}

⊕ Author affiliations

Abstract

Anhydrous ionic co-crystals (ICCs) of cyanuric acid (CA) with sodium and lithium chlorides have been prepared by solid state methods and structurally characterized from X-ray powder diffraction data (XRPD). Complete encapsulation of the Li^+Cl^- ion pair by the organic molecules is observed in CA-LiCl, while the solid-state solvation of piles of Na^+ cations in CA-NaCl results in the markedly increased dissolution rate (ca. 5 times) and solubility (ca. 20 times) in water with respect to pure CA.



For copyright reasons only the link to the original article is reported here:

<http://pubs.rsc.org/en/content/articlelanding/2017/ce/c7ce00037e#!divAbstract>

3.2.2.1. Supplementary Information

The link to the supporting information is reported here:

<http://www.rsc.org/suppdata/c7/ce/c7ce00037e/c7ce00037e1.pdf>

Experimental Part

Materials and instrumentation

All reagents and solvents used in this work were purchased from Sigma-Aldrich and used without further purification.

Solid State Synthesis

ICCs of cyanuric acid were obtained by kneading CA (1 mmol) and the corresponding co-former (1 mmol) for 30-60 minutes in a Retsch MM200 ball miller, operated at a frequency of 25 Hz, in the presence of a few drops of solvent (ethanol and water for CA·NaCl, methanol for CA·LiCl). CA·LiCl was also obtained by manual grinding, but its preparation of CA·LiCl was more difficult due to the high hygroscopicity of LiCl, and 4 to 5 cycles of grinding in a mortar (up to 5 minutes) followed by drying in the oven (15-20 minutes) were necessary to get a pure product.

X-ray powder diffraction measurements

Room temperature X-ray powder diffraction (XRPD) patterns were collected on a PANalytical X'Pert PRO automated diffractometer with transmission geometry equipped with Focusing mirror and Pixcel detector in the 2θ range $5-90^\circ$ (step size 0.0130° , time/step 118.32 s, VxA 40kV x 40mA). Data analyses were carried out using the Panalytical X'pert Highscore Plus program. The identity between the bulk material obtained via solution and solid-state processes was always verified by comparing calculated and observed powder diffraction patterns.

Synchrotron radiation-XRPD measurements of CA·LiCl and CA·NaCl were performed at the Swiss Light Source (SLS) Material Science (MS) Powder Diffraction (PD)²⁷ end station with a nominal photon energy of 17KeV. Fine Si640D NIST standard refinement returned a wavelength of $0.709703(2)\text{\AA}$ and a residual Zero Error of $2\theta = 0.0048(4)^\circ$. Data were collected with a 1D Mythen II detector²⁸ in the range $2-120^\circ 2\theta$, with intrinsic step size of $0.0036 (2\theta)$. Samples were loaded in 0.5 mm glass capillaries and spun at

4Hz during the measurement. Multiframing data were recorded in transmission with an exposure time of 5 seconds to avoid radiation damage; the raw data were then individually inspected before being merged together and flat field corrected.

Structural determination of CA·LiCl.

Laboratory data were preliminarily used to determine the crystal structure. Powder diffraction data were analysed with the software X'Pert HighScore Plus²⁹ and unit cell parameters were found using DICVOL4 or DICVOL algorithms. Initially CA·LiCl was indexed in the cubic system with a unit cell volume of 161.79 Å³. The cell volume corresponds to the volume of 1x(LiCl C₃N₃O₃H₃), hence the structure was solved in the triclinic space group P1 by simulated annealing, performed with EXPO2014,³⁰ using Li and Cl atoms, and one molecule of cyanuric acid. Ten runs for simulated annealing trial were set, and a cooling rate (defined as the ratio T_n/T_n⁻¹) of 0.95 was used. The Platon³¹ ADDSYMM SHELX command was subsequently applied, and data were transformed into the trigonal space group R3m.

The Rietveld refinement was subsequently performed with TOPAS 5.0³² in the R3m space group on *synchrotron* data measurement in the range 2θ=6.6-70.5°. A shifted Chebyshev function with 10 parameters was used to fit the background and two extra peaks to describe the halos of the amorphous material. The peak shape was modelled for size and strain with the Gaussian and Lorentzian functions present in TOPAS 5.0 and the anisotropic peak broadening was modelled as described by Stephens.³³

The excess of LiCl used in the reaction was identified as LiCl·H₂O monohydrate, which was refined on the basis of the known crystal structure (see Figure ESI-1).

The refinement converged to R_{wp}=4.89 % and R_p= 4.63%.

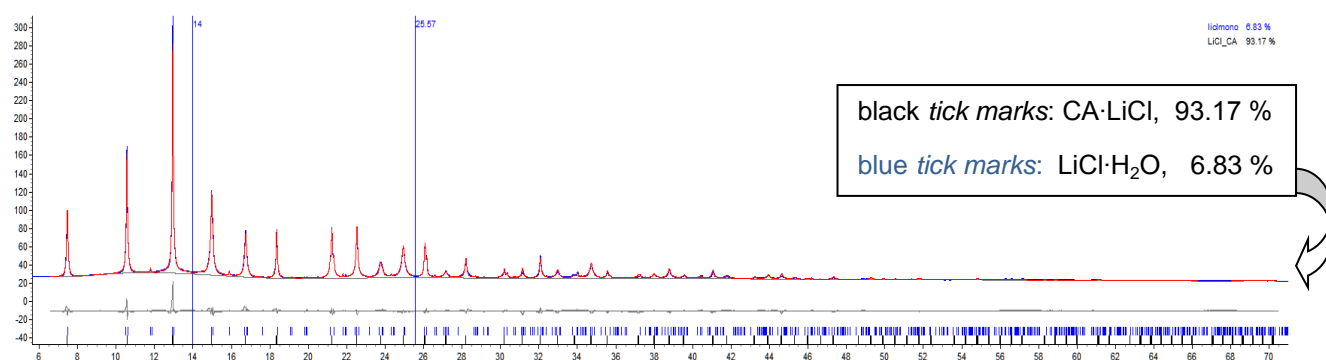


Figure ESI-1.: Rietveld analysis plot of CA·LiCl. Red line is the calculated diffractogram, blue line is the observed diffractogram and grey line is the difference plot. Blue and black tick marks corresponds to CA·LiCl and LiCl·H₂O respectively. Y-axis is reported as \sqrt{y} .

The powder pattern of CA·NaCl was indexed in the hexagonal system, space group $P6_3mc$, with a volume cell of 325.231 \AA^3 and a plausible solution was found with EXPO 2014 with the simulated annealing algorithm. The structure was analysed with Platon, ADDSYMM SHELX command was applied and a unit cell of a higher symmetry was found. Afterwards, the structure described with $P6_3/mmc$ symmetry was used for Rietveld refinements in the range $2\theta=5-90^\circ$, which were performed with the software TOPAS 5.0. The background was described by modelling the empty capillary and by the Chebyshev function with 2 parameters. The peak shape was modelled for size and strain with the Gaussian and Lorentzian functions present in TOPAS 5.0.

A small quantity of NaCl present was identified in the product pattern, and its profile was refined on the basis of the known crystal structure (see Figure ESI-2).

The refinement converged to $R_{wp}=4.55 \%$ and $R_p= 4.03\%$.

Structural data for are listed in Table ESI-1.

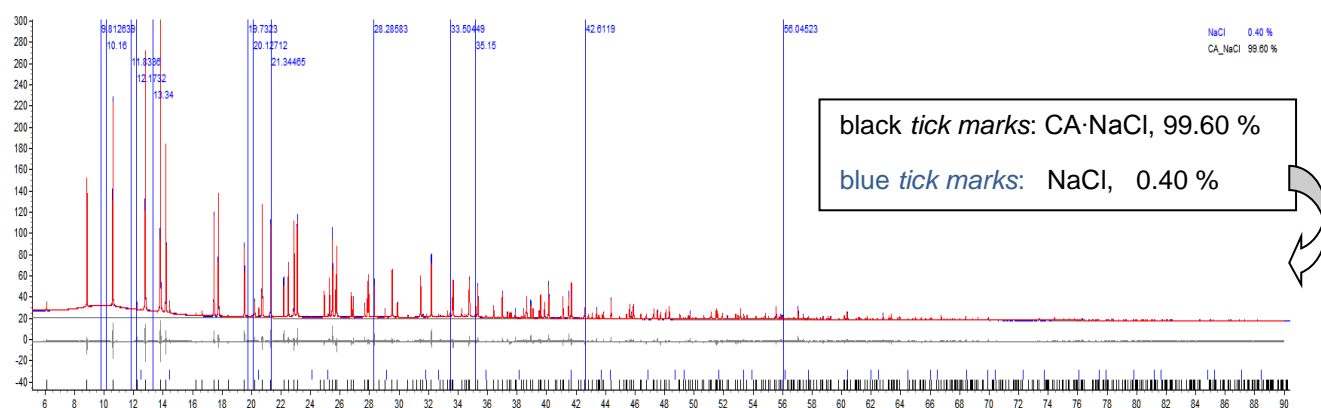


Figure ESI-2. : Rietveld analysis plot of CA·NaCl. Red line is the calculated diffractogram, blue line is the observed diffractogram and grey line is the difference plot. Black and blue tick marks corresponds to CA·NaCl and NaCl respectively. Y-axis is reported as \sqrt{y} .

Table ESI-1. Structural data for CA·LiCl and CA·NaCl.

	CA·LiCl	CA·NaCl
Formula	C ₃ H ₃ N ₃ O ₃ LiCl	C ₃ H ₃ N ₃ O ₃ NaCl
Fw (g mol ⁻¹)	171.47	187.52
Crystal system	Trigonal	Hexagonal
Space group	R3m	P6 ₃ /mmc
Z	3	2
a (Å)	7.7079(1)	7.6807(1)
b (Å)	7.7079(1)	7.6807(1)
c (Å)	9.4483(3)	6.3662(1)
α (°)	90.0	90.0
β (°)	90.0	90.0
γ (°)	120.0	120.0
V (Å ³)	486.1(1)	325.23(1)
R_wp	4.9	4.5

The programs Vesta³⁴, Schakal³⁵ and Mercury³⁶ were used for graphical representations of the structures. Crystal data can be obtained free of charge *via* www.ccdc.cam.ac.uk/conts/retrieving.html (or from the Cambridge Crystallographic Data Centre, 12 Union Road, Cambridge CB21EZ, UK; fax: (+44)1223-336-033; or e-mail: deposit@ccdc.cam.ac.uk). CCDC numbers 1524847 and 1524848 for CA·LiCl and CA·NaCl, respectively.

Thermogravimetric Analysis (TGA)

TGA measurements were performed using a Perkin-Elmer TGA7 in the temperature range 30-400 °C under an N₂ gas flow, at a heating rate of 5 °C min⁻¹.

Intrinsic dissolution test for CA·NaCl.

Dissolution rate in ultrapure water solution at room temperature was performed for cyanuric acid and CA·NaCl. Measurements were carried out using a Varian Cary 50 spectrophotometer equipped with a fiber optic dip probe. Absorbance of the solutions was continuously measured during 2 minutes.

Solubility test for CA·NaCl.

A small amount of CA·NaCl was weighed, and portions of it were added to a test tube containing 1mL of water at room temperature, and shaken until the solid was completely dissolved. The procedure was repeated until no more CA·NaCl could be

dissolved. The remaining co-crystal was weighed and the difference with the initial quantity calculated as the amount of the co-crystal dissolved. The experiment was repeated 3 times and the average value was used.

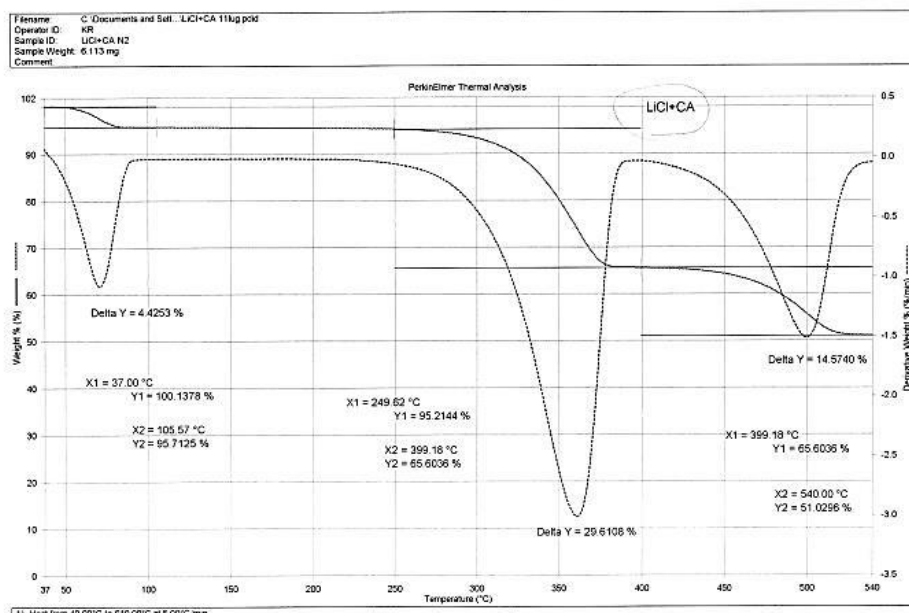


Fig. ESI-3. TGA trace for CA·LiCl as obtained from the solid-state reaction. The first weight loss corresponds to excess water adsorbed on the crystals surface, due to the excess of LiCl used in the reaction, which, upon desiccation in the oven, forms monohydrated LiCl (see Fig. ESI-1). The upper solid line, parallel to the x-axis and used to mark the first loss of water, incorrectly suggests that a plateau is present between 37 and 50°C. For this reason the derivative curve has been traced (dotted curve), which shows how water release is active already at 37°C, i.e. at the beginning of the measurement (thus indicating loss of surface water, that is followed by release of crystallization water from LiCl·H₂O).

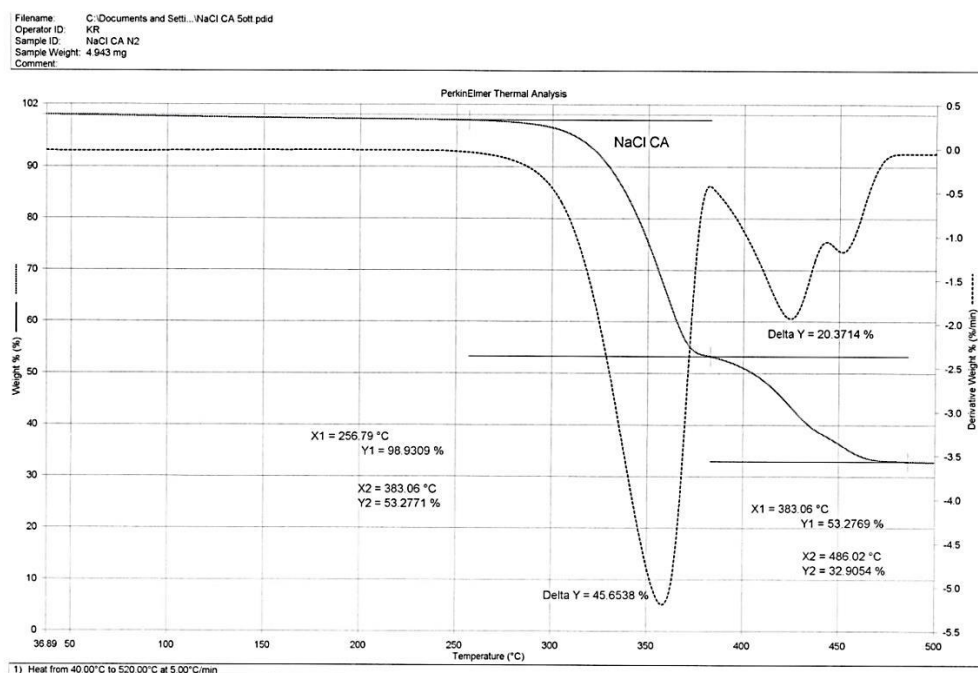


Fig. ESI-4. TGA trace for CA·NaCl as obtained from the solid-state reaction.

3.2.3. Ionic co-crystals of cyanuric acids with the rest of alkali halides.

Cyanuric acid easily forms ionic co-crystals with alkali halides (see introduction, table 3.2.1-1). All ICCs were obtained by mechanical mixing of solid CA and of the alkali salts by *kneading* the solid mixture with the addition of a small quantity of solvent. Similar to ICCs of cyanuric acid with LiCl and NaCl, crystallization from solvent (ethanol, methanol and water) failed to yield crystals suitable for single crystal investigation. The only exception was CA·KI·H₂O, which yielded single crystals suitable for structure determination. The lack of single crystals motivated us to determine the structures from powder diffraction data alone.

As it was observed for CA·LiCl and CA·NaCl, the majority of the ICCs discussed here are anhydrous. This phenomenon as such is rather unusual since the majority of ICCs of alkali halides prepared this far tend to form hydrates¹, which in some cases can be subsequently dehydrated.²⁴ We attribute this difference to the peculiar structure of CA, which is small and highly symmetrical affording optimal packings with spherical ions without a need to fill the metal cations coordination sphere with water molecules, as it will be apparent in the following.

The interaction of CA with alkali chlorides

To start with, the ICCs of a general formula MCl (M = Li, Na, Rb, Cs) can be examined in details. The interaction of CA with alkali chloride salts formed by the smallest cations of the group resulted into formation of crystals of high

symmetry¹². The peculiarities of the crystal structures of CA·LiCl and CA·NaCl have been already discussed in the previous chapter (3.2.2).

The use of bigger cations (Rb^+ and Cs^+) results in a change of stoichiometry of the co-crystals with the doubling of the number of CA molecules involved in the crystal structures. As a result, isomorphous $\text{CA}_2\cdot\text{RbCl}$ and $\text{CA}_2\cdot\text{CsCl}$ were obtained (fig. 3.2.3-1).

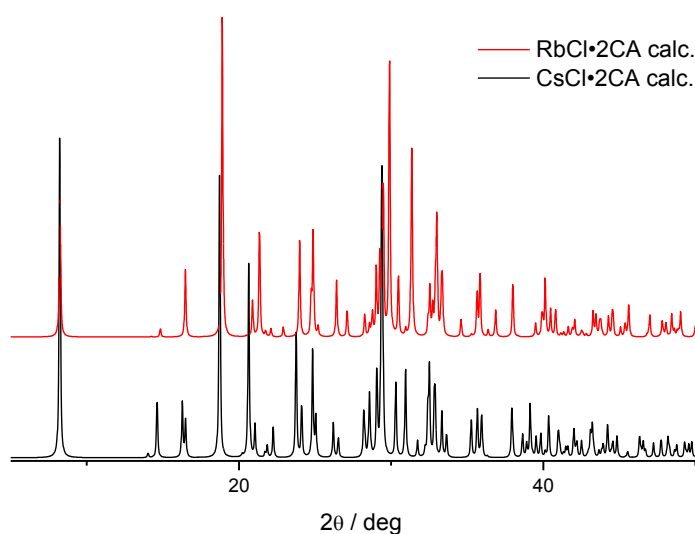


Figure 3.2.3-1 XRPD of $\text{CA}_2\cdot\text{RbCl}$ and $\text{CA}_2\cdot\text{CsCl}$

Both ICCs crystallize in the monoclinic system. Rb/Cs cation is coordinated by six different molecules of CA and with three Cl^- anions (fig. 3.2.3-2). If we divide the molecule of a CA into three equal $\text{O}=\text{C}-\text{NH}$ fragments it becomes obvious that two such fragments interact with RbCl whereas the third one interacts with another molecule of CA via hydrogen bonds.

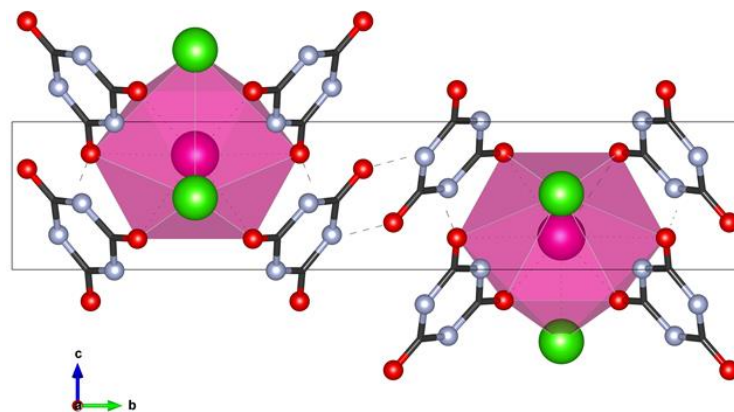


Figure 3.2.3-2 $\text{CA}_2 \cdot \text{RbCl}$. View down crystallographic a -axis (top); hydrogen bonds between CA_2 molecules. Hydrogen atoms are not shown for clarity

Interestingly, $\text{CA}_2 \cdot \text{RbCl}$ and $\text{CA}_2 \cdot \text{CsCl}$ showed different susceptibility towards moisture. The former appeared to be quite stable at room temperature whereas the latter adsorbed water from the atmosphere. Besides the fact that it became sticky, its XRPD pattern showed the presence of some new peaks (fig. 3.2.3-3). Taking into account the fact that it was possible to reobtain the initial XRPD pattern upon heating the sample in the oven it could be assumed that those peaks correspond to the hydrated form of the ICC of CA with CsCl.

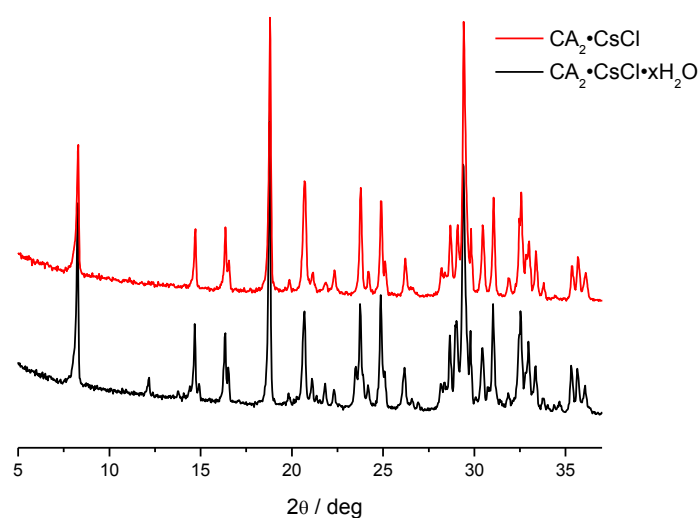


Figure 3.2.3-3 $\text{CA}_2 \cdot \text{CsCl}$. The comparison between XRPD patterns of $\text{CA}_2 \cdot \text{CsCl}$ analysed immediately after being synthesized (red) and in 24h (black).

Table 3.2.1-1 reports also an intriguing negative result. So far it has proven impossible to obtain an ICC of CA with KCl. Despite the numerous attempts to synthesize CA·KCl, all our efforts appeared to be unsuccessful: the methods that yielded the other co-crystals (kneading with ethanol, H₂O and methanol) failed to give the ICC of cyanuric acid with KCl. Attempts to introduce other alkali salts which formed ICCs with CA in a kind of pseudo seeding to induce the formation of CA·KCl failed as well. In all cases (NaCl and KBr) the peaks of the corresponding co-crystals along with unreacted CA and KCl were observed. Taking into account the information given above one is brought to think that the cation size plays a crucial role. The K⁺ cation is, on the one hand, too big to form an ICC with CA in 1:1 ratio (as in the case of Li⁺ and Na⁺), while, on the other hand, it is still too small to form a co-crystal in 1:2 ratio similar to the ones of RbCl and CsCl.

The interaction of CA with alkali bromides

Ball milling preparations of ICCs with Br⁻ as an anion were much faster than with the Cl⁻ anion. For example, the reaction of a mixture NaCl (1 mole) and NaBr (1 mole) with CA (2 moles) yielded quantitative formation of CA·NaBr (1 mole) within 15 minutes while CA (1 mole) and NaCl (1 mole) were still unreacted.

All the ICCs with alkali bromide present a 1:1 stoichiometry. The co-crystallization of cyanuric acid with LiBr resulted in the formation of a new phase. Unfortunately, we have not been able to solve its structure so far. However, based on the obtained XRPD pattern it can be asserted that its structure is completely different from CA·LiCl. In addition, TGA analysis showed

that it contains solvent molecules in its structure and since the obtained XRPD patterns were identical regardless of the solvent applied (methanol, ethanol and water) it was assumed that the hydrated product $\text{CA}\cdot\text{LiBr}\cdot n\text{H}_2\text{O}$ (see fig. 3.2.3-4) was formed.

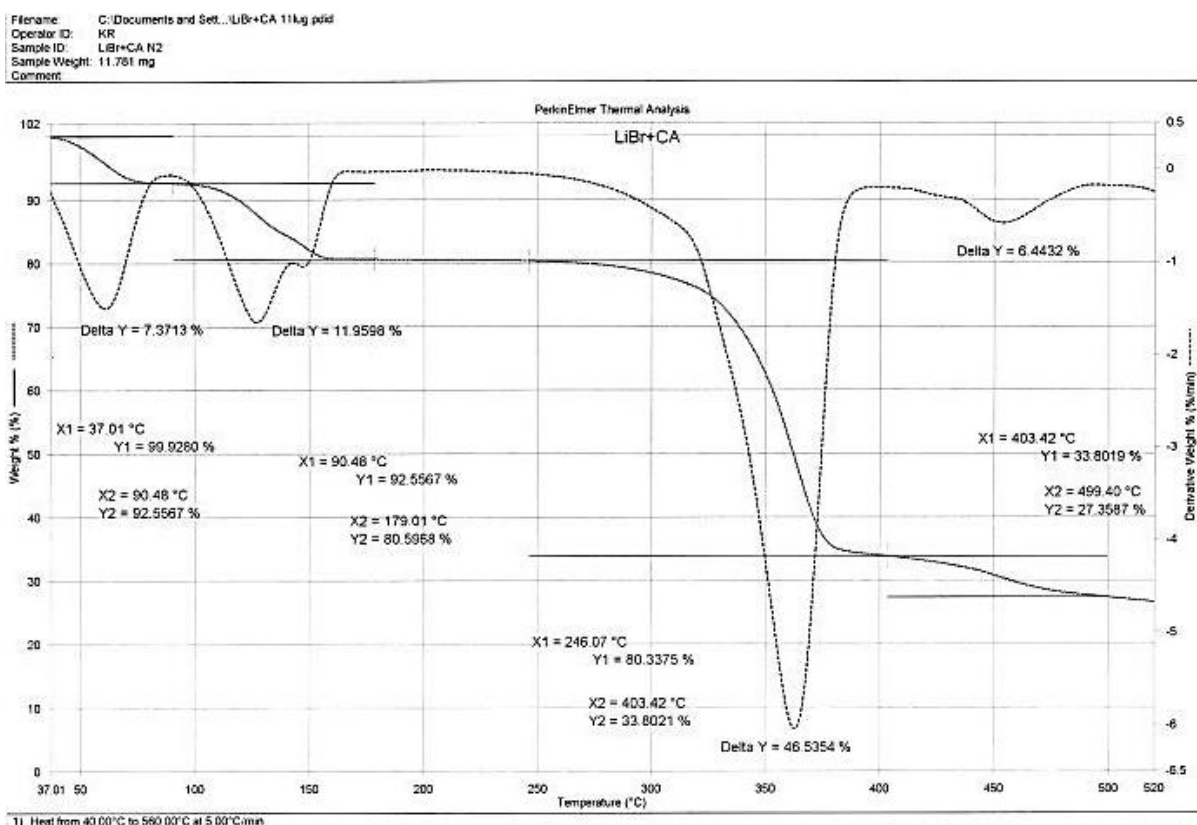
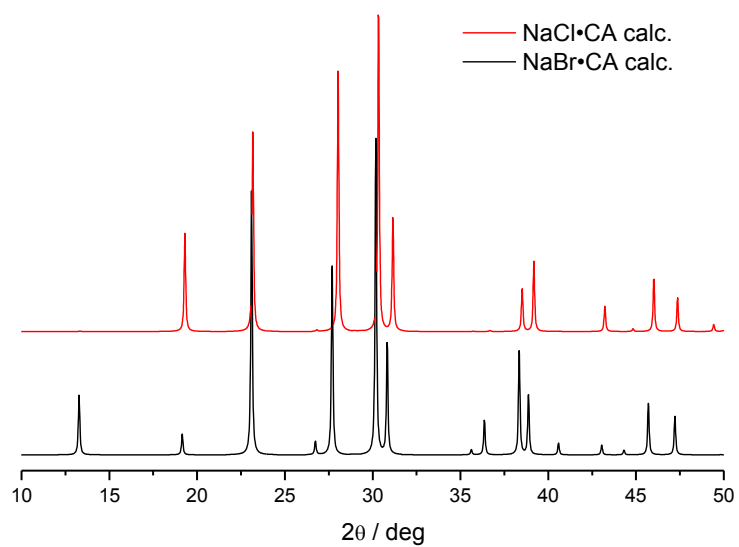
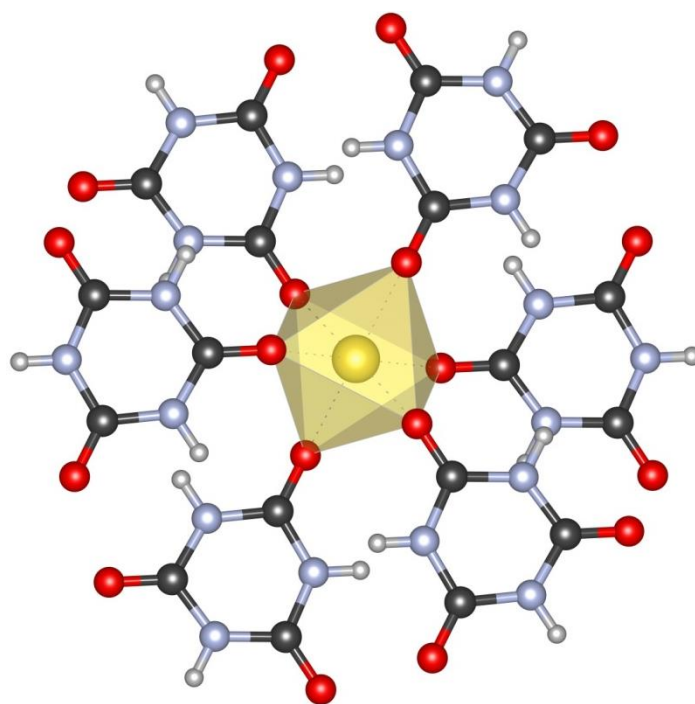


Figure 3.2.3-4 TGA traces of $\text{CA}\cdot\text{LiBr}\cdot n\text{H}_2\text{O}$

The interaction of NaBr with CA appeared to be dependent on the solvent applied. Ball milling of the equimolar quantities of sodium bromide with cyanuric acid using methanol or ethanol as a solvent resulted into the formation of anhydrous $\text{CA}\cdot\text{NaBr}$ which is isomorphous (fig. 3.2.3-5 (a)) to $\text{CA}\cdot\text{NaCl}$ (XAKSUA¹²). However, if the same experiment is performed using catalytic quantities of water, the obtained product was hydrated $\text{CA}\cdot\text{NaBr}\cdot 2\text{H}_2\text{O}$ (3.2.3-6).



(a)



(b)

Figure 3.2.3-5 (a) XRPD of CA·NaCl and CA·NaBr; (b) Na^+ coordination in CA·NaBr

The Na^+ cation in $\text{CA}\cdot\text{NaBr}\cdot 2\text{H}_2\text{O}$ as well as in $\text{CA}\cdot\text{NaBr}$ shows octahedral coordination with three coordination sites used by molecules of CA and three filled by water molecules (Fig. 3.2.3-6).

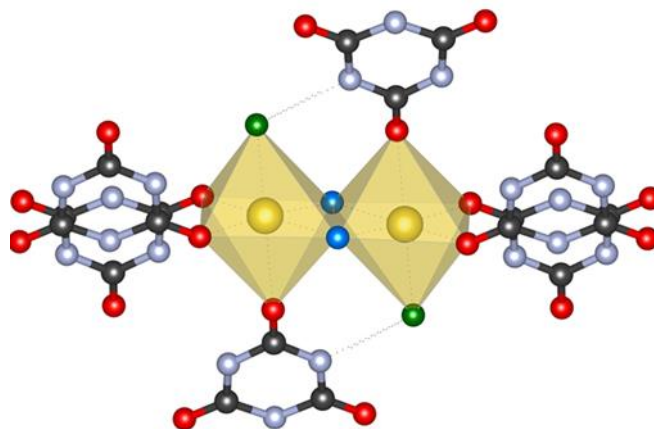


Figure 3.2.3-6 Na^+ coordination in $\text{CA}\cdot\text{NaBr}\cdot 2\text{H}_2\text{O}$. Oxygens of water molecules are marked in green and blue for clarity.

The interaction with bromide salts of larger alkali cations (K^+ , Rb^+ , Cs^+) resulted in coordination of the cations with the halide anions beside the CA molecules (fig. 3.2.3-7).

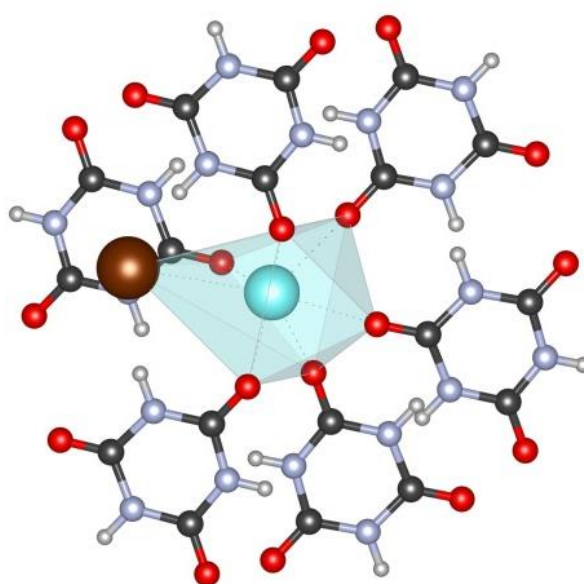


Figure 3.2.3-7 K^+ coordination in $\text{CA}\cdot\text{KBr}$

The co-crystallization of cyanuric acid with rubidium and caesium bromides produced the isomorphous co-crystals CA·RbBr and CA·CsBr. Figure 3.2.3-8 represents the crystal structure of CA·RbBr. As for the ICCs formed with sodium halides discussed above, the Rb⁺ cations of CA·RbBr have also an octahedral coordination. However, contrary to what observed with Na⁺, Rb⁺ interacts with four oxygens of different CA molecules and two anions.

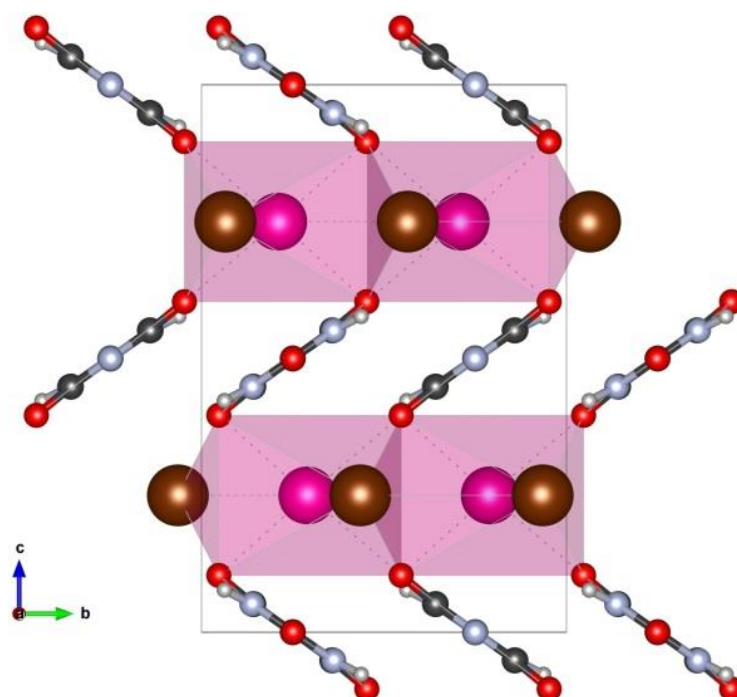


Figure 3.2.3-8 Crystal packing of CA·RbBr. View down crystallographic *a*-axis

The interaction of CA with alkali iodides

The investigation of interactions of CA with alkali iodide salts was more difficult. The reaction with LiI resulted in the formation of a new phase which was very hygroscopic. The interaction with NaI resulted into a new ICC, but its structure was not solved so far. The obtained XRPD pattern is different from those observed for CA·NaCl/NaBr or CA·NaBr·2H₂O.

The interaction of cyanuric acid with potassium iodide led to the formation of $\text{CA}\cdot\text{KI}\cdot\text{H}_2\text{O}$. Actually, it was the only case when it was possible to recrystallize the obtained ionic co-crystal and to solve its structure using single crystal data. It is a monoclinic crystal system. The coordination of K^+ is similar to the one observed in $\text{CA}\cdot\text{KBr}$ with the only difference that it interacts with four molecules of CA and the two missing coordinates are fulfilled by oxygens derived from water (fig. 3.2.3-9).

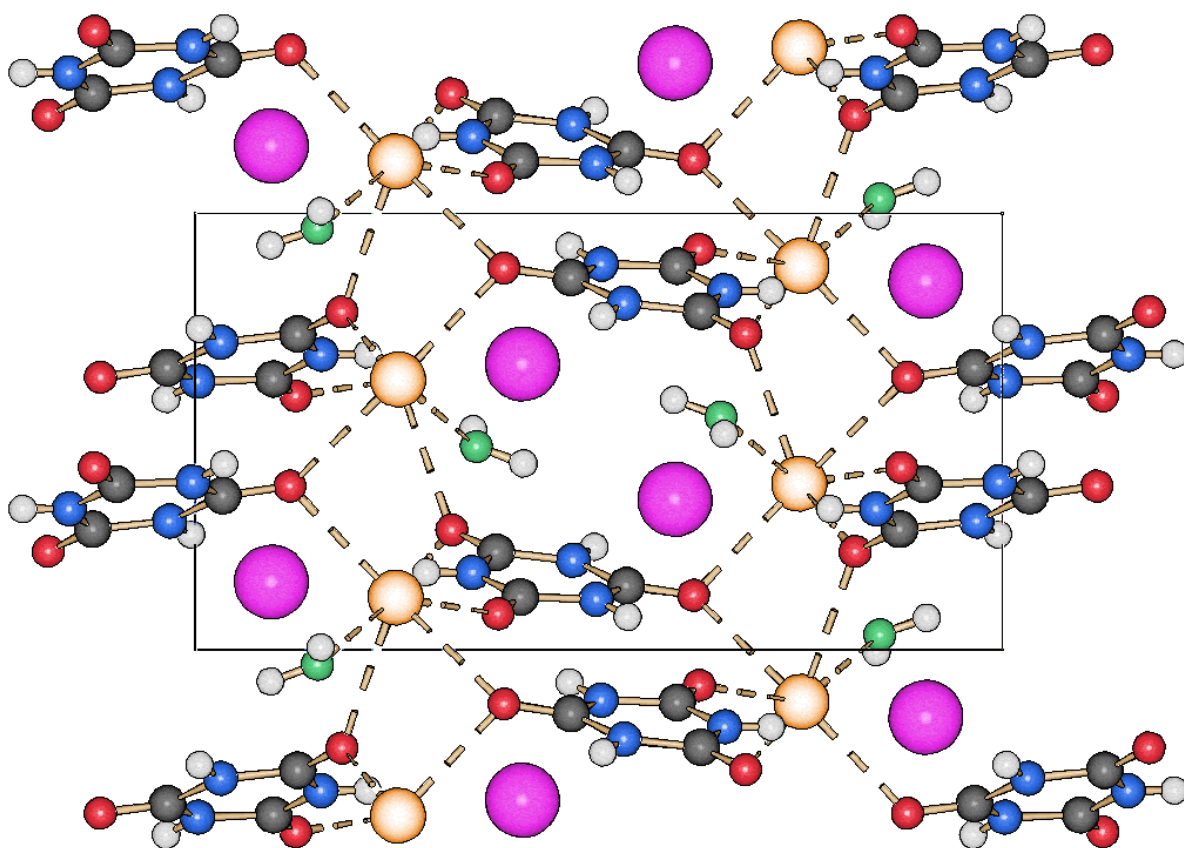


Figure 3.2.3-9 $\text{CA}\cdot\text{KI}\cdot\text{H}_2\text{O}$. Water molecules are marked in green for clarity.

The crystal structure of $\text{CA}\cdot\text{RbI}$ appeared to be isomorphous to the one of $\text{CA}\cdot\text{KBr}$ (fig. 3.2.3-10) while we have been so far unable to obtain co-crystals with CsI .

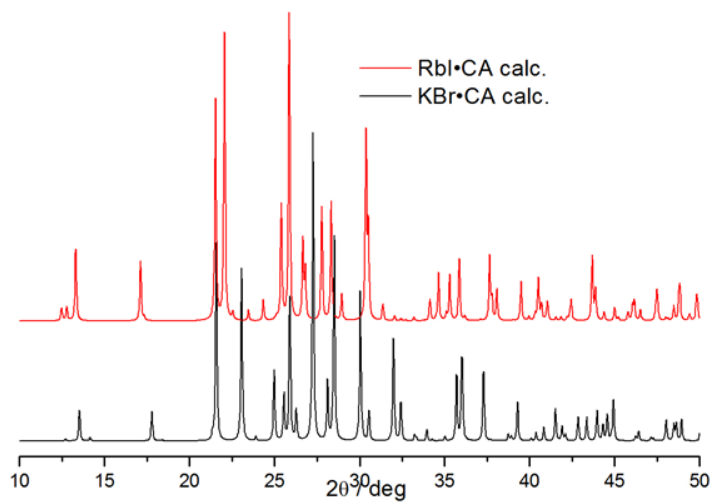


Figure 3.2.3-10 XRPD of CA·RbI and CA·KBr

3.2.4.1 Supporting Information

Table 3.2.3-1 Structural data for ICCs solved from XRPD data.

	NaBr·CA· 2H ₂ O	KBr·CA	RbBr·CA	CsBr·CA	NaBr·CA	RbCl·2CA	RbI·CA	CsCl·2CA
Formula	C ₃ H ₇ N ₃ O ₅ NaBr	C ₃ H ₃ N ₃ O ₃ KBr	C ₃ H ₃ N ₃ O ₃ RbBr	C ₃ H ₃ N ₃ O ₃ CsBr	C ₃ H ₃ N ₃ O ₃ NaBr	C ₆ H ₆ N ₆ O ₆ RbCl	C ₃ H ₃ N ₃ O ₃ R bI	C ₆ H ₆ N ₆ O ₆ CsCl
Fw (g·mol ⁻¹)	268.00	248.08	294.45	341.88	231.97	379.07	341.45	426.51
Crystal system	Triclinic	Ortho- rhombic	Ortho- rhombic	Ortho- rhombic	Hexagonal	Monoclinic	Ortho- rhombic	Monoclinic
Space group	P-1	Pnma	Pbcm	Pbcm	P6 ₃ /mmc	P2 ₁ /m	Pnma	P2 ₁ /m
a (Å)	8.52(1)	7.12(1)	8.58(1)	9.08(1)	7.69(1)	4.52(1)	7.57(1)	6.79(1)
b (Å)	7.20(1)	8.22(1)	12.88(1)	12.84(1)	7.69(1)	21.46(1)	8.24(1)	21.48(1)
c (Å)	7.86(1)	13.07(1)	6.80(1)	6.86(1)	6.43(1)	6.48(1)	13.83(1)	6.65(1)
α (°)	101.51(1)	90.0	90.0	90.0	90.0	90.0	90.0	90.0
β (°)	91.77(1)	90.0	90.0	90.0	90.0	106.68(1)	90.0	139.75(1)
γ (°)	105.04(1)	90.0	90.0	90.0	120.0	90.0	90.0	90.0
V (Å ³)	455.5(1)	766.6(1)	752.6(1)	800.6(1)	329.9(1)	603.2(1)	864.5(1)	627.2(1)
R_wp	4.94%*	5.78%	9.46%	7.62%	8.8%	8.89%	6.30%	6.65%

*3-50 2-theta flat stage

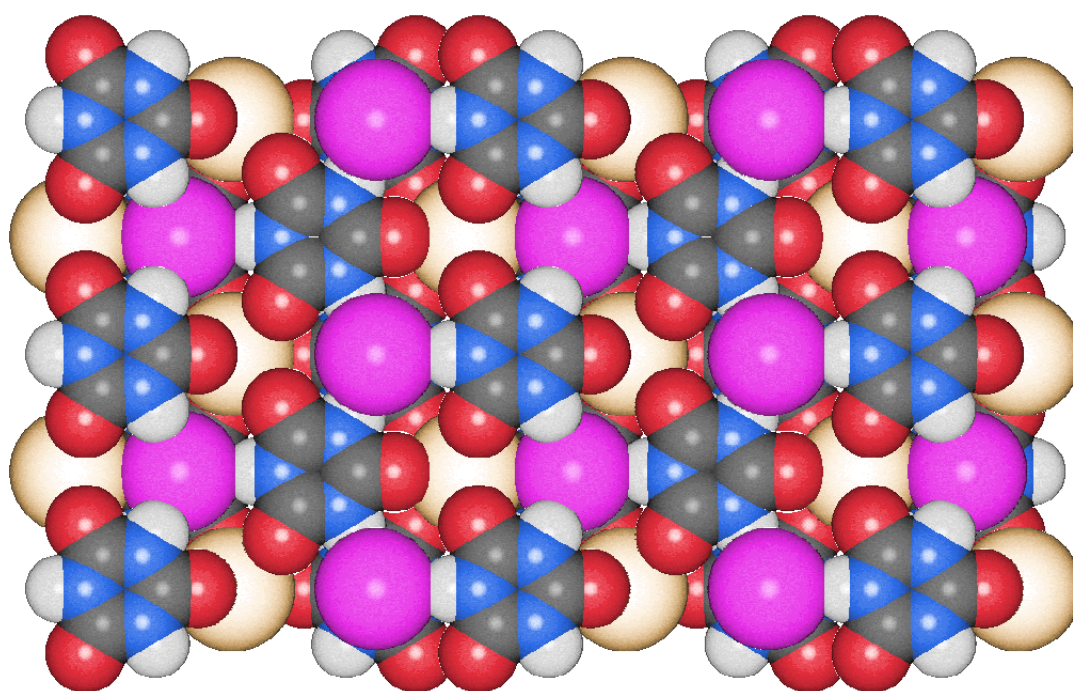


Figure 3.2.3-11 The crystal packing of CA·RbI. Rubidium cations are light brown, iodides are pink

Rietveld refinements.

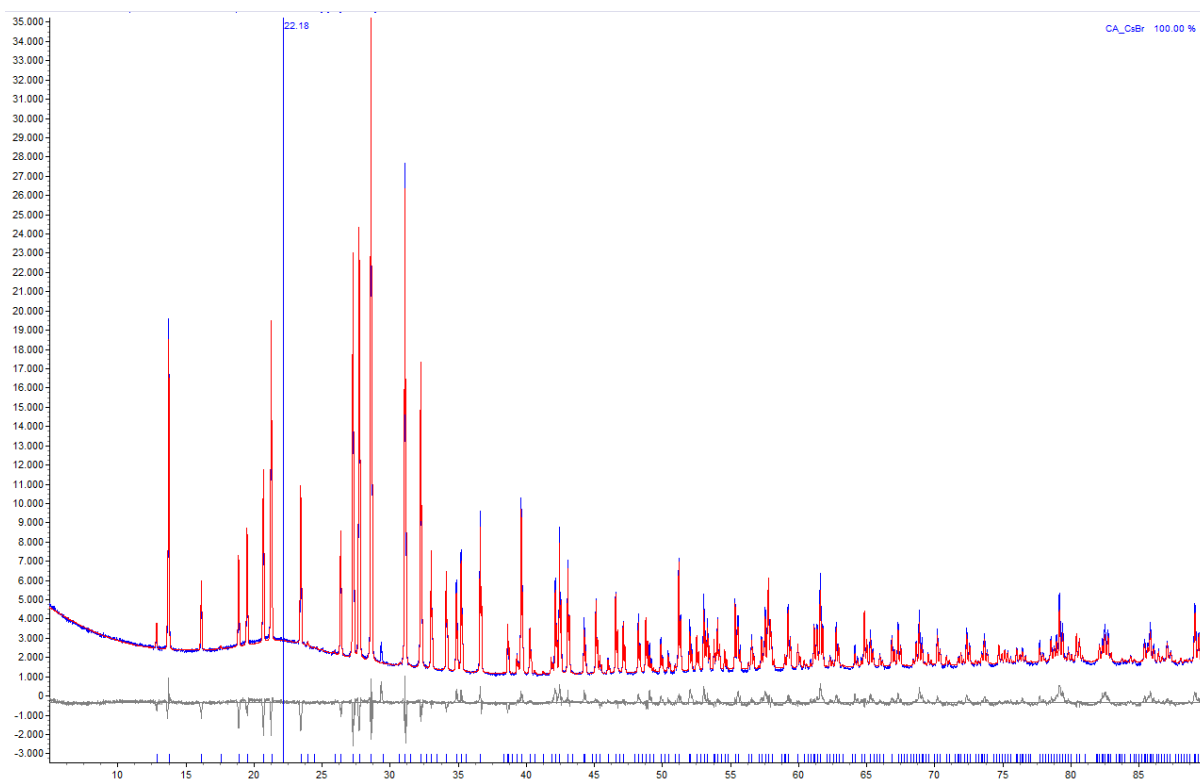


Figure 3.2.3-12 CA·CsBr.

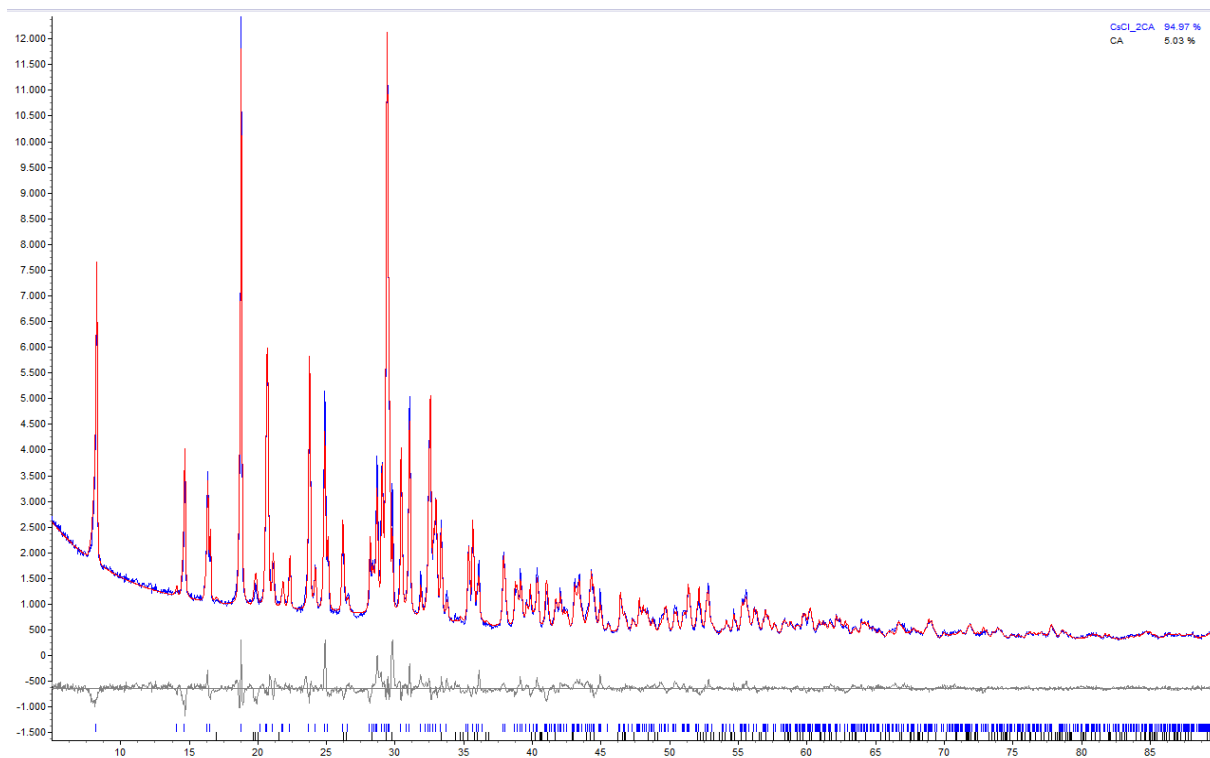


Figure 3.2.3-3 CA₂·CsCl. Some traces of cyanuric acid are present in the XRPD pattern.

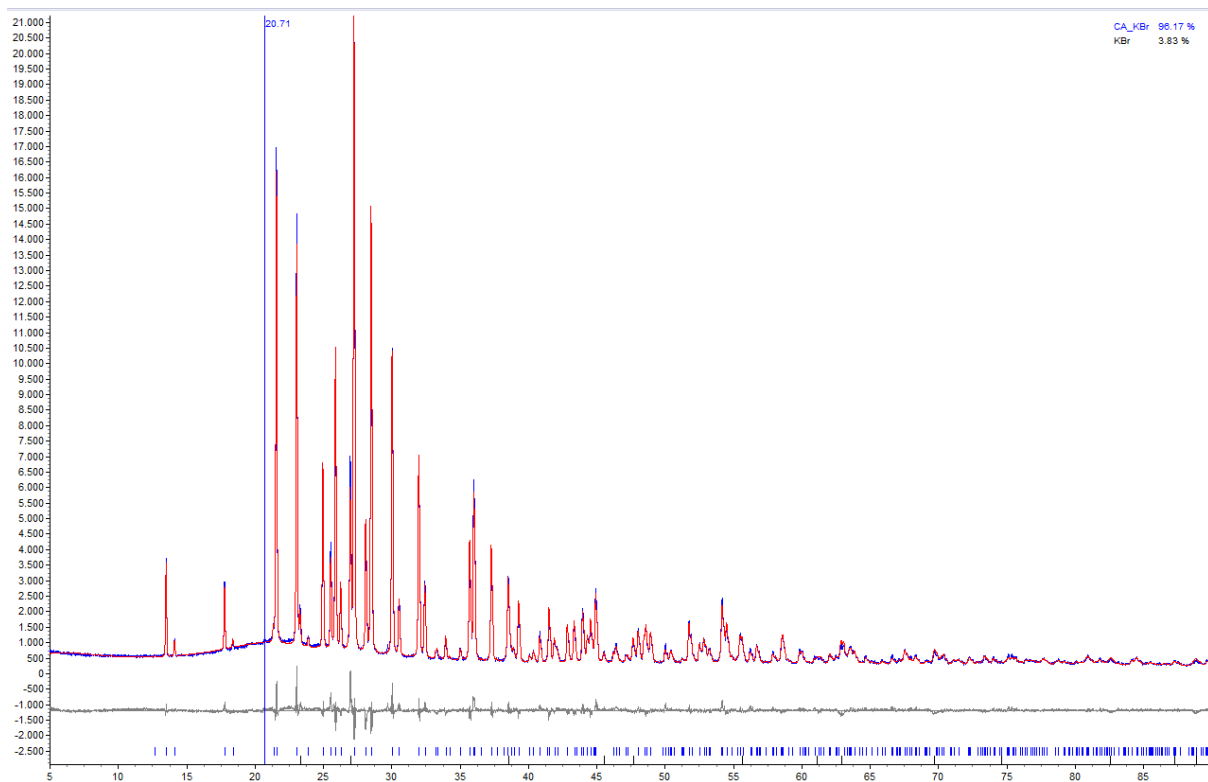


Figure 3.2.3-4 CA·KBr. Some traces of KBr are present in the XRPD pattern.

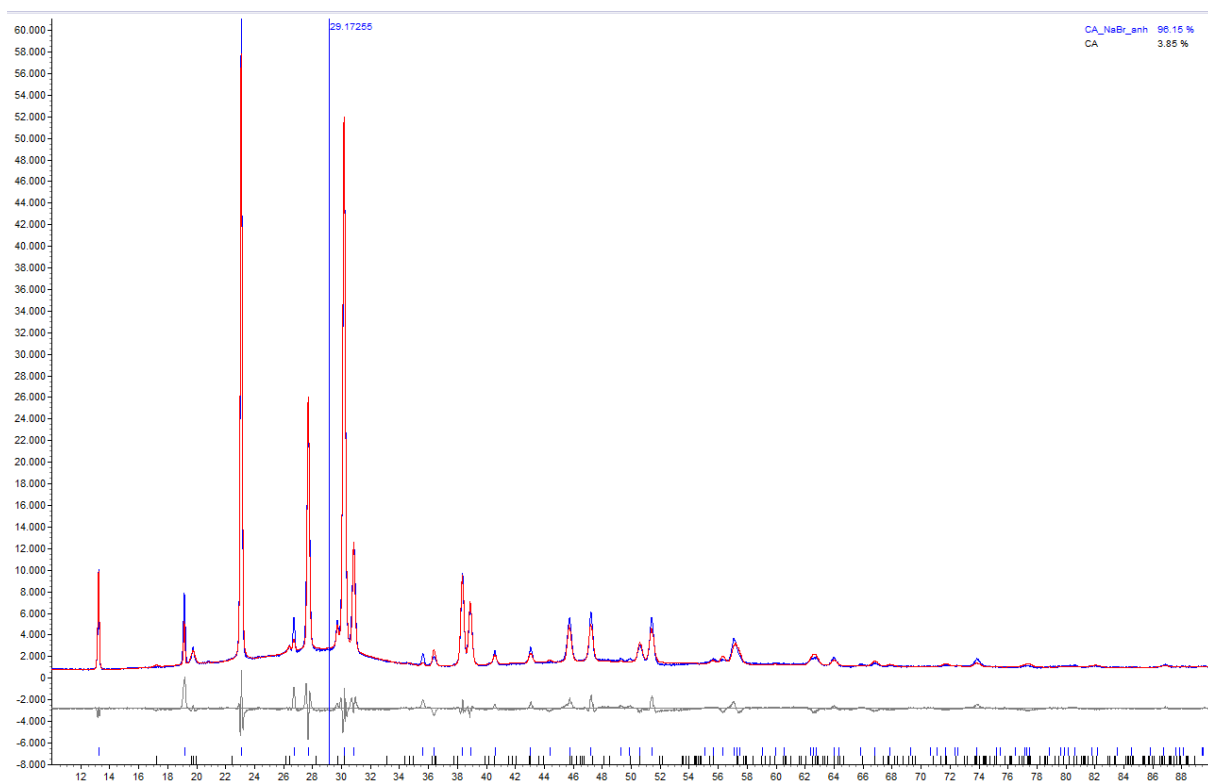


Figure 3.2.3-5 CA·NaBr. Some traces of cyanuric acid are present in the XRPD pattern.

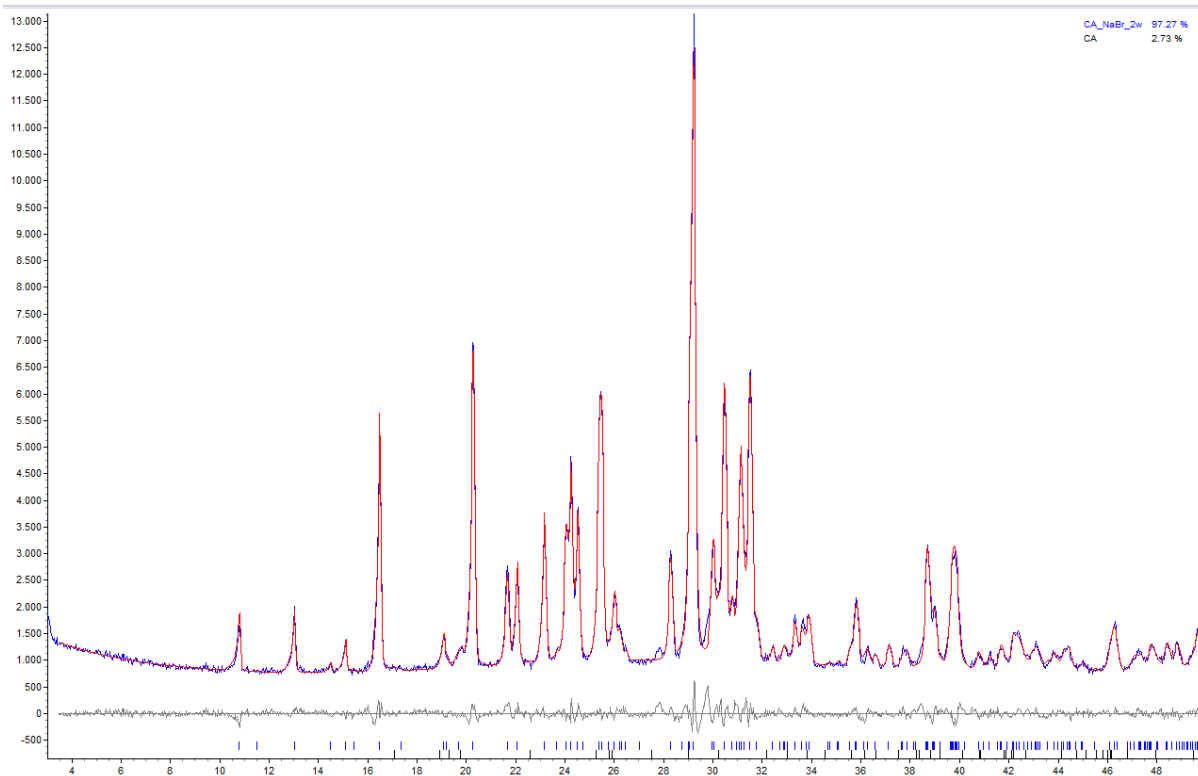


Figure 3.2.3-6 CA·NaBr·2H₂O. Some traces of cyanuric acid are present in the XRPD pattern.

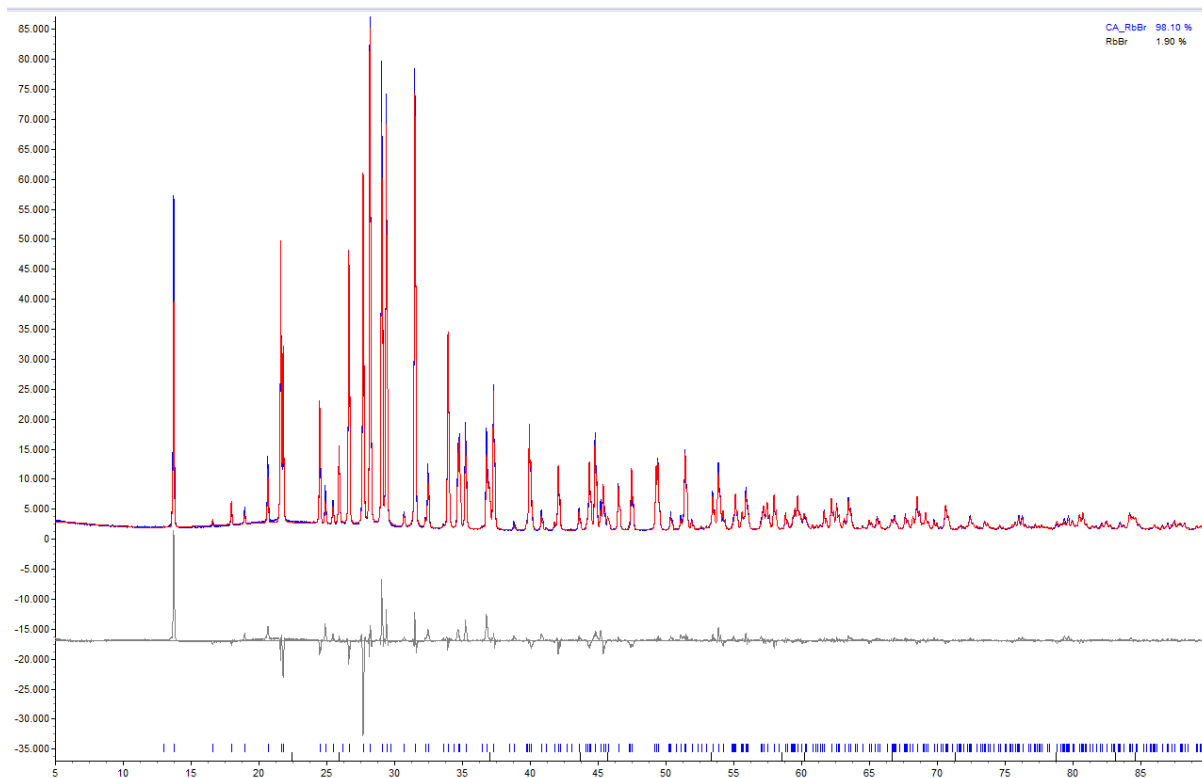


Figure 3.2.3-7 CA·RbBr. Some traces of RbBr are present in the XRPD pattern.

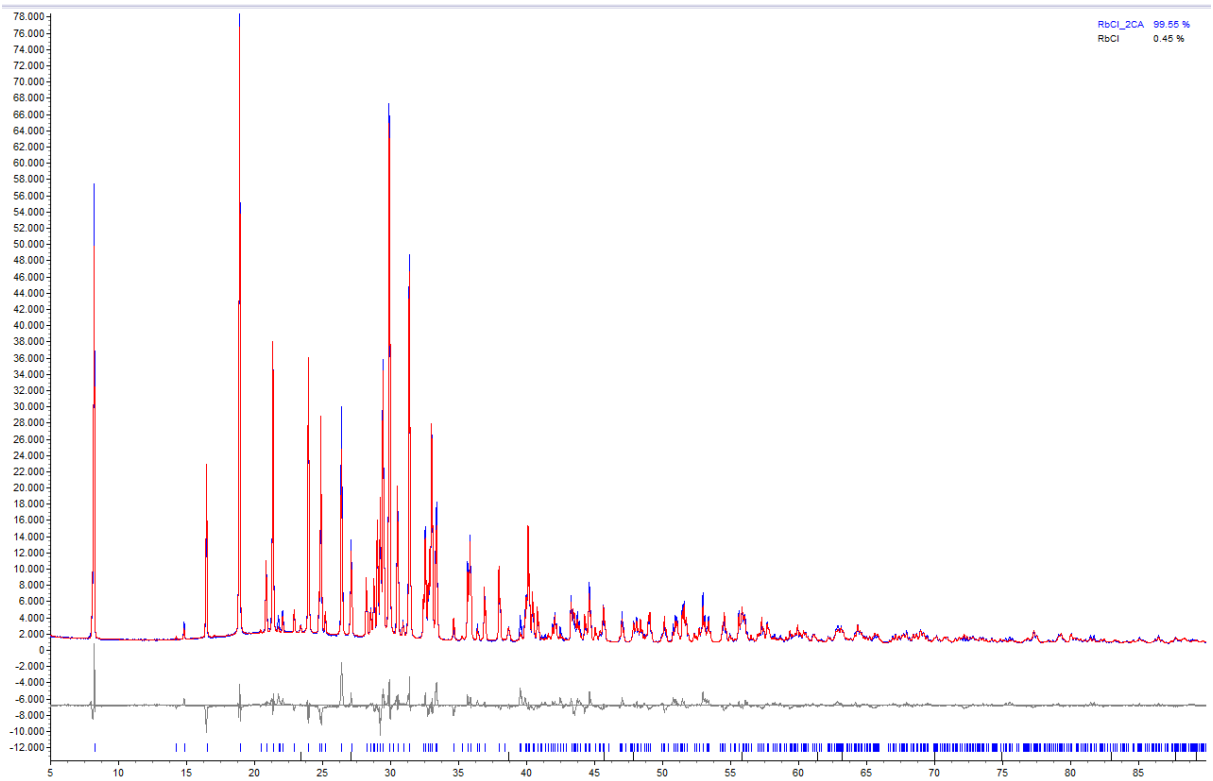


Figure 3.2.3-8 CA₂·RbCl, Some traces of RbCl are present in the XRPD pattern.

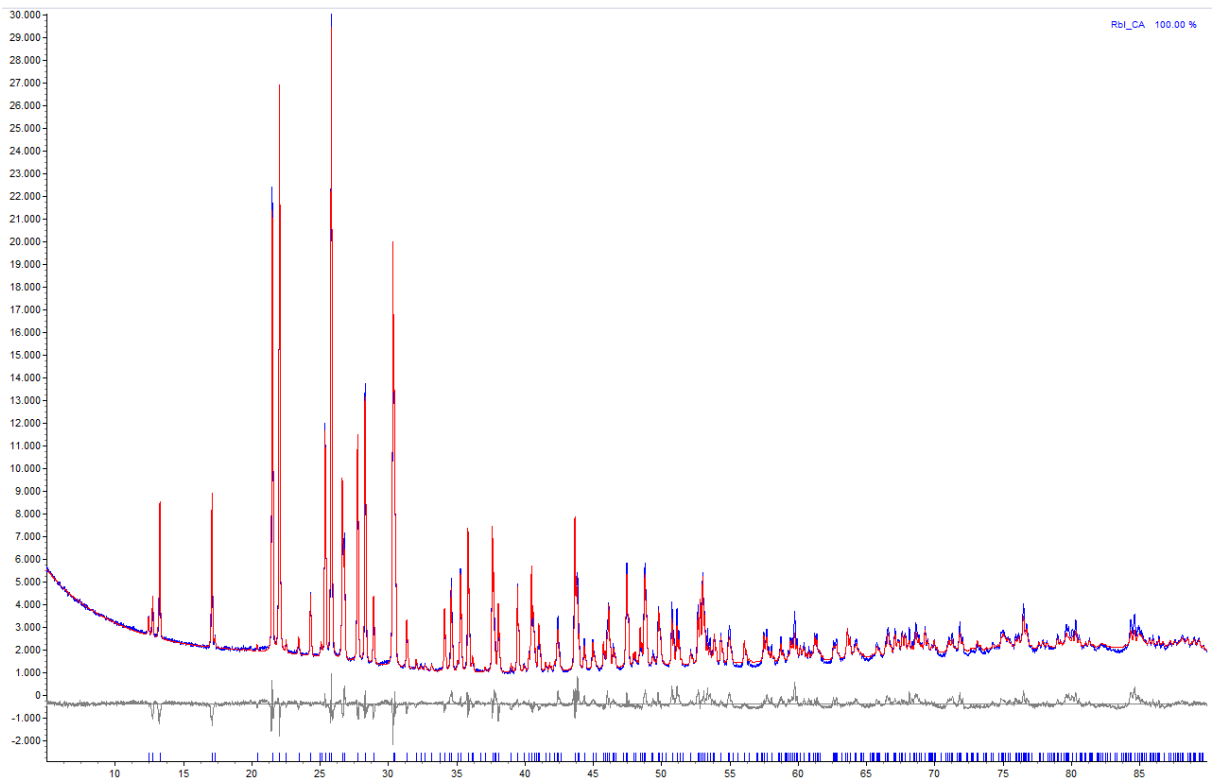


Figure 3.2.3-9 CA·RbI

Filename: C:\Program...Cyanuric Ac. CA_H 14apr.ppid
 Operator ID: KR
 Sample ID: Cyanuric Ac. CA PA
 Sample Weight: 7.510 mg
 Comment: heating

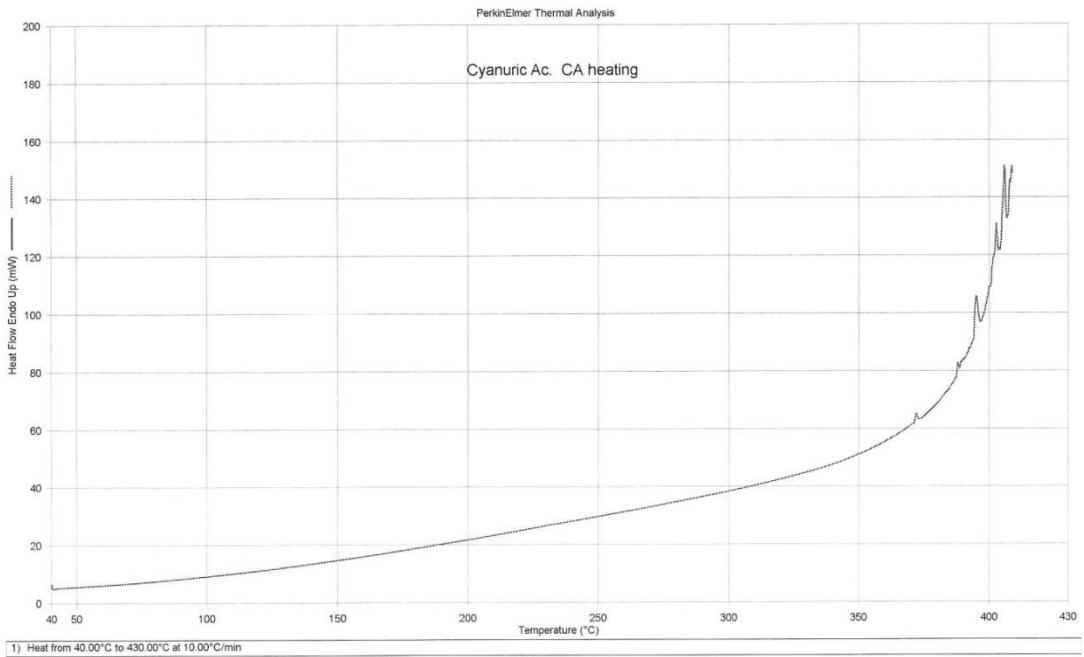


Figure 3.2.3-10 DSC trace for cyanuric acid.

Filename: C:\Program File...RbCl CA 1-2_H 14apr.ppid
 Operator ID: KR
 Sample ID: RbCl CA 1:2 PA
 Sample Weight: 5.180 mg
 Comment: heating

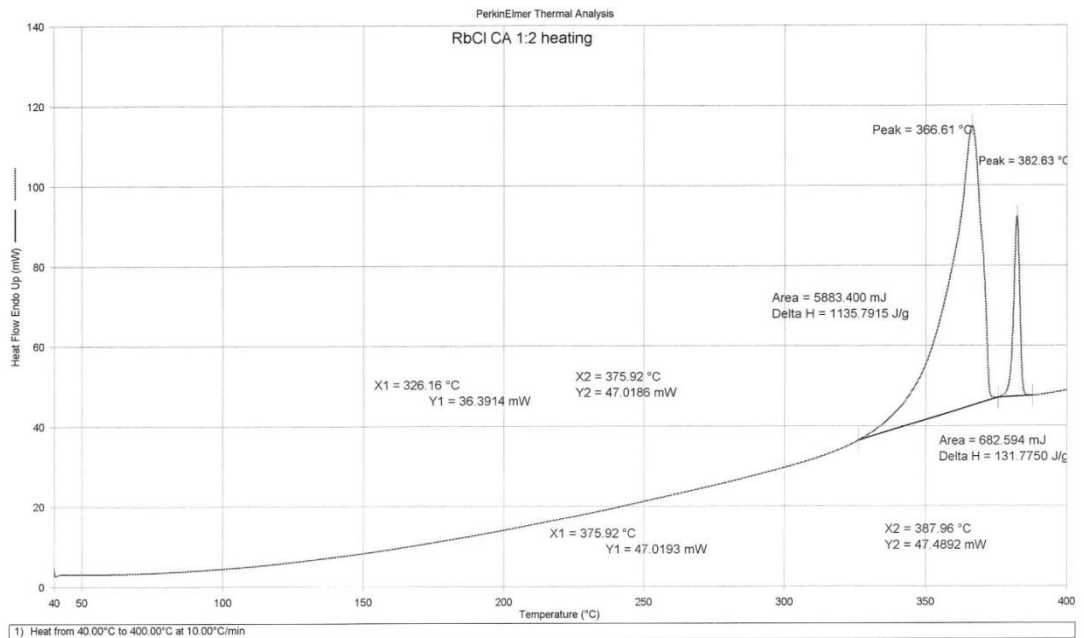


Figure 3.2.3-11 DSC trace for CA₂·RbCl.

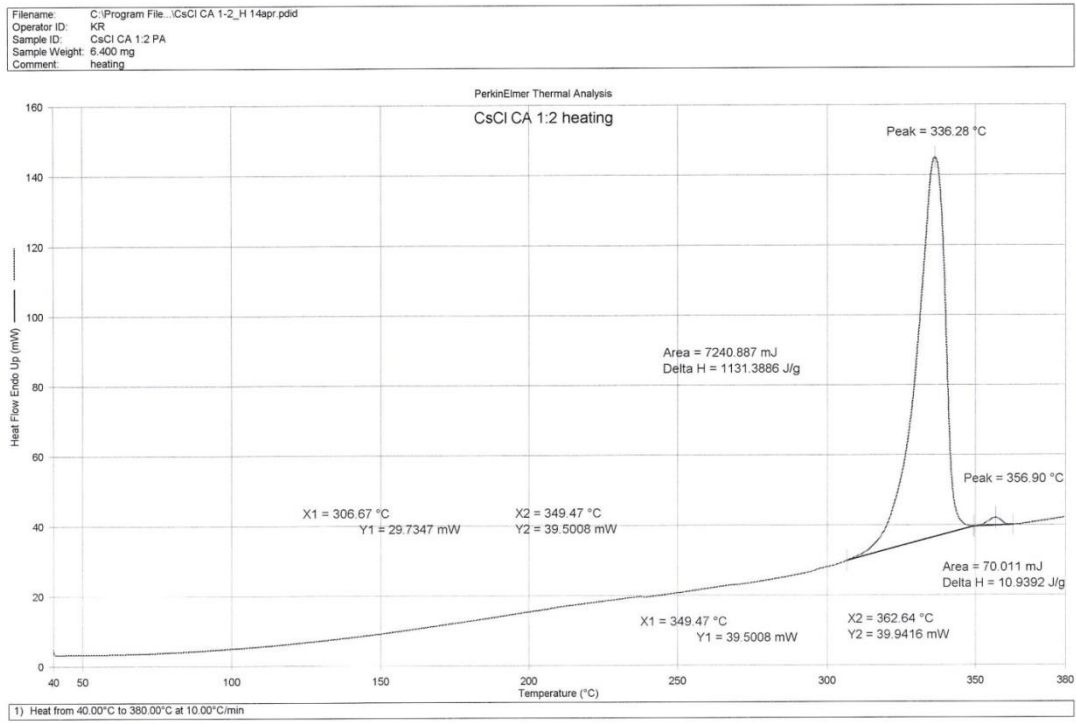


Figure 3.2.313 DSC trace for $CA_2 \cdot CsCl$.

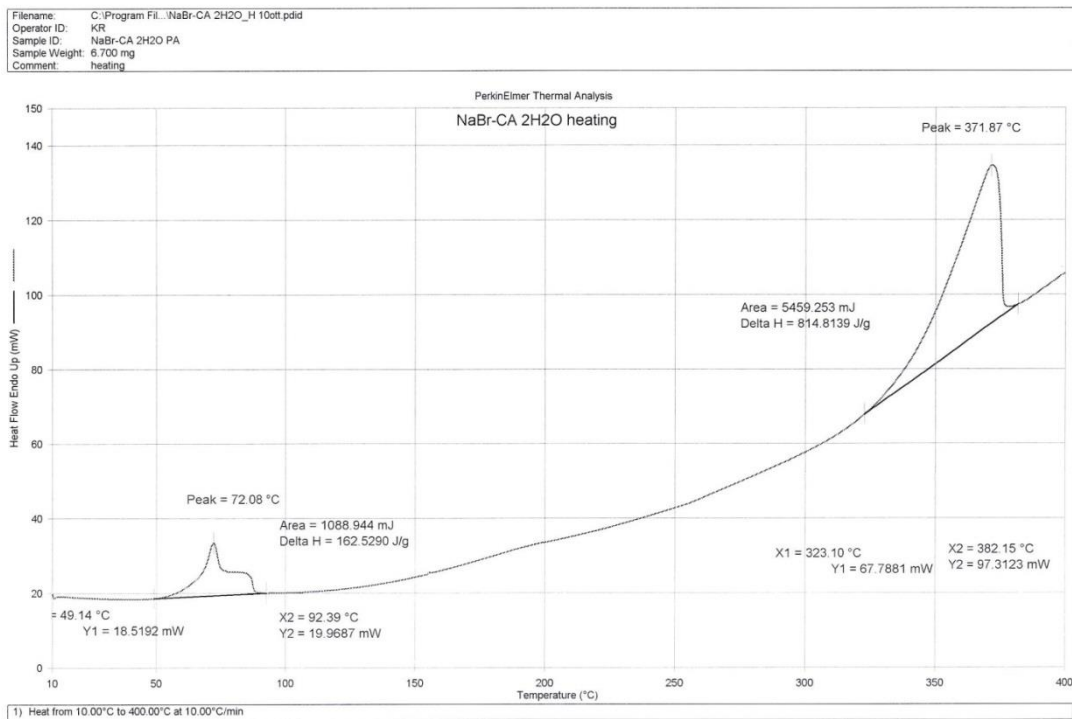


Figure 3.2.3-13 DSC trace for $CA \cdot NaBr \cdot 2H_2O$.

Filename: C:\Program Files\Pyr...\NaBr_CA_H 10mag.pdtd
 Operator ID: KR
 Sample ID: NaBr CA PA
 Sample Weight: 5.000 mg
 Comment: heating

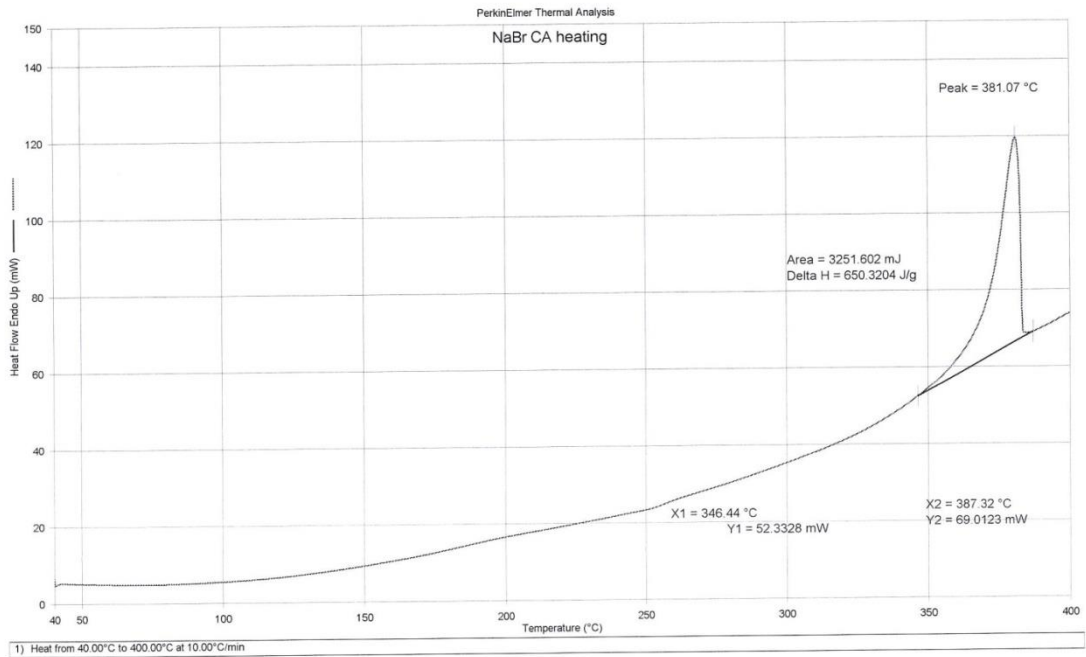


Figure 3.2.3-14 DSC trace for CA·NaBr.

Filename: C:\Program Files\Pyr...\KBr-CA_H 20ott.pdtd
 Operator ID: KR
 Sample ID: KBr-CA PA
 Sample Weight: 5.820 mg
 Comment: heating

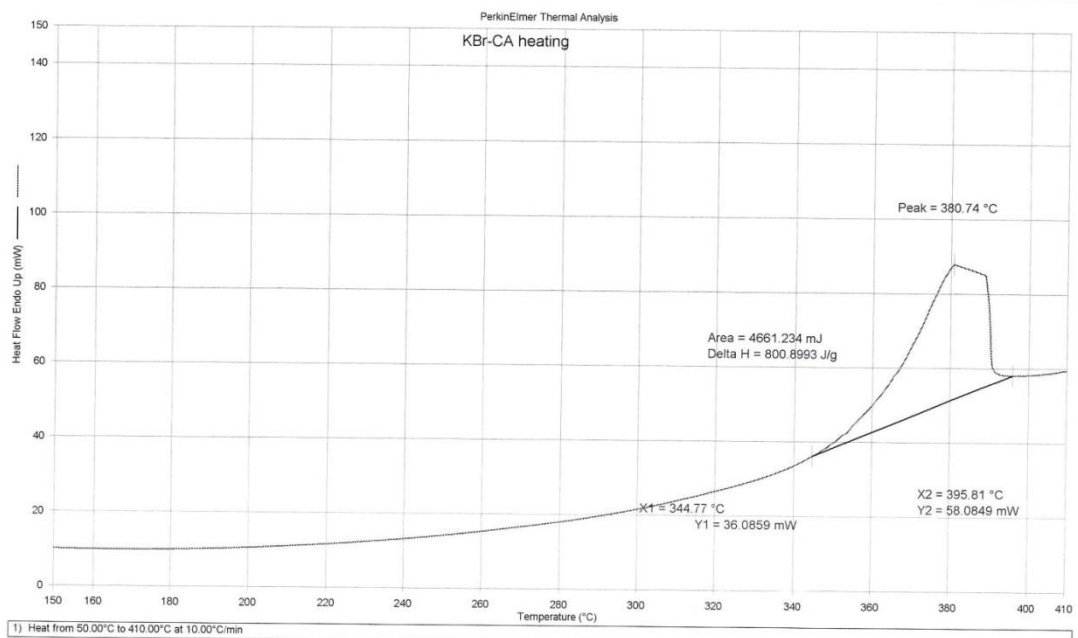


Figure 3.2.3-15 DSC trace for CA·KBr.

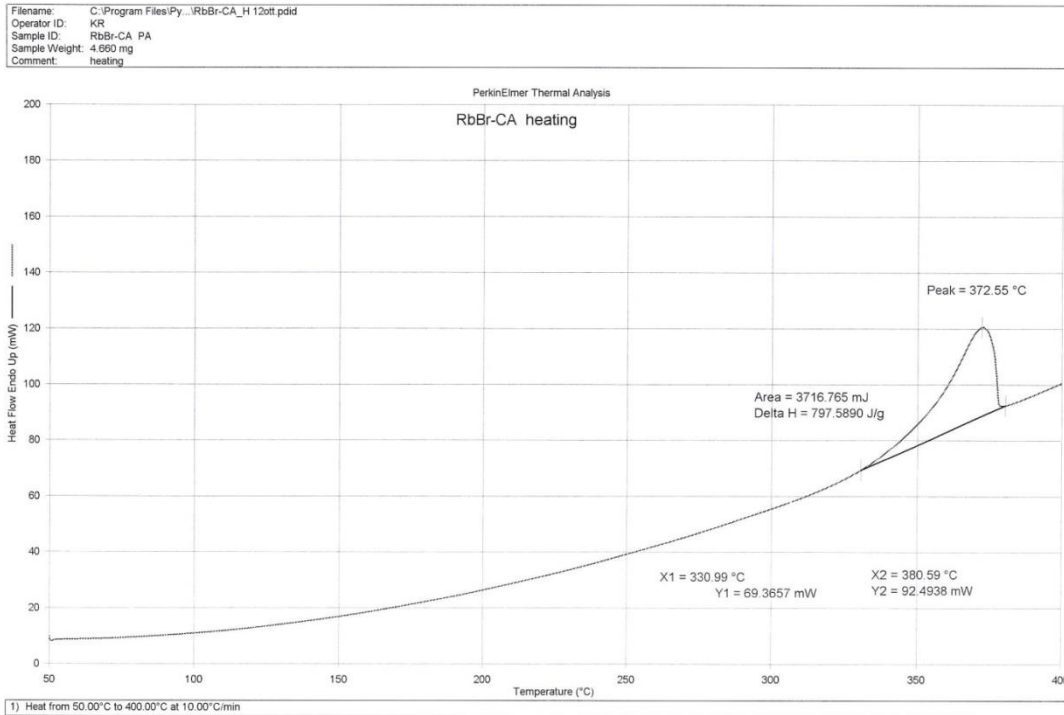


Figure 3.2.314 DSC trace for CA·RbBr.

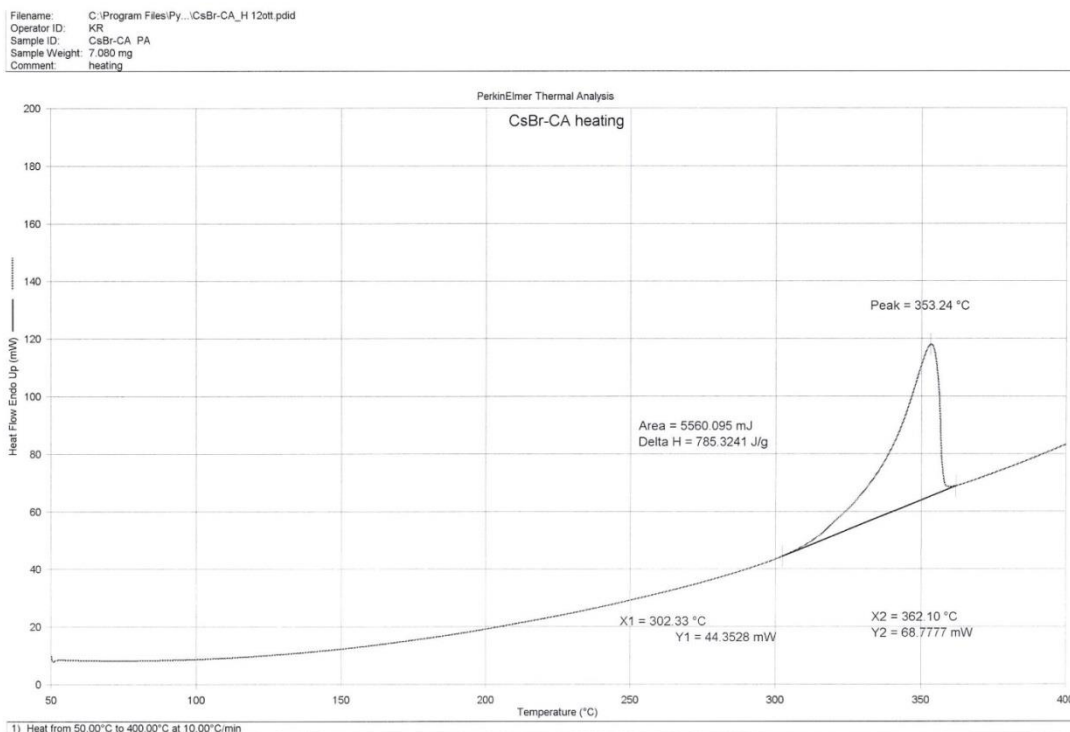


Figure 3.2.3-17 DSC trace for CA·CsBr.

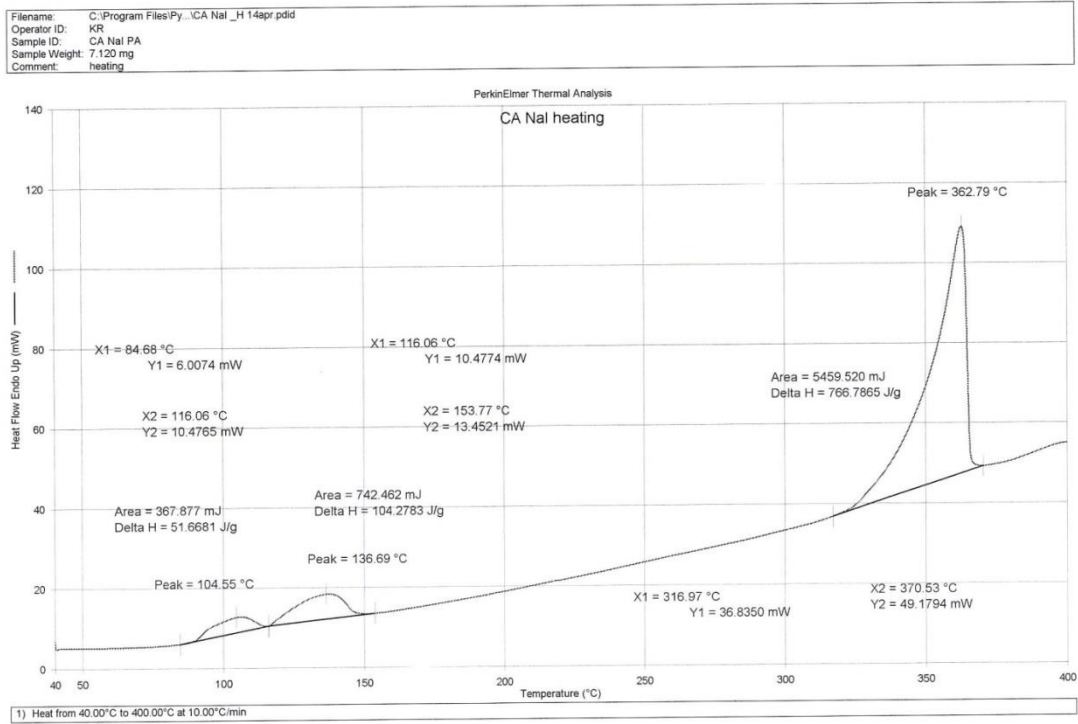


Figure 3.2.3-18 DSC trace for CA·Nal.

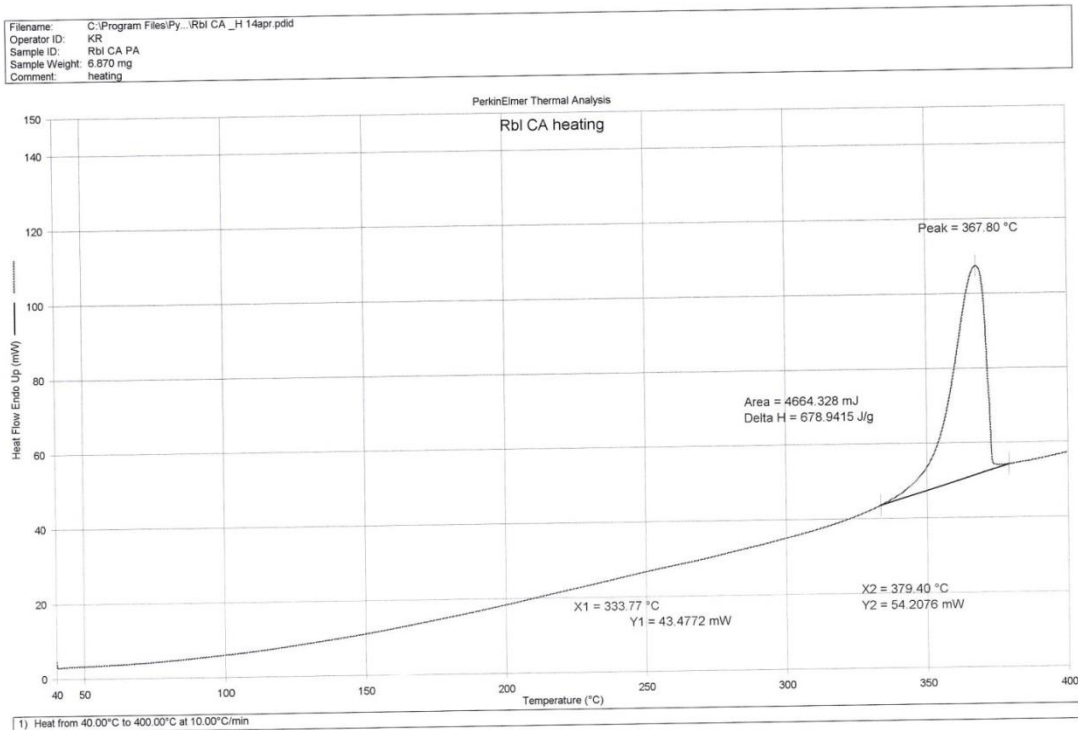


Figure 3.2.3-19 DSC trace for CA·Nal.

Filename: C:\Documents and Sett...RbCl-CA 10att.pdid
 Operator ID: KR
 Sample ID: RbCl-CA N2
 Sample Weight: 9.347 mg
 Comment:

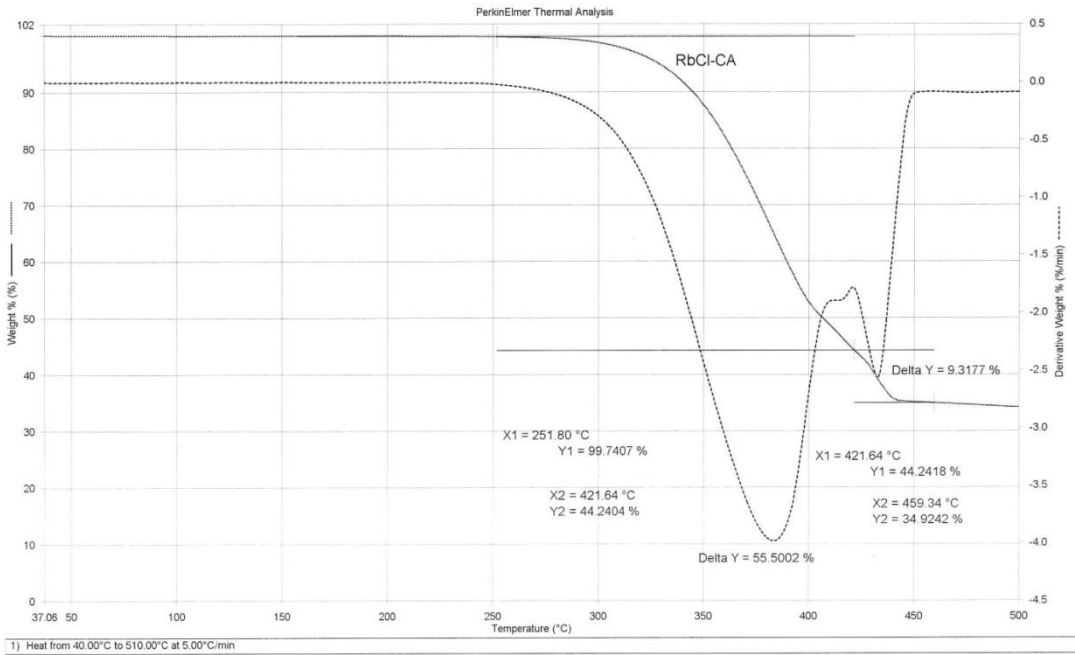


Figure 3.2.3-15 TGA trace for $CA_2 \cdot RbCl$.

Filename: C:\Documents and Sett...CsCl-CA 20att.pdid
 Operator ID: KR
 Sample ID: CsCl-CA N2
 Sample Weight: 9.002 mg
 Comment:

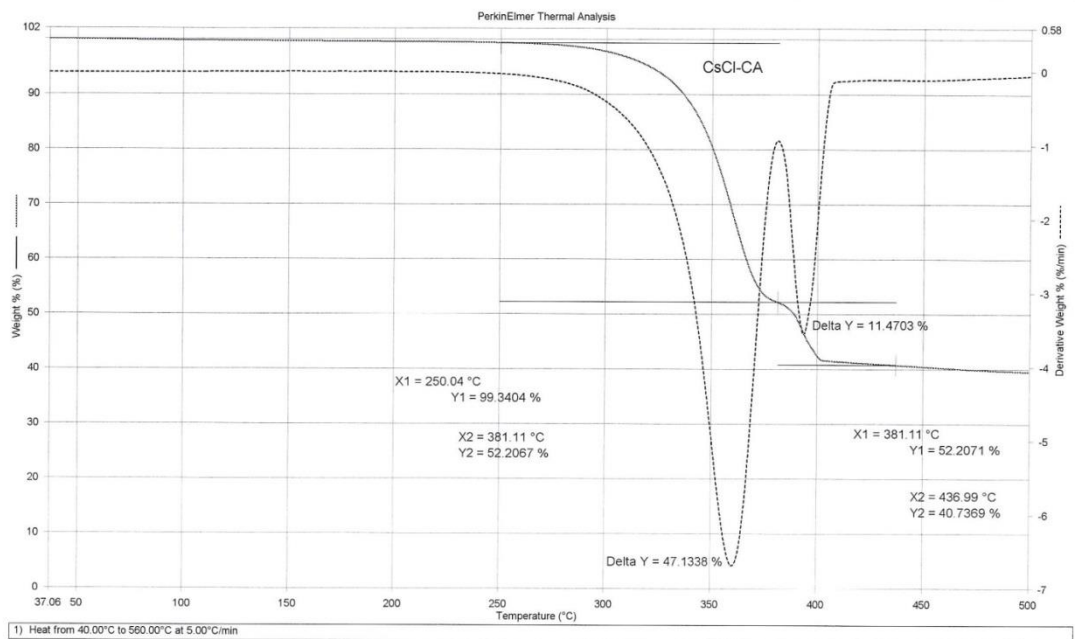


Figure 3.2.3-16 TGA trace for $CA_2 \cdot CsCl$.

Filename: C:\Documents and Settings\KR\NaBr-CA 2H2O 10ott.pdtd
 Operator ID: KR
 Sample ID: NaBr-CA 2H2O N2
 Sample Weight: 7.652 mg
 Comment:

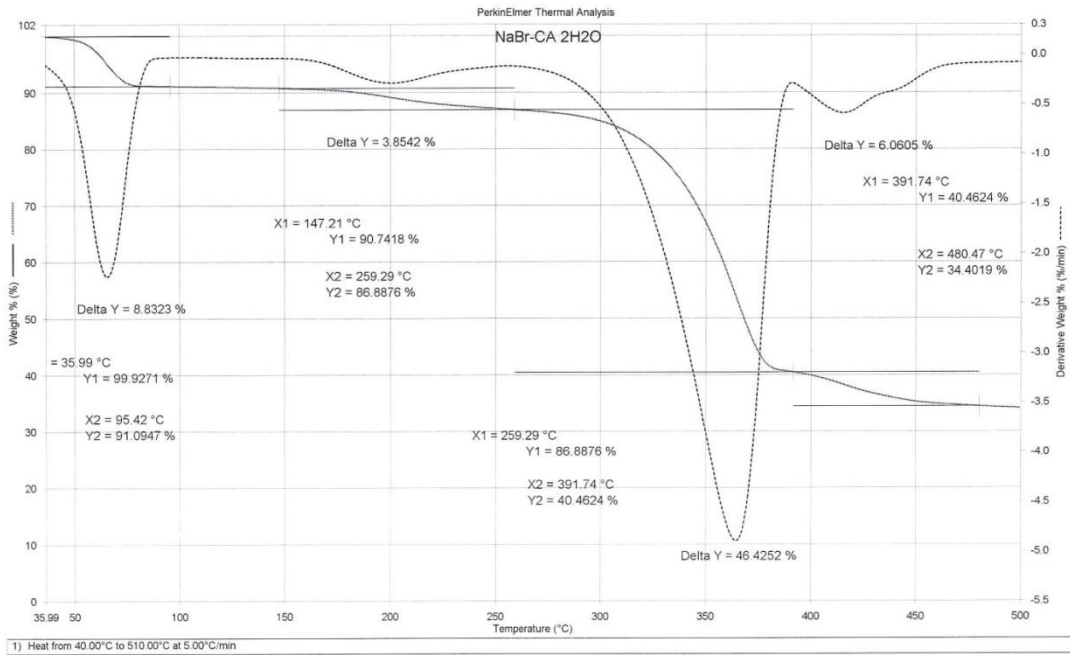


Figure 3.2.3-17 TGA trace for CA·NaBr·2H₂O.

Filename: C:\Documents and Settings\KR\NaBr-CA 20ott.pdtd
 Operator ID: KR
 Sample ID: NaBr-CA N2
 Sample Weight: 5.223 mg
 Comment:

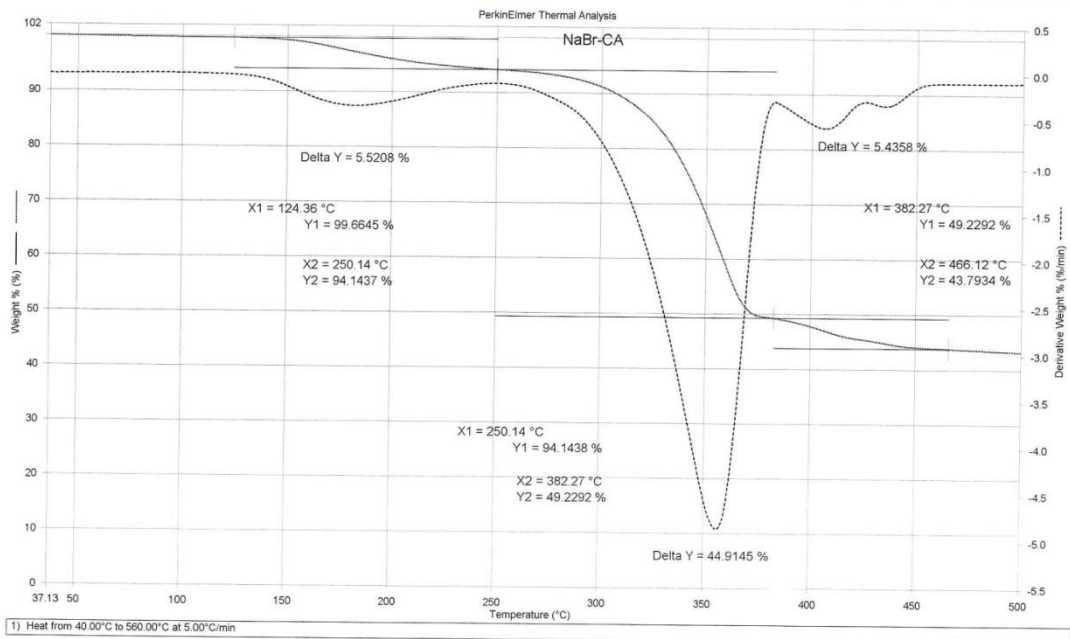


Figure 3.2.3-18 TGA trace for CA·NaBr.

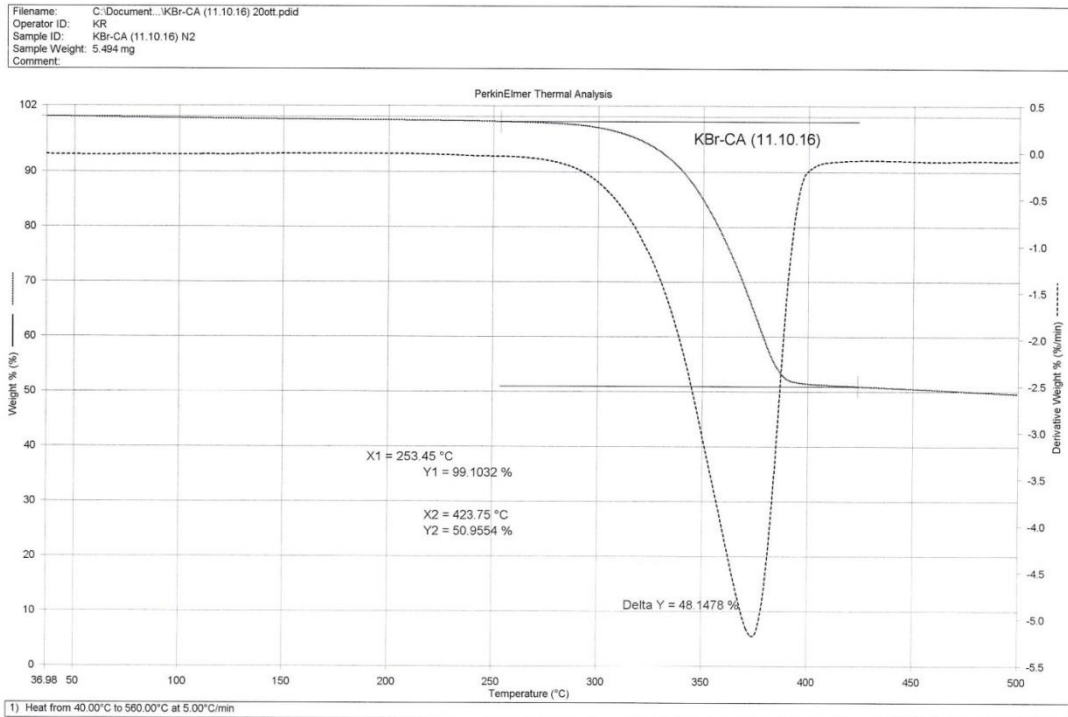


Figure 3.2.3-19 TGA trace for CA·KBr.

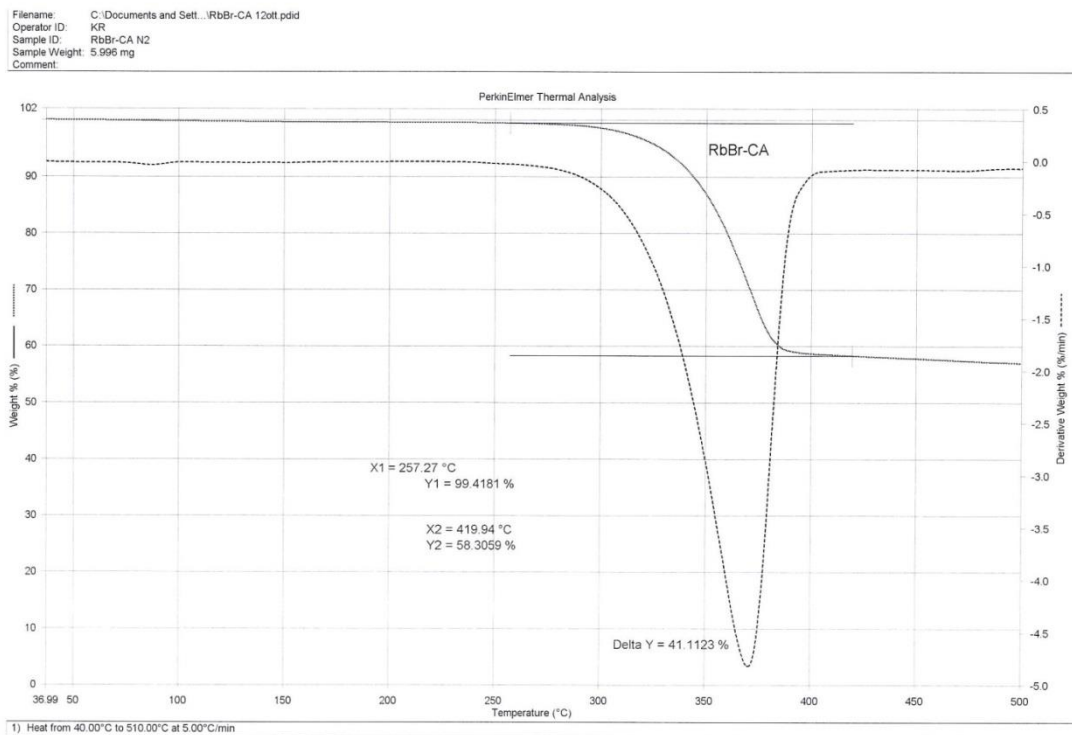


Figure 3.2.3-20 TGA trace for CA·RbBr.

Filename: C:\Documents and Sett...\CsBr-CA 12ott.ppid
Operator ID: KR
Sample ID: CsBr-CA N2
Sample Weight: 5.608 mg
Comment:

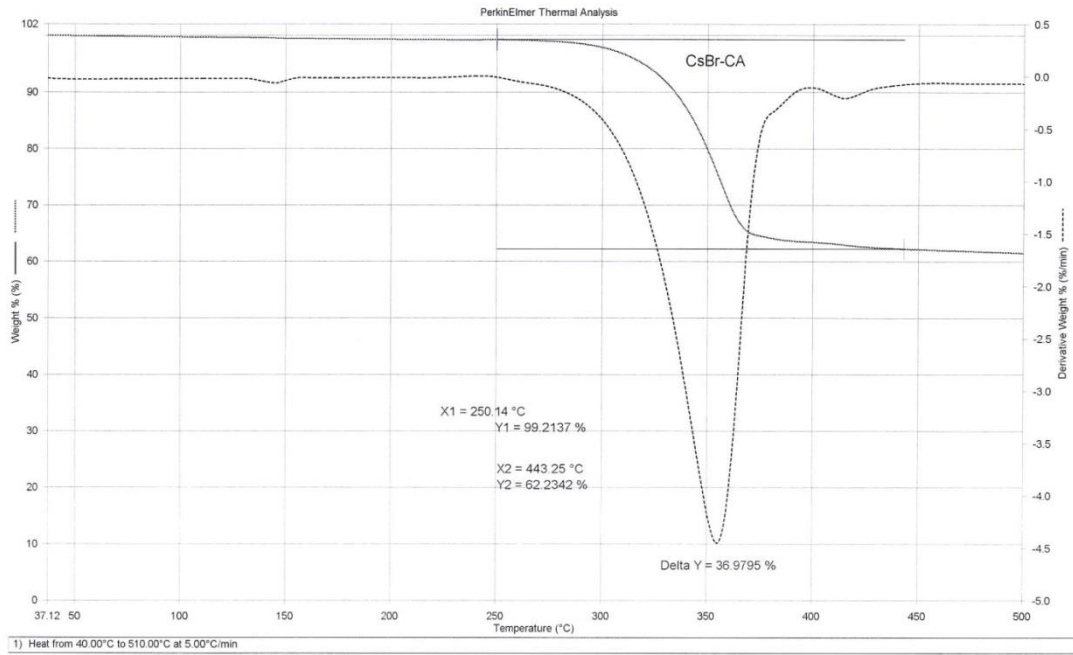


Figure 3.2.3-21 TGA trace for CA·CsBr.

Filename: C:\Documents and Settings...I CA 50tt.ppid
Operator ID: KR
Sample ID: I CA N2
Sample Weight: 6.010 mg
Comment:

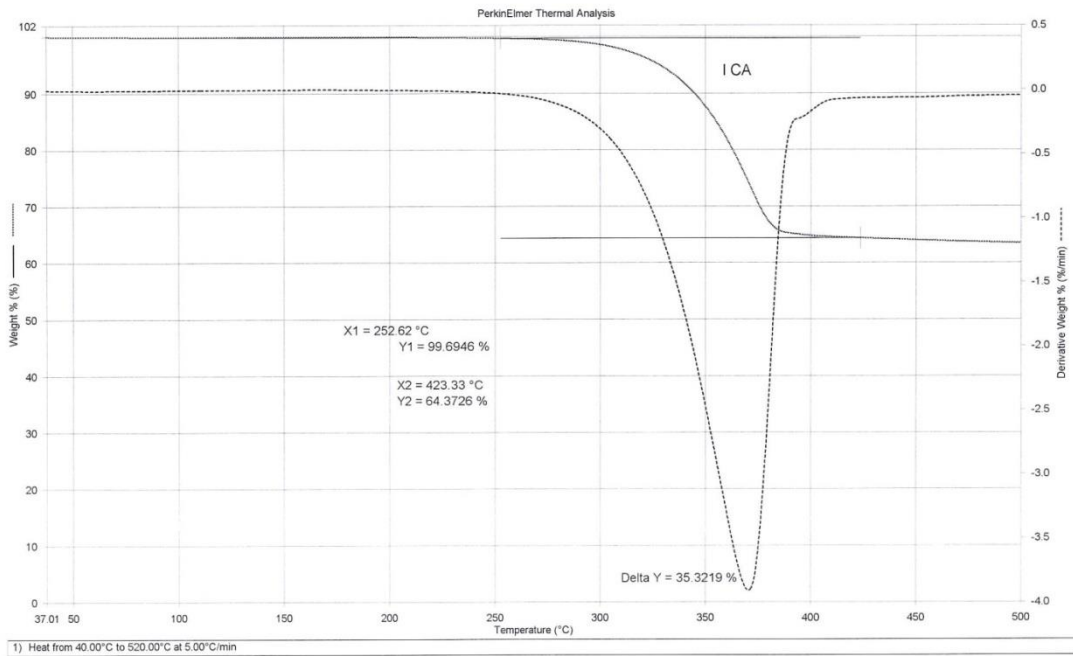


Figure 3.2.3-22 TGA trace for CA·Rbl.

3.2.4. Conclusions

The interaction of cyanuric acid with alkali halides resulted into formation of fourteen new ionic co-crystals. The ICCs were obtained mechanochemically – by grinding in the presence of a minimal quantity of a solvent. Such a synthetic technique represents a green chemistry approach. The structures of eleven of them were determined: ten were solved from XRPD patterns and one using single crystal data. The peculiarities of the crystal packing of ICCs depending on the nature of the ions were demonstrated. The solubility properties of CA·NaCl were investigated. The co-crystal appeared to be much more soluble compared to CA on its own.

3.3. Mechanochemical preparation of molecular and ionic co-crystals of the hormone melatonin

3.3.1. Overview

The search for new possible formulations of natural antioxidants and geroprotectors L-carnosine and melatonin aimed at optimizing physicochemical properties has become the main scope of my Master thesis.³⁷ L-carnosine was co-crystallized with a number of organic acids which belong to the GRAS³⁸ (Generally Recognized As Safe) list.³⁹ Melatonin, in turn, was co-crystallized with a number of molecular co-formers, but only two molecular co-crystals were obtained.³⁷ Consequently, we decided to try and obtain ionic co-crystals upon co-crystallizing melatonin with pharmaceutically acceptable inorganic salts, namely NaCl, ZnCl₂, CaCl₂ and MgCl₂. Melatonin is barely soluble in water and the idea was to test the possibility to enhance its solubility characteristics via co-crystallization with highly water soluble inorganic salts. However, only one ionic co-crystal Mel₂·CaCl₂·2H₂O was obtained. It was structurally characterized using thermogravimetric and XRPD data. The solubility study showed significant improvement of solubility characteristics of the co-crystal compared to those of melatonin itself.

3.3.2. Introduction

Pharmaceutical co-crystals^{4, 40-43} are multicomponent crystalline materials composed of an Active Pharmaceutical Ingredient (API) and at least one co-former, i.e. a benign molecule combined with the API in a specific stoichiometric ratio. To completely fulfil the requirements of co-crystals, both the API and the co-former(s) must be solid at ambient conditions.⁴⁴

Pharmaceutical co-crystals have been attracting scientists as they can not only considerably diversify the solid forms of APIs, but also improve their physicochemical properties (solubility,⁴⁵ dissolution rate,^{46, 47} bioavailability,⁴⁸ melting point,⁴⁹ *etc.*). The wide range of possible co-formers provides numerous strategies to manipulate the physicochemical properties of interest. More recently the choice of co-formers has been amply expanded by the use of pharmaceutically acceptable inorganic salts, e.g. some alkali and alkaline earth halides, in the co-crystal formation. These so called ionic co-crystals (ICCs)^{1, 2} provide alternative routes to modify the solid state properties of the API.^{9, 11} Recently this type of co-crystals has been proven to be useful in the context of chiral resolution.⁵⁰⁻⁵² In this paper we report the results of the investigation of the co-crystal landscape of the hormone melatonin.⁵³

Melatonin has been the subject of intense investigations, as witnessed by the number of scientific publications in the period 1985-2018 containing the word “melatonin” in their titles: 17 398 (of which more than 600 this year; source: Web of ScienceTM). A review article on the impact of melatonin in research has recently been published.⁵⁴ To date, only one co-crystal of melatonin with pimelic acid was reported.⁵⁵ This co-crystal showed a twofold increase in solubility characteristics and a 30% increase in the intrinsic dissolution rate compared to those of melatonin.

Melatonin (N-acetyl-5-methoxy-tryptaminem, Fig. 3.3.2-1) is the pineal hormone produced from the essential amino acid tryptophan mainly during the night.⁵⁶ It plays a vital role in the regulation of circadian and seasonal changes in various aspects of physiology and neuroendocrine function. In other words, it is responsible for the body internal timekeeping system and for the regulation of the sleep-wake cycle and seasonal adaptation. In addition to its

main functions, melatonin is also a powerful free-radical scavenger and wide-spectrum antioxidant.^{53, 56, 57}

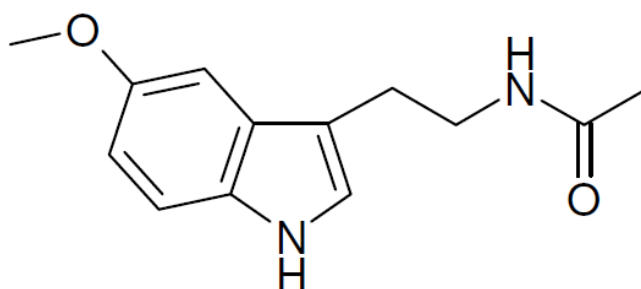


Figure 3.3.2-1 Melatonin.

Melatonin plays an essential role in human healthy life and the shortage of this antioxidant may result into oxidative damage of DNA, lipids and proteins: potential risks are accelerated senescence and development of ageing-related diseases (e.g. coronary heart disease, cerebrovascular disease, cancer, arthritis, dementia, cataract, osteoporosis, type II diabetes, hypertension, Alzheimer's disease, Parkinson's disease, etc.).^{57, 58}

Therefore, the increasing interest in the consumption of exogenous melatonin is not surprising. Generally, it is used to treat insomnia, jet lag, shift work disorder, circadian rhythm disorders in blind individuals, and benzodiazepine and nicotine withdrawal.⁵⁹ According to the US Food and Drug Administration (FDA) melatonin is a dietary supplement.⁶⁰ Its solubility in water is low;^{61, 62} this fact can limit its oral bioavailability in humans and, consequently, solubility enhancement would be highly desirable. To this end, we have explored co-crystal formation with a large number of potential co-formers.

We have succeeded with the cyclic diamines piperazine (PIP) and 1,4-diazabicyclooctane (DABCO) while CaCl_2 was successful in yield a di-hydrated ICC. The co-crystallization of melatonin with CaCl_2 is of particular interest since the organic salt belongs to the GRAS list.³⁸ The preparation, isolation, structural

features and solubility profiles will be discussed in the following. The structures of **the** products $\text{mel}_2\cdot\text{PIP}$ and $\text{mel}_2\cdot\text{CaCl}_2\cdot 2\text{H}_2\text{O}$ were determined directly from powder diffraction data, while crystals suitable for single-crystal experiments were obtained for $\text{mel}_2\cdot\text{DABCO}$.

3.3.3. Experimental part

Materials and instrumentation

All reagents and solvents used in this work were purchased from Sigma-Aldrich and used without further purification.

Solid State Synthesis

Co-crystals of melatonin with DABCO, $\text{mel}_2\cdot\text{DABCO}$, and piperazine, $\text{mel}_2\cdot\text{pip}$, and the hydrated ionic co-crystal with CaCl_2 , $\text{mel}_2\cdot\text{CaCl}_2\cdot 2\text{H}_2\text{O}$, were obtained by mechanochemistry: Melatonin (0.1 mmol) and the corresponding co-former (0.05 mmol) were kneaded for 30 minutes in a Retsch MM400 ball miller, operated at a frequency of 20 Hz, in the presence of a few drops of ethanol. $\text{Mel}_2\cdot\text{DABCO}$ crystals suitable for single crystal X-ray diffraction analysis were obtained by slow evaporation of a dichloromethane saturated solution of the kneading product.

Slurry

$\text{Mel}_2\cdot\text{CaCl}_2\cdot 2\text{H}_2\text{O}$ was also obtained by slurring equimolar amounts of melatonin and $\text{CaCl}_2\cdot 6\text{H}_2\text{O}$ in ethanol for two days.

X-ray powder diffraction measurements

Room temperature X-ray powder diffraction (XRPD) patterns were collected on two different diffractometers: on a Bruker D2 phaser X-ray diffractometer in the 2θ range from 3° to 37° using a $\text{Cu-K}\alpha$ ($\lambda=1.54 \text{ \AA}$) source equipped with a LinxEye detector, nickel filter and operated at 30 kV and 10 mA and on a

PANalytical X'Pert PRO automated diffractometer equipped with a X'Celerator detector in the 2θ range $3\text{--}50^\circ$ (step size 0.011, time/step 50 s, VxA 40x40). Data analyses were carried out using the PANalytical X'Pert Highscore Plus program. The identity between the bulk material obtained via solution and solid-state processes was always verified by comparing calculated and observed powder diffraction patterns (see SI fig. 3.3.5-9-10).

Structural Characterization from powder data

Powder diffraction data were analysed with the software X'Pert HighScore Plus. 15 peaks were chosen in the 2θ range 3-37, and unit cell parameters were found using DICVOL4⁶³ or DICVOL6⁶³ algorithms. The procedure for the structure solution of $\text{mel}_2\cdot\text{CaCl}_2\cdot 2\text{H}_2\text{O}$ is described here. This ICC is characterized by a monoclinic unit cell with a volume of $1501.51(1) \text{ \AA}^3$, compatible with the presence of four molecules of melatonin, two Ca^{2+} , four Cl^- anions and four water molecules. The structure was solved in the space group $P2_1/c$ by simulated annealing, performed with EXPO2014³⁰ using one melatonin, one chloride, water and calcium moieties (the latter was found to be on a special position). Ten runs for simulated annealing trial were set, and a cooling rate (defined as the ratio T_n/T_{n-1}) of 0.95 was used. The best solutions were selected and used for Rietveld refinements, which was performed with the software TOPAS³². An overall thermal parameter was adopted for all atoms of melatonin. All hydrogen atoms were fixed in calculated positions. Structural data for all compounds investigated in this work are listed in Table 3.3.3-1.

Table 3.3.3-1 Structural data for melatonin co-crystals and ionic co-crystals.

	$\text{mel}_2\cdot\text{pip}$	$\text{mel}_2\cdot\text{DABCO}$	$\text{mel}_2\cdot\text{CaCl}_2\cdot 2\text{H}_2\text{O}$
Formula	$\text{C}_{30}\text{H}_{42}\text{N}_6\text{O}_4$	$\text{C}_{32}\text{H}_{44}\text{N}_6\text{O}_4$	$\text{C}_{26}\text{H}_{36}\text{N}_4\text{O}_6\text{CaCl}_2$
Fw ($\text{g}\cdot\text{mol}^{-1}$)	550.69	576.73	611.57

Crystal system	Monoclinic	Monoclinic	Monoclinic
Space group	P2 ₁ /c	P2 ₁ /c	P2 ₁ /c
Z, Z'	2, 0.5	2, 0.5	2, 0.5
a (Å)	17.051(6)	17.685(4)	18.965(4)
b (Å)	9.831(3)	9.925(2)	8.9353(14)
c (Å)	9.334(3)	9.2960(19)	8.9870(18)
α (°)	90.0	90.0	90.0
β (°)	105.099(17)	103.39(3)	99.634(17)
γ (°)	90.0	90.0	90.0
V (Å ³)	1510.61(8)	1587.3 (6)	1501.50(5)
R _{wp}	4.24	-	4.83
d / mg.cm ⁻³	-	1.207	-
μ / mm ⁻¹	-	0.081	-
Measd reflns	-	22619	-
Indep reflns	-	3453	-
Reflns ($I \geq 2\sigma(I)$)	-	2689	-
R _{int}	-	0.034	-
R[F ² > 2σ(F ²)]	-	0.09	-
wR(F ²)	-	0.171	-

Single Crystal X-ray Diffraction

Single crystal X-ray data for mel₂·DABCO were collected at RT and at 150K on a Bruker D8 and an X8 Apex II diffractometers, respectively, both equipped with MoKα X-ray source and graphite monochromator. Multi-scan absorption correction (SADABS) was applied. Data collection and refinement details are listed in Table 1. All non-hydrogen atoms were refined anisotropically. The DABCO molecule in mel₂·DABCO is disordered around a crystallographic inversion centre. H_{CH} and H_{NH} atoms were added in calculated positions and refined riding on their respective carbon atoms. The structure was solved by the Intrinsic Phasing methods and refined by least squares methods again F² using SHELXT-2014⁶⁴ and SHELXL-2014⁶⁵. The program Platon⁶⁶ was used to calculate hydrogen bond

distances. Schakal³⁵ and Mercury 3.10³⁶ were used for molecular graphics.

Differential Scanning Calorimetry (DSC)

DSC measurements were performed for melatonin and its co-crystals with a Perkin–Elmer Diamond. Samples (3–5 mg) were placed in hermetic aluminium pans. Heating was carried out at 5 °C min⁻¹ for all samples.

Thermogravimetric Analysis (TGA)

TGA measurements of melatonin and its co-crystals were performed using a Perkin-Elmer TGA7 in the temperature range 30-400 °C under an N₂ gas flow, at a heating rate of 5 °C min⁻¹.

Solubility test for mel₂·CaCl₂·2H₂O.

A small amount of mel₂·CaCl₂·2H₂O was weighed and portions of it were added to a test tube containing 1mL of water at room temperature and shaken until the solid was completely dissolved. The procedure was repeated until no more mel₂·CaCl₂·2H₂O could be dissolved. The remaining co-crystal was weighed and the difference with the initial quantity calculated as the amount of the co-crystal dissolved. The experiment was repeated 3 times and the average value was used.

3.3.4. Results and Discussion

Co-crystals of melatonin with piperazine and DABCO

Despite the wide interest in melatonin, only one example of melatonin co-crystal, melatonin·pimelic acid, has recently been reported in the literature.⁵⁵ Co-crystallization of melatonin was attempted with a number of co-formers, containing different functional groups (see Table SI 3.3.5-

1-4), by applying a variety of methods such crystallization from solution, grinding, kneading and slurry, all in various stoichiometric ratios. In no instance co-crystallization with melatonin was observed, and the products invariably resulted in a mixture of the starting materials. Successful results were obtained only when we used diamine bases as co-formers; in this way the base can act as a hydrogen bonding bridge between two melatonin molecules, thus disrupting the dimer present in pure melatonin, which is further stabilized by four hydrogen bonding interactions with amido oxygen of four neighbouring melatonin molecules (see Fig. 3.34-1).

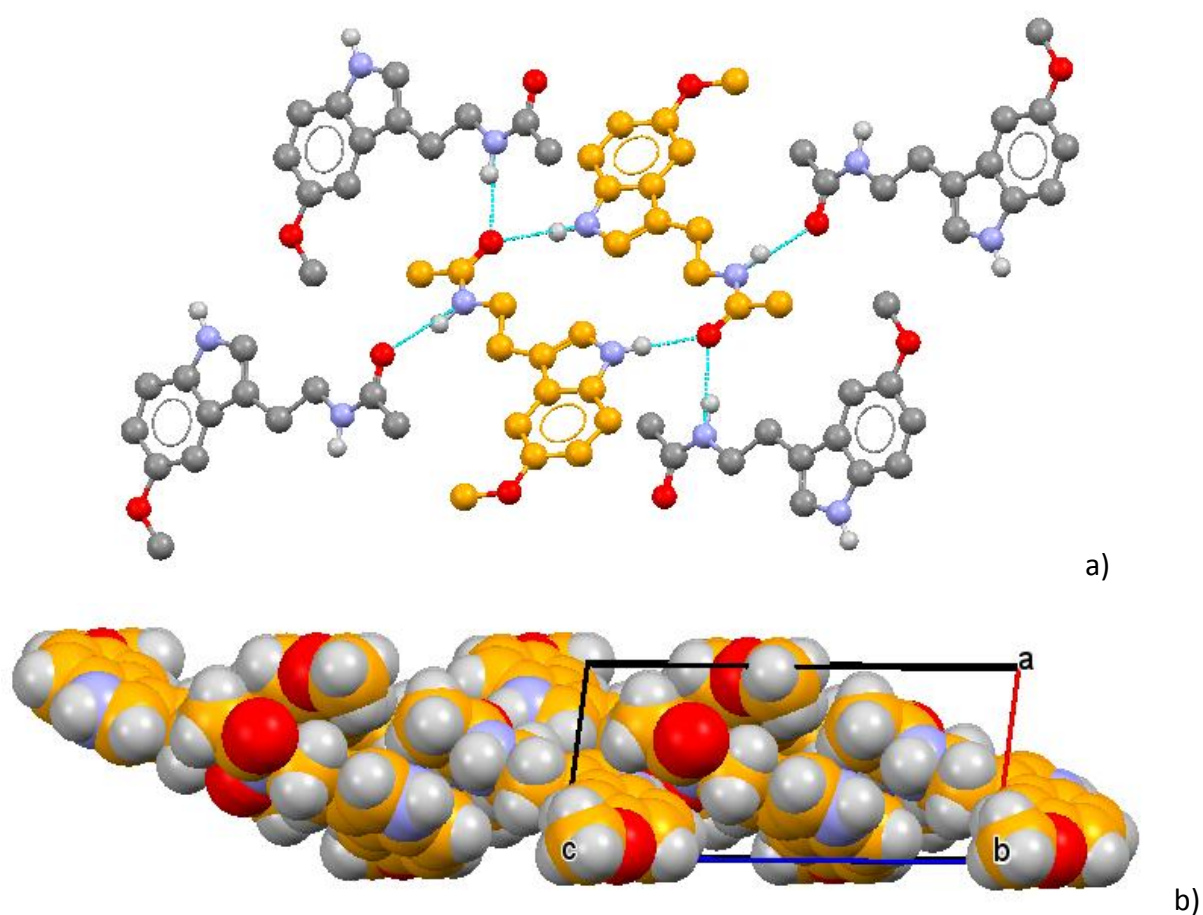


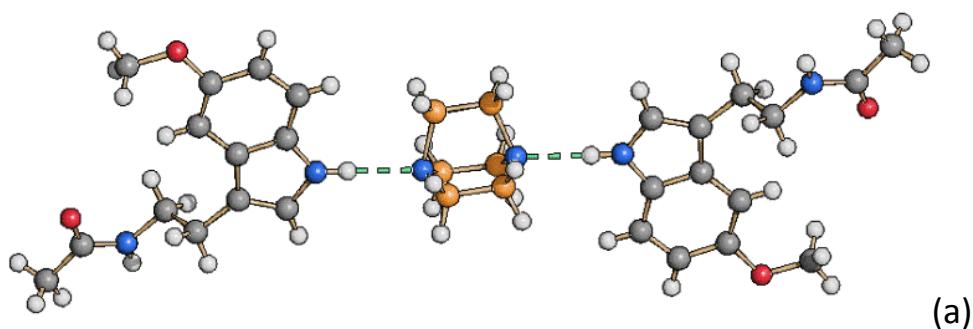
Figure 3.3.4-1 HB-pattern in crystalline melatonin (MELATN01).

The main packing motif is the hydrogen bonded “dimer” formed by two melatonin molecules referred by an inversion centre (C atoms in orange) (a). The dimer is then interacting via further hydrogen bonds with four melatonin molecules, thus forming a thick, infinite 2D-layer (b) extending in the *bc*-plane.

The diamine bases piperazine and DABCO (1,4-diazabicyclooctane) were selected to react with melatonin; DABCO does not belong to the GRAS family, but was chosen because of its similarity, both in shape and functions, with piperazine. We were able to obtain the two co-crystals $\text{mel}_2\cdot\text{DABCO}$ and $\text{mel}_2\cdot\text{pip}$ by ball-milling melatonin with DABCO or piperazine in a 2:1 ratio, in the presence of a drop of ethanol. In the case of DABCO single crystals were obtained from solution reaction in dichloromethane, and full structural characterization of $\text{mel}_2\cdot\text{DABCO}$ was possible via single crystal X-ray diffraction.

Fig. 3.3.4-1a shows how the $\text{N-H}\cdots\text{O}_{\text{amido}}$ hydrogen bonds present in the pure melatonin dimer are replaced in $\text{mel}_2\cdot\text{DABCO}$ by $\text{N}_{\text{base}}\cdots(\text{H})\text{N}_{\text{melatonin}}$ hydrogen bonds.

Attempts at obtaining single crystals of $\text{mel}_2\cdot\text{pip}$, following the same procedure, were unsuccessful. Given the strong similarity of their X-ray powder patterns (see Fig. SI 3.3.5-12), and the similarity in shape and hydrogen bonding propensity of piperazine and DABCO, we assumed that the two co-crystalline materials were isomorphous; the structure of $\text{mel}_2\cdot\text{pip}$ was thus solved from powder data (see Fig. 3.3.4-2b), using as a model the structure of $\text{mel}_2\cdot\text{DABCO}$. The whole crystal in both $\text{mel}_2\cdot\text{DABCO}$ and $\text{mel}_2\cdot\text{pip}$ can be described as formed by alternating layers of melatonin and piperazine or DABCO molecules, as it is shown in Figure 3.3.4-2c for crystalline $\text{mel}_2\cdot\text{pip}$.



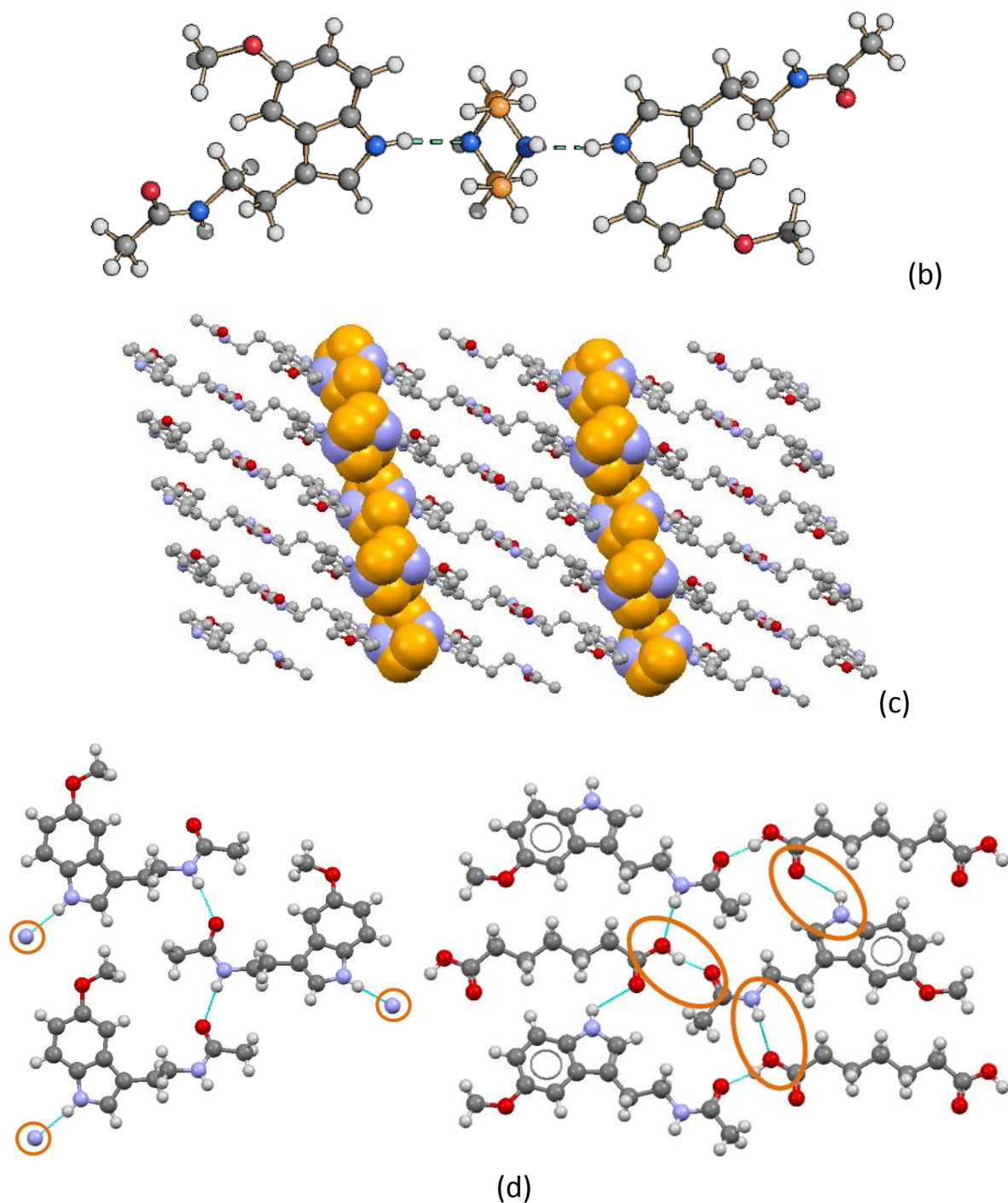


Figure 3.3.4-2 The DABCO (a) and piperazine (b) molecules bridge pairs of melatonin molecules via hydrogen bonds of the $N \cdots (H)N_{\text{melatonin}}$ type. The whole crystal can be described as alternating layers of melatonin and piperazine or DABCO molecules extending parallel to the b -axis, as it is shown here; (c) for crystalline $\text{mel}_2 \cdot \text{pip}$ (hydrogen atoms omitted for clarity). *Orange circles in (d) indicate DABCO nitrogen atoms.*

Hydrated ionic co-crystal of melatonin with CaCl_2

Ionic co-crystals (ICCs) are currently attracting the interest of scientists working with pharmaceutical compounds, as they make possible to build crystalline

materials comprising charged ions, i.e. Coulombic interactions, *and* unmodified, neutral APIs.² This is particularly relevant for systems that do not possess hydrogen bonding donors or acceptor to be used for the construction of molecular co-crystals. By reacting equimolar quantities of melatonin and $\text{CaCl}_2 \cdot 6\text{H}_2\text{O}$ in a slurry experiment with ethanol, we were able to obtain the dihydrated ionic co-crystal $\text{mel}_2 \cdot \text{CaCl}_2 \cdot 2\text{H}_2\text{O}$. Figure 3.3.4-3 shows the first coordination sphere of the calcium cation, which lies on a crystallographic inversion centre: two water molecules, two O_{amido} atoms belonging to melatonin and two chloride ions constitute the vertices of an octahedron; infinite layers of octahedra extend parallel to the crystallographic *bc*-plane (see fig. 3.3.4-4). Charge-assisted hydrogen bonding interactions of the $\text{N}(\text{H}) \cdots \text{Cl}^-$ type [$\text{N}(\text{H}) \cdots \text{Cl}^-$ 3.45(1) Å] are present between the chloride anions and the NH groups on melatonin. As a result, charged species and hydrogen bond acceptor groups are all “segregated” along the layers (fig. 3.3.4-4).

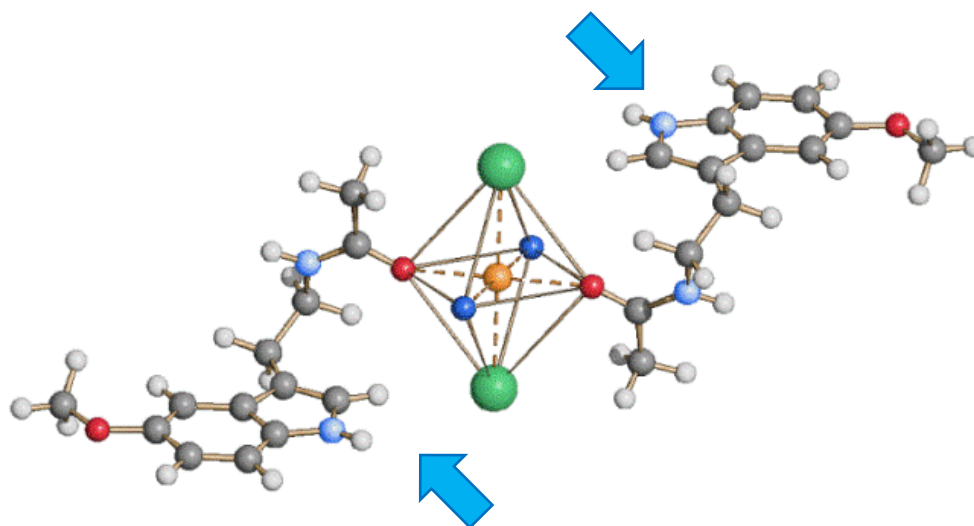


Figure 3.3.4-3 The coordination of melatonin, water molecules (blue) and chlorides to Ca^{2+} . The NH groups indicated by the arrow are hydrogen bonded to chloride ions belonging to the coordination sphere of adjacent Ca^{2+} ions.

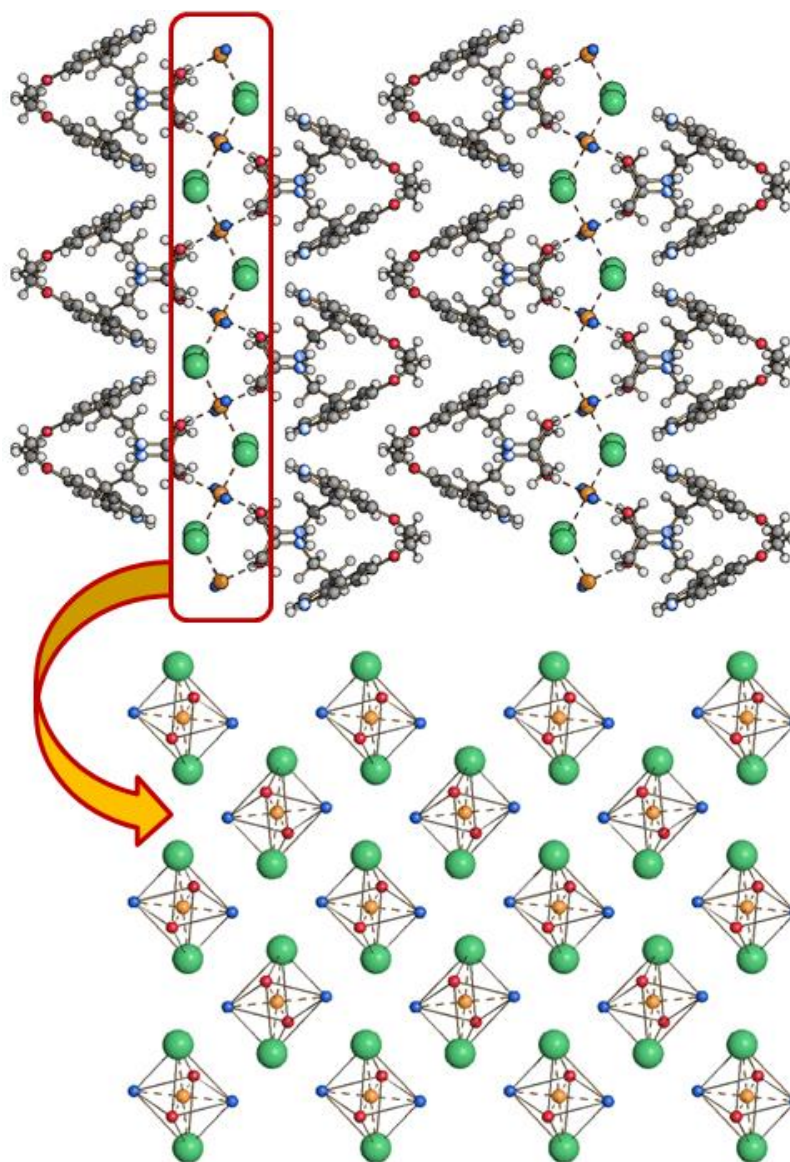


Figure 3.3.4-4 The crystal packing of $\text{mel}_2 \cdot \text{CaCl}_2 \cdot 2\text{H}_2\text{O}$. Top: view along the c -axis; bottom: layer, view along the a -axis.

In our recent paper it was shown that the co-crystallization of cyanuric acid with sodium chloride resulted in a significant improvement of solubility characteristics of the organic molecule.¹² Thus, in view of the interest in increasing the solubility of melatonin in water the thermodynamic solubility of $\text{mel}_2 \cdot \text{CaCl}_2 \cdot 2\text{H}_2\text{O}$ has been measured.

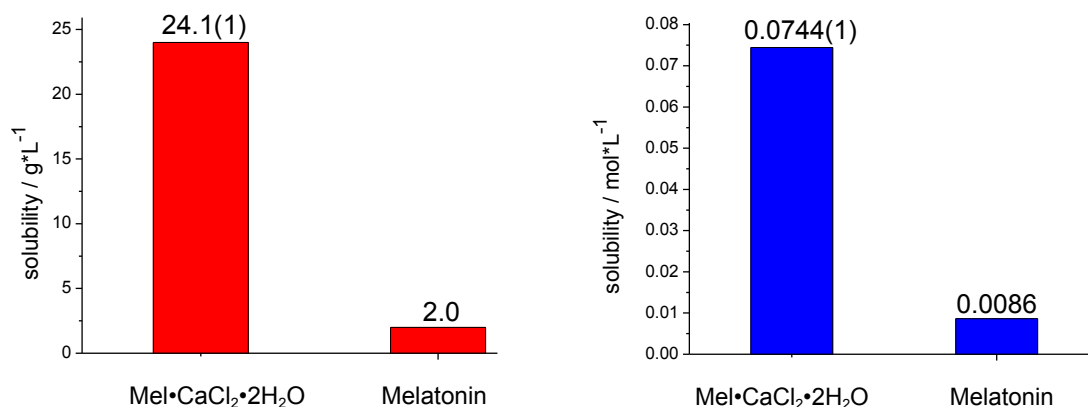


Figure 3.3.4-5 Comparison of the solubility in water at 293 K for melatonin⁶¹ and the ionic co-crystal mel₂•CaCl₂•2H₂O, in g*L⁻¹ (left) and in mol*L⁻¹ (right).

The thermodynamic solubility of mel₂•CaCl₂•2H₂O showed an impressive difference, with an increase of about 8.5 times with respect to the pure organic compound (0.0744(1) versus 0.0086 mol*L⁻¹) (fig. 3.3.4-5). In order to investigate the possibility of existence of the obtained ICC as an anhydrous product, variable temperature experiments have been performed. However, the only change one could observe was amorphization of the product at the temperature close to the melting point of melatonin.

3.3.5. Supporting information

Filename: C:\Documents and S...\Melatonina 18ott.pcid
 Operator ID: KR
 Sample ID: Melatonina N2
 Sample Weight: 2.106 mg
 Comment:

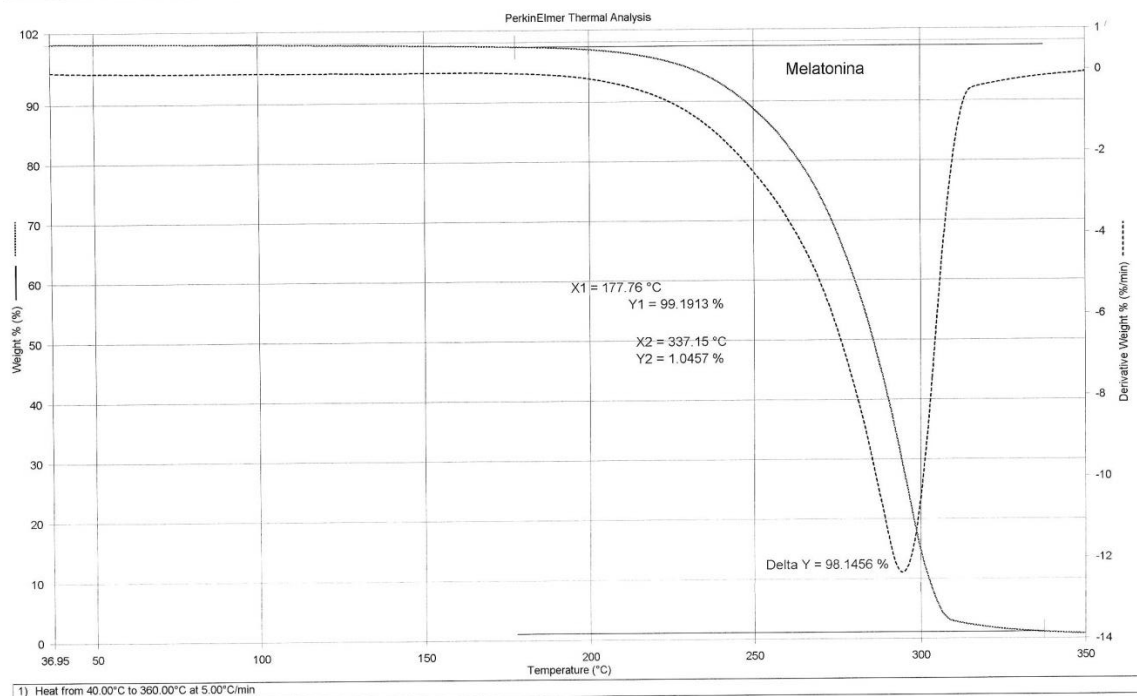


Figure 3.3.5-1 TGA of melatonin.

Filename: C:\Program Files...\Melatonina_H 18ott.pcid
 Operator ID: KR
 Sample ID: Melatonina pan aperto
 Sample Weight: 2.800 mg
 Comment: heating

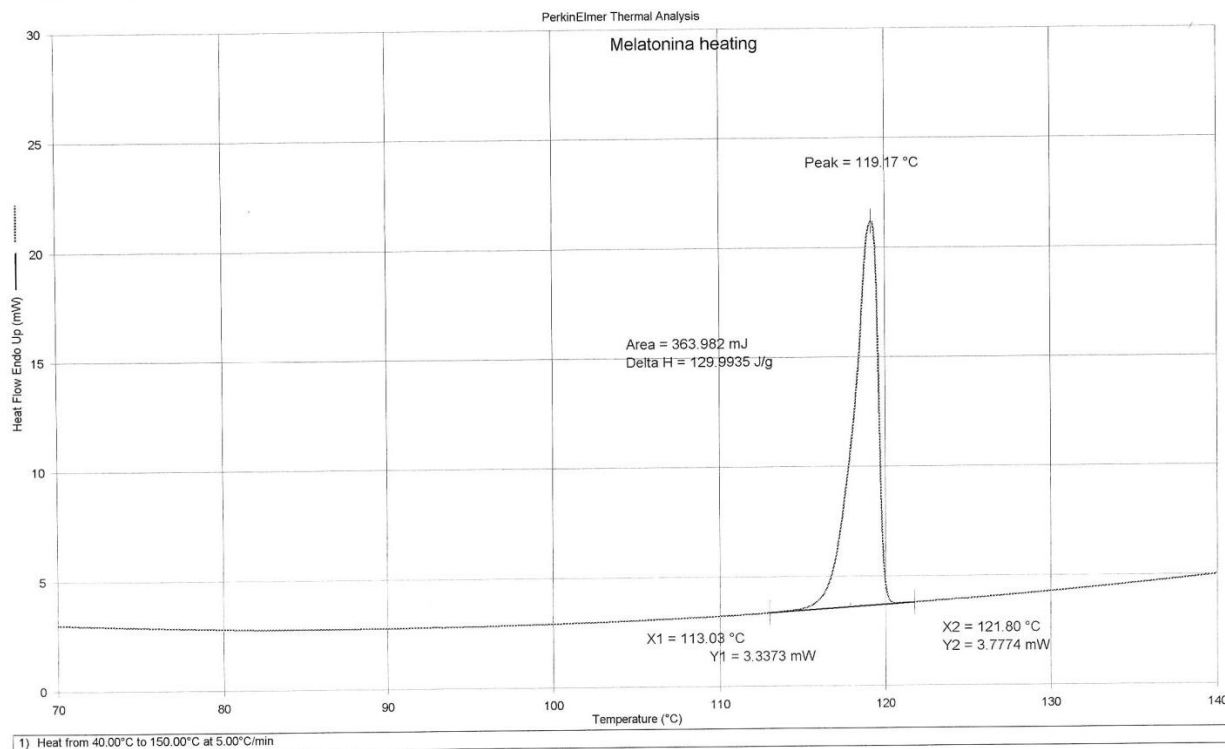


Figure 3.3.5-2 DSC of melatonin.

Filename: C:\Documents and Se...MEL DABCO 24mag.pdid
 Operator ID: KR
 Sample ID: MEL DABCO N2
 Sample Weight: 3.211 mg
 Comment:

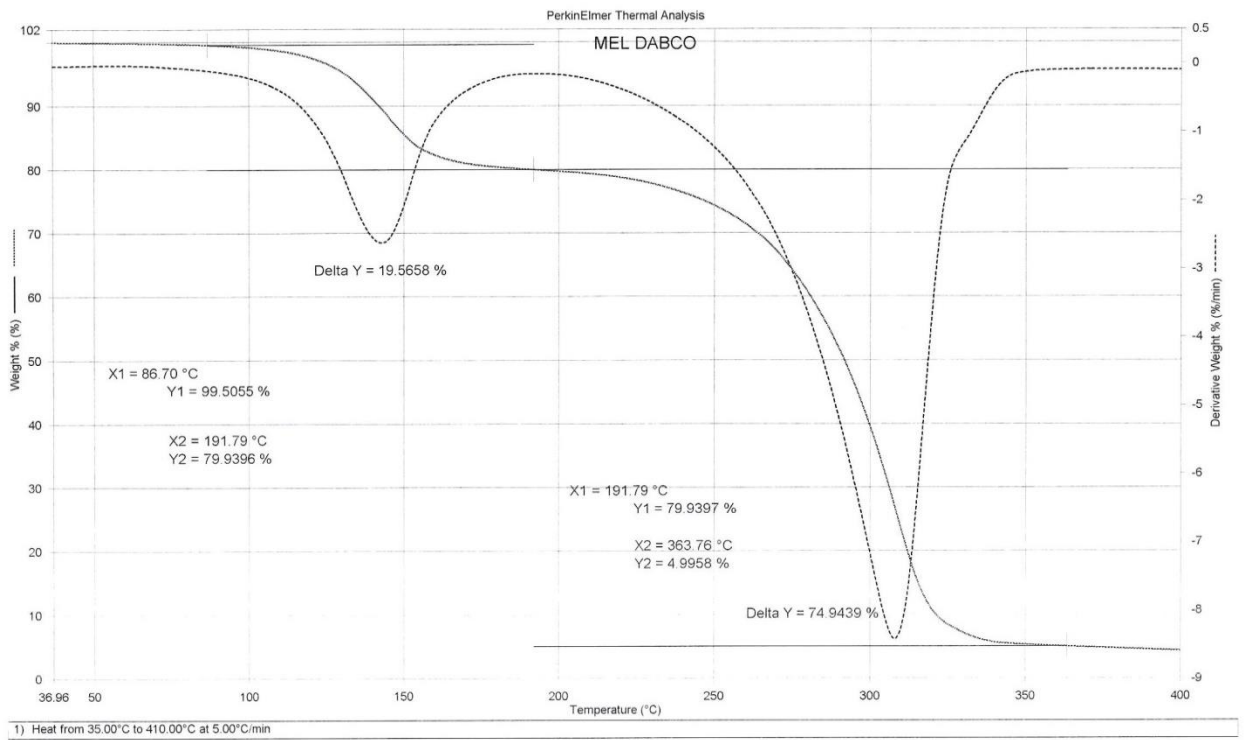


Figure 3.3.5-3 TGA of mel₂-DABCO.

Filename: C:\Program Fil...MEL DABCO_H PA 11mag.pdid
 Operator ID: KR
 Sample ID: MEL DABCO PA
 Sample Weight: 4.740 mg
 Comment: heating

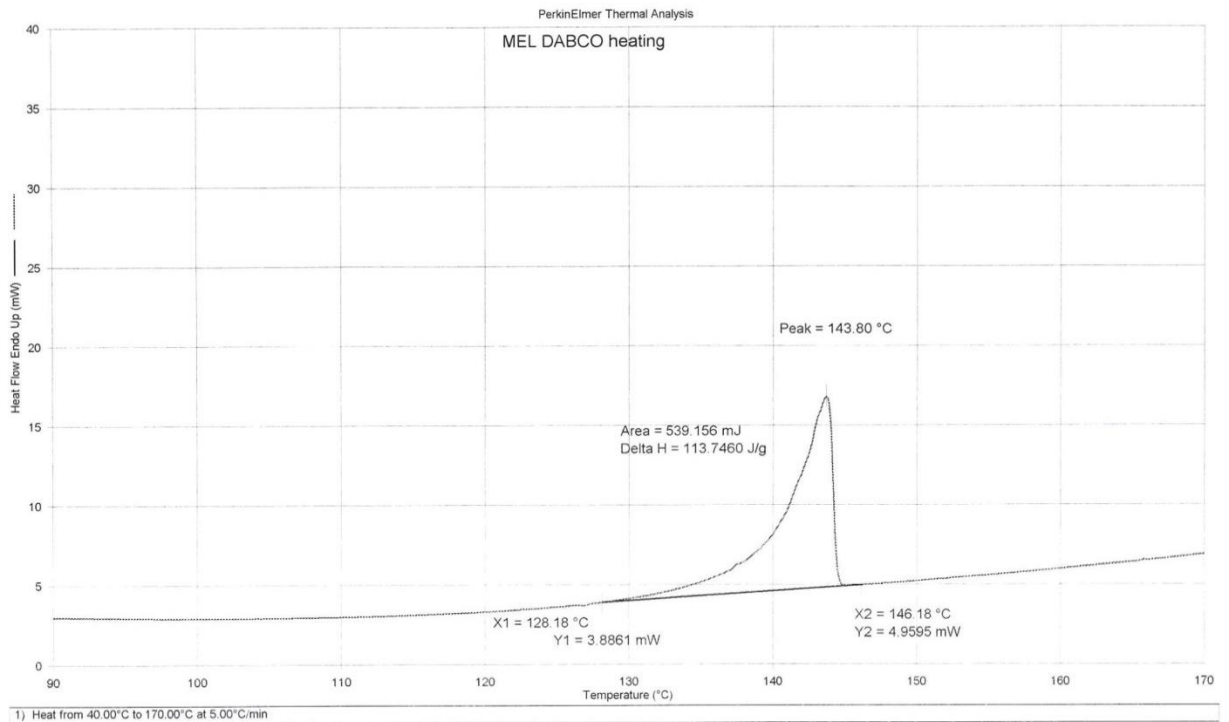


Figure 3.3.5-4 DSC of mel₂-DABCO.

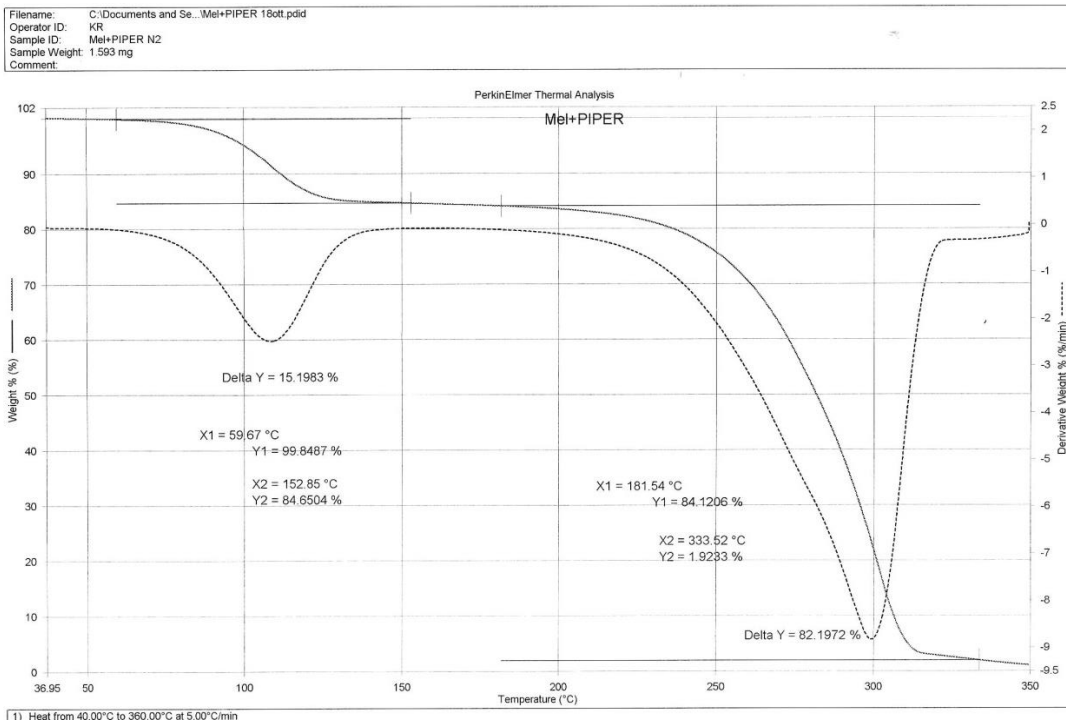


Figure 3.3.5-5 TGA of mel₂·pip.

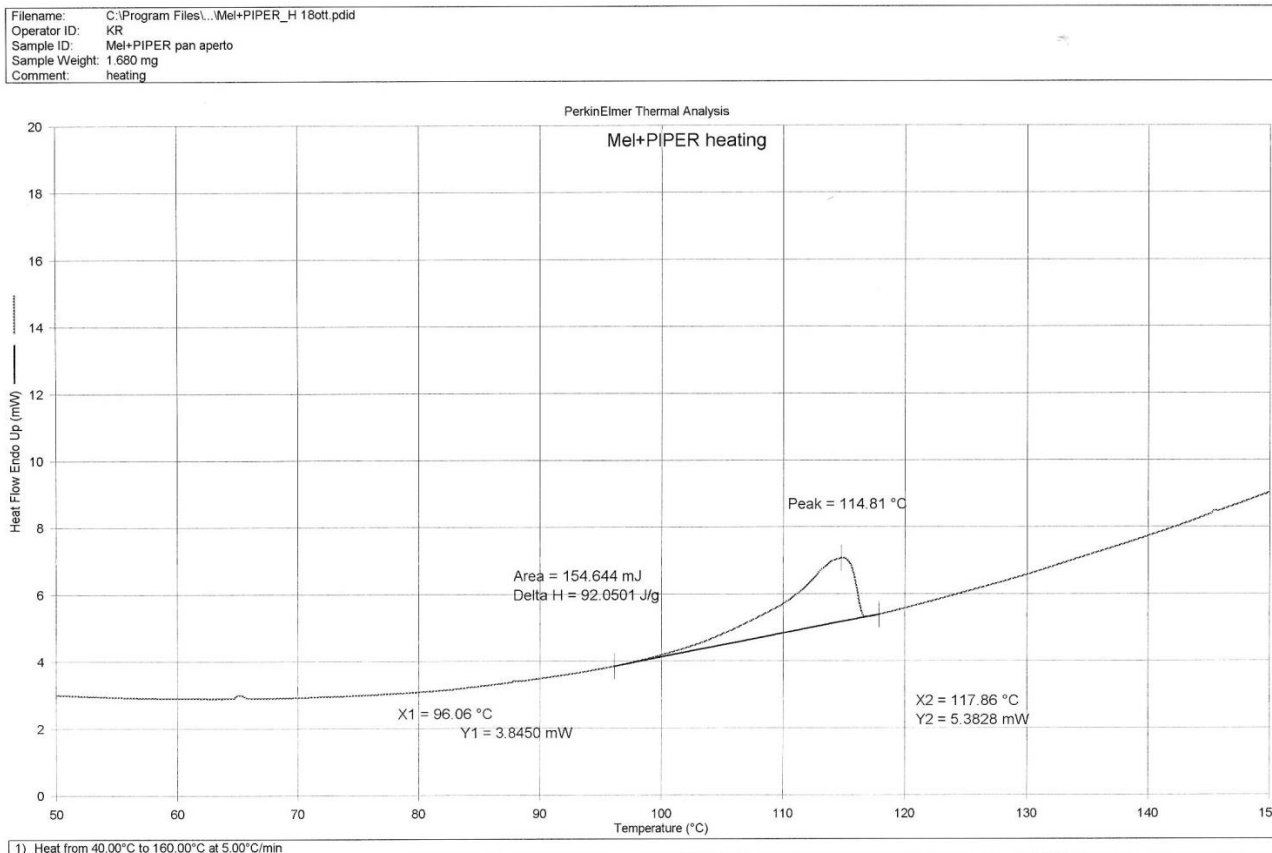


Figure 3.3.5-6 DSC of mel₂·pip.

Filename: C:\Documents...MEL2 CaCl2 2H2O 25mag.pdlid
 Operator ID: KR
 Sample ID: MEL2 CaCl2 2H2O N2
 Sample Weight: 3.736 mg
 Comment:

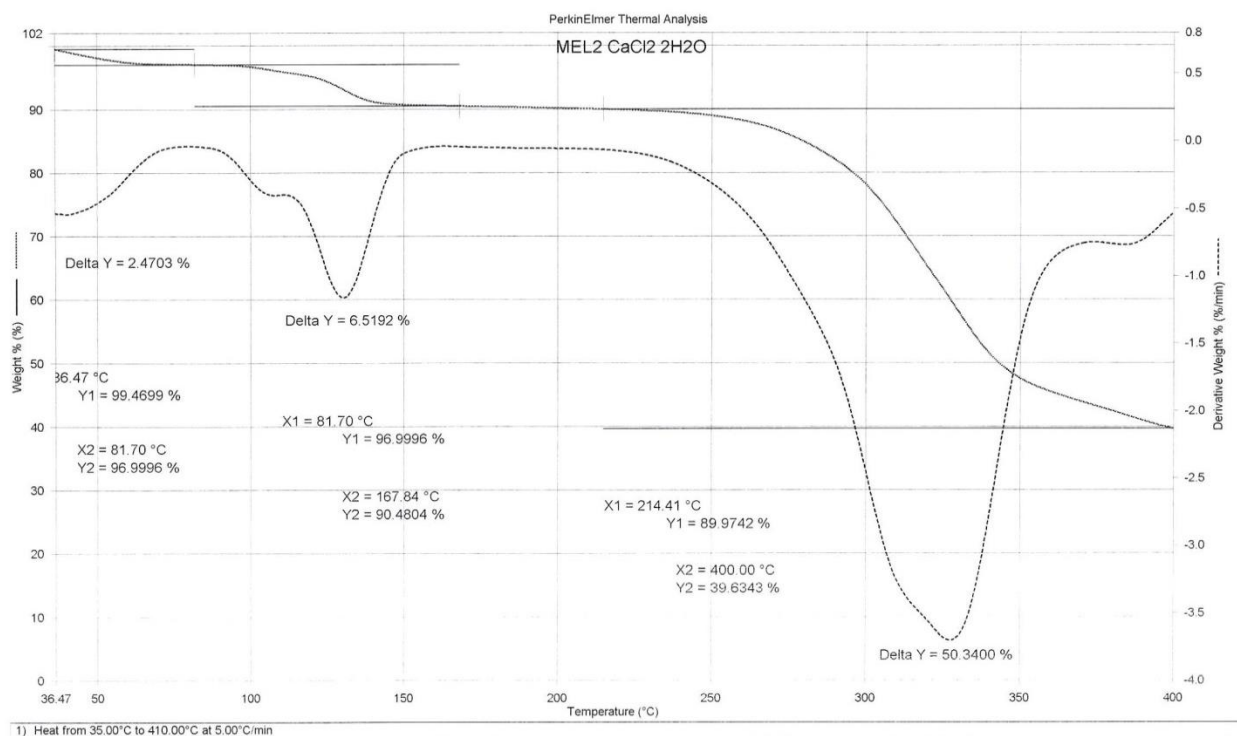


Figure 3.3.5-7 TGA of $\text{mel}_2 \cdot \text{CaCl}_2 \cdot 2\text{H}_2\text{O}$.

Filename: C:\Progr...MEL2 CaCl2 2H2O_H PA 28mag.pdlid
 Operator ID: KR
 Sample ID: MEL2 CaCl2 2H2O PA
 Sample Weight: 3.220 mg
 Comment: heating

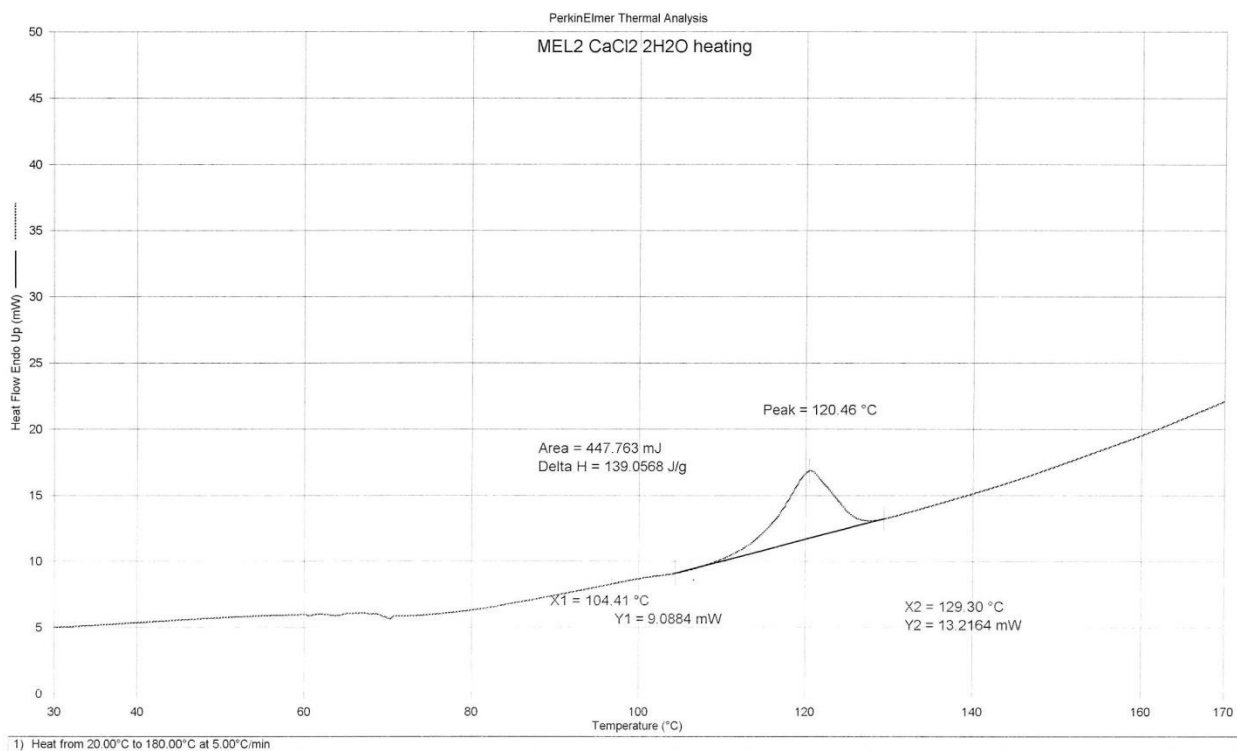


Figure 3.3.5-8 DSC of $\text{mel}_2 \cdot \text{CaCl}_2 \cdot 2\text{H}_2\text{O}$.

XRPD: comparison between reagents and products

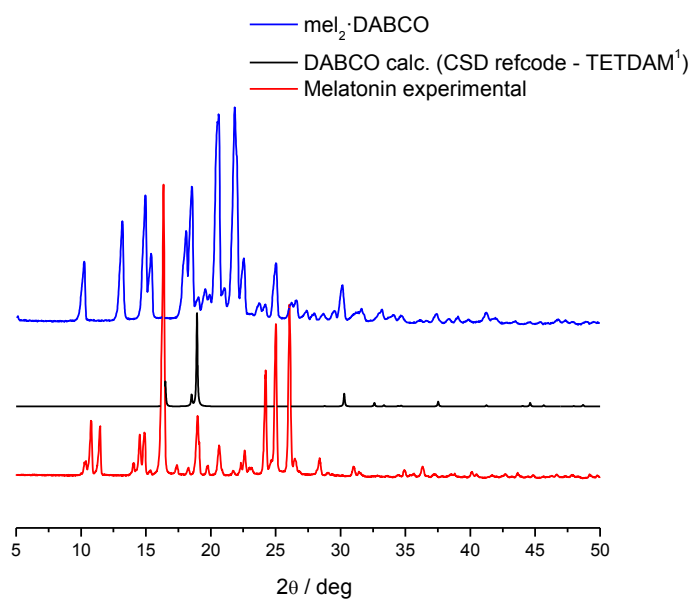


Figure 3.3.5-9 XRPD comparison between mel₂·DABCO and starting materials.⁶⁷

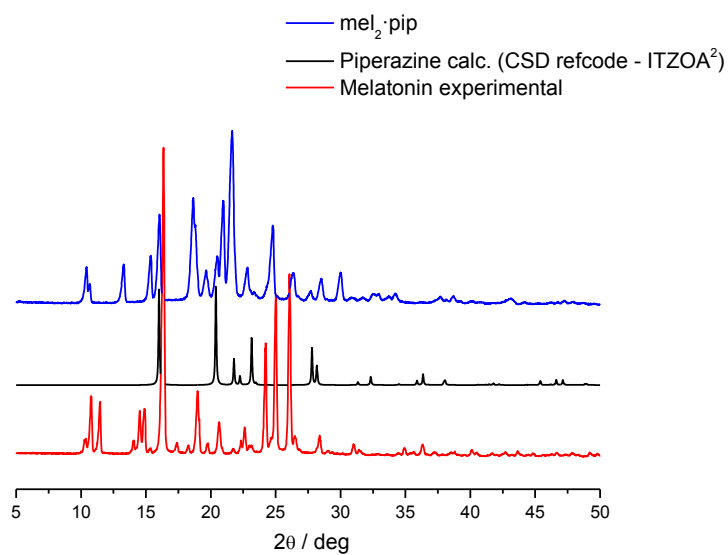


Figure 3.3.5-10 XRPD comparison between mel₂·pip and starting materials.⁶⁸

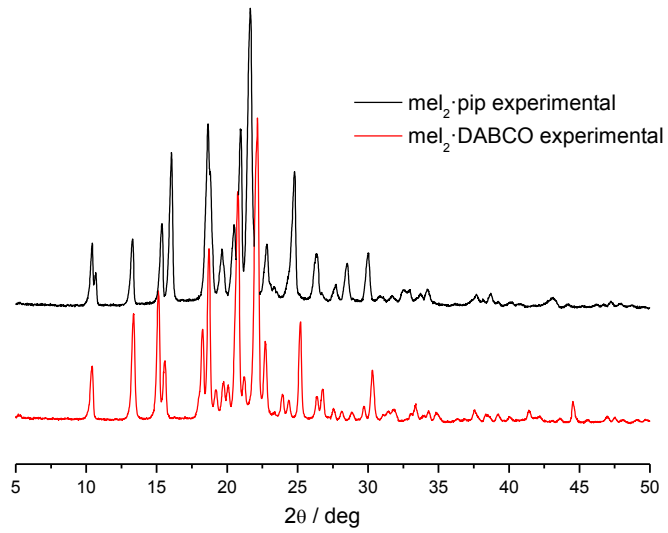


Figure 3.3.5-11 Comparison between the XRPD patterns of the mel₂·pip and mel₂·DABCO co-crystals.

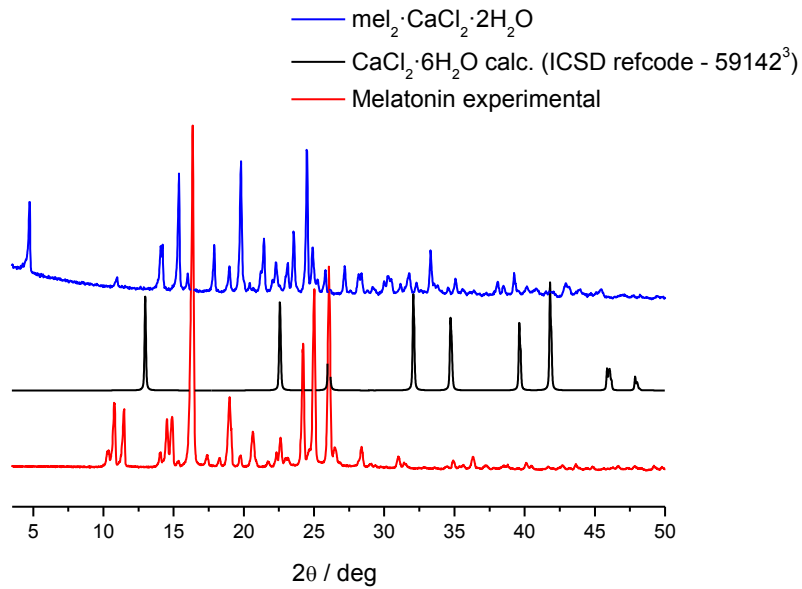


Figure 3.3.5-12 XRPD comparison between mel₂·CaCl₂·2H₂O and starting materials.⁶⁹

Rietveld refinements

Experimental (blue curve), calculated (red curve), and difference (grey curve) powder patterns. Peak positions are marked in blue.

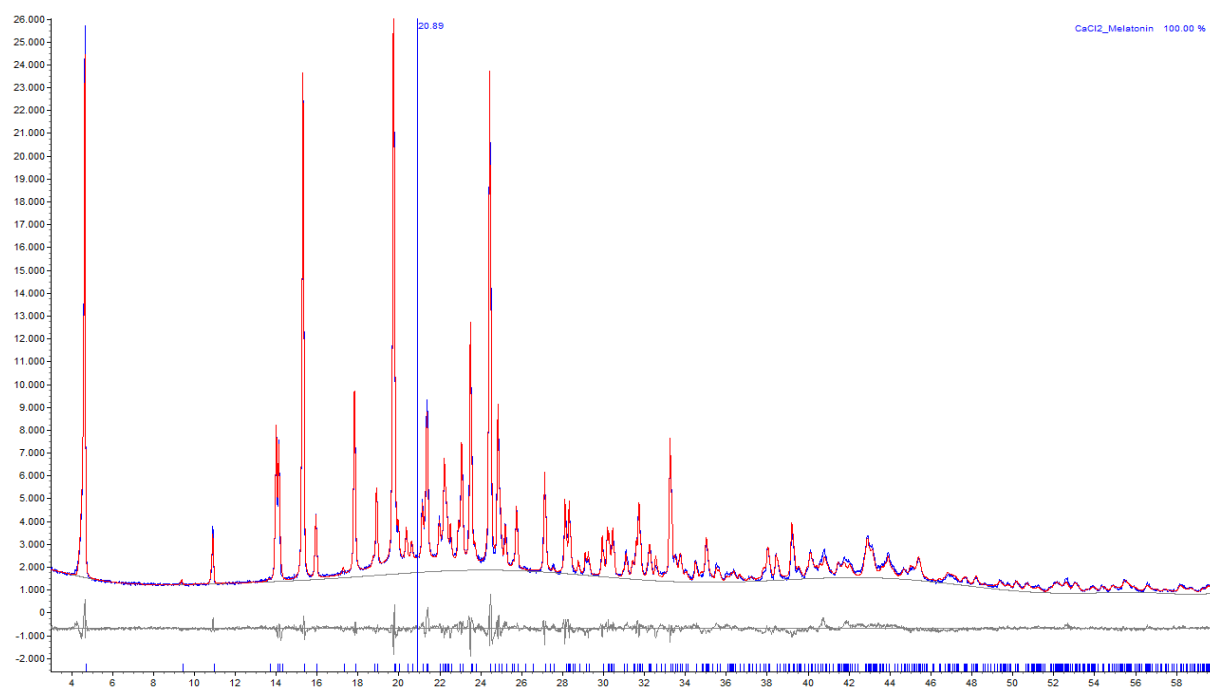


Figure 3.3.5-13 Rietveld refinement of $\text{mel}_2 \cdot \text{CaCl}_2 \cdot 2\text{H}_2\text{O}$.

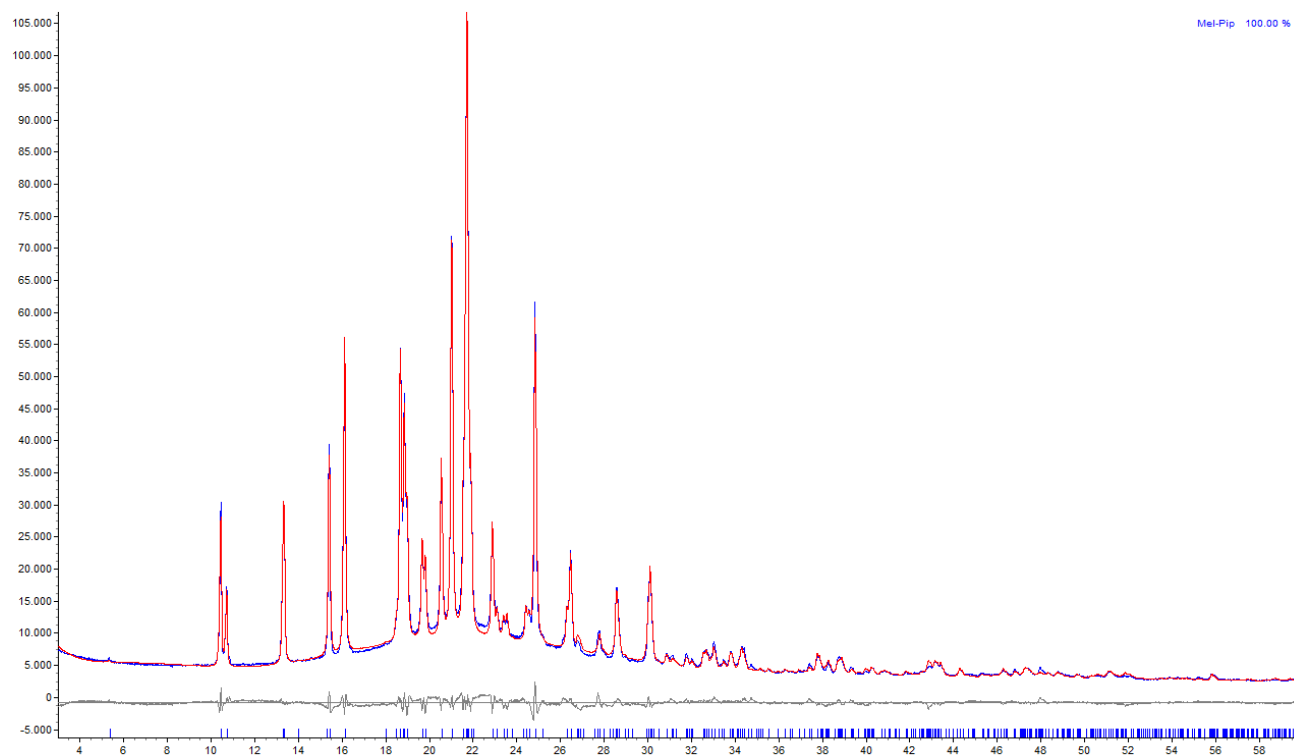


Figure 3.3.5-14 Rietveld refinement of $\text{mel}_2 \cdot \text{pip}$.

Tables of co-formers tested.

Table 3.3.5-1 Organic acids.

#	Co-former	Method	Results
1	Nicotinic acid	Kneading with EtOH	✗
2	Fumaric acid	Kneading with EtOH	✗
3	Isophthalic acid	Kneading with EtOH	✗
4	4-aminosalicylic acid	Kneading with EtOH	✗
5	Succinic acid 1:2	Kneading with EtOH	✗
6	Glutaric acid 1:2	Kneading with EtOH	✗
7	Ascorbic acid	Kneading with EtOH	✗
8	Barbituric acid	Kneading with EtOH	✗
9	Nalidixic acid	Kneading with EtOH	✗

Table 3.3.5-2 Amino acids.

#	Co-former	Method	Results
1	L-tryptophan	Kneading with EtOH	✗
2	L-Glutamic acid	Kneading with EtOH	✗
3	L-Glutamine	Kneading with EtOH	✗
4	L-Histidine	Kneading with EtOH	✗
5	L-aspartic acid	Kneading with EtOH	✗

Table 3.3.5-3 Inorganic salts.

#	Co-former	Method	Results
1	CaCl ₂	Kneading with EtOH	✓
		Slurry in EtOH	✓
		Evaporation from EtOH	✗
		Slurry in water	✗
2	MgCl ₂ ·6H ₂ O	Kneading with EtOH	✗
		Slurry in EtOH	✗
		Evaporation from EtOH	✗
3	KBr	Kneading with EtOH	✗
4	NaCl	Kneading with EtOH	✗
5	Sr(NO ₃) ₂	Kneading with EtOH	✗
6	LiCl	Kneading with EtOH	✗
		Slurry in EtOH	✗
		Evaporation from EtOH	✗
7	SrCl ₂ ·6H ₂ O	Kneading with EtOH	✗
8	NaBr	Kneading with EtOH	✗
9	ZnCl ₂	Kneading with EtOH	✗
		Slurry in EtOH	✗
		Evaporation from EtOH	✗
		Slurry in water	
10	AgNO ₃	Kneading with EtOH	✗
11	Cu(NO ₃) ₂ ·3H ₂ O	Kneading with EtOH	✗

Table 3.3.5-4 Phenols.

#	Co-former	Method	Results
1	Thymol	Kneading with EtOH Evaporation from EtOH	× ×
2	Eugenol	Kneading Slurry in the excess of eugenol Crystallization from eugenol	× × ×
3	Carvacrol	Kneading Slurry in the excess of carvacrol Crystallization from carvacrol	× × ×

Table 3.3.5-5 Nitrogen containing compounds.

#	Co-former	Method	Results
1	Quinoxaline	Kneading with EtOH	×
2	Morpholine	Kneading Slurry in the excess of morpholine	×
3	Piperazine	Kneading with EtOH Evaporation from EtOH Slurry in water	✓ × ×
4	DABCO (triethylenediamine)	Kneading with EtOH Evaporation from ethanol Slurry in water	✓ × ×
5	4,4'-bipyridine	Kneading with EtOH Slurry in EtOH Evaporation from EtOH	×
6	ε-Caprolactam	Kneading with EtOH	×
7	Caffeine anhydrous	Kneading with EtOH	×
8	4,4'-trimethylenedipiperidine	Kneading with EtOH	×
9	Hexamine	Kneading with EtOH Evaporation from EtOH	× ×
10	Carbamazepine	Kneading with EtOH	×
11	Pyrazine	Kneading with EtOH Slurry in EtOH	× ×
12	Quinuclidine	Kneading with EtOH	×
13	3-quinuclidinol	Kneading with EtOH	×
14	Adenosine	Kneading with EtOH Slurry in EtOH Evaporation from water/ethanol mixtures Crystallization from melt Solvothermal crystallization in water	× × × × ×
15	Urea	Kneading with EtOH	×
16	4-aminopyridine	Kneading with EtOH	×

Table 3.3.5-6 Various.

#	Co-former	Method	Results
1	Dioxane	Kneading Slurry in the excess of dioxane	× ×
2	Benzoquinone	Kneading with EtOH	×

3.3.6. Conclusions

In this chapter the results of a systematic exploration of the possibility of preparing co-crystals of melatonin with a number of co-formers have been reported. Two molecular co-crystals and one ionic co-crystal of melatonin have been obtained. The structures of mel₂·pip and mel₂·CaCl₂·2H₂O co-crystals were established by X-ray powder diffraction. The latter showed an 8-fold higher thermodynamic solubility characteristics compared to those of melatonin.

3.4. Exploring chiral resolution in the solid-state via ionic co-crystal formation.

The idea developed in this part of the research combines the issue of chirality with that of ionic co-crystal formation. Initially, the scope of this research was more general: to apply the formation of both molecular and ionic co-crystals as a tool to either separate a particular enantiomer from a racemic mixture or to prevent its possible transformation into a different form. However, after some preliminary results on the co-crystallization of both enantiopure and racemic histidine with lithium halides were obtained⁵⁰, we decided to focus all our efforts on the ICCs. Li⁺ cations selectively link to molecules of the same chirality, forming enantiopure chains, resulting in some of the cases in a chiral resolution process in the solid state via conglomerate formation. The co-crystallization of the investigated amino acid with calcium halides did not show any effect on the chirality of the obtained ionic co-crystals.⁵¹ Taking into account the obtained results, it was speculated that one possible reason for chiral preference in ICCs formed by DL-histidine and lithium halides could be the nature of the cation which favours the coordination of molecules of the same handedness. We decided to put this hypothesis to test by attempting the co-crystallization of another amino acid – DL-proline with lithium halides.⁵² The obtained results appeared to be quite similar with those obtained for the co-crystallization of histidine with lithium halides: once again the homochiral preference of lithium cations was observed in all the ICCs. In order to understand whether the phenomenon of lithium homochiral preference could be explained by a particular phenomenon of lithium cations *per se* or by the tetrahedral geometry around the lithium cations that could favour the coordination of molecules of the same handedness, it was decided to perform the complexation with a different metal cation favouring a tetrahedral

coordination. This time an antiepileptic drug – levetiracetam (enantiopure *S*-etiracetam) and its racemic intermediate *RS*-etiracetam was co-crystallized with ZnCl_2 ,⁷⁰ as zinc is known to favour tetrahedral coordination. In agreement with our working hypothesis, the complexation of the racemic etiracetam to zinc cations appeared to be enantioselective.

3.4.1. Ionic Co-crystals of Racemic and Enantiopure Histidine: An Intriguing Case of Homochiral Preference

The investigation of the peculiarities of co-crystallization of chiral compounds was started with the amino acid histidine and alkali chlorides and bromides.⁵⁰ The grinding with a drop of solvent (kneading¹⁸) was chosen for the preliminary screening. The obtained results showed that only the co-crystallization of lithium chloride and lithium bromide led to the formation of new phases. Consequently, it was decided to concentrate our efforts on the interaction of L- and DL-histidine with lithium halides. The obtained results appeared to be quite interesting. As it could be expected, lithium cations had a tetrahedral coordination. It was formed by three different molecules of histidine and a molecule of water. However, the most intriguing aspect was the enantioselective complexation of the racemic amino acid to lithium cations: each Li^+ was selectively coordinated by the amino acids of the same handedness forming the infinite chains of L-histidine· Li^+ and D-histidine· Li^+ . Furthermore, it was found that the enantiopure chains observed in both racemic and conglomerate crystals are of the same type observed in the ICCs prepared with enantiopure L-Histidine. And as it was found out later, this peculiar coordinative feature could not only result into formation of these enantiopure chains, but also lead to the spontaneous chiral resolution with the formation of conglomerates.

A detailed report on the co-crystallization of enantiopure and racemic histidine with lithium halides has been recently published.



Article

Ionic Cocrystals of Racemic and Enantiopure Histidine: An Intriguing Case of Homochiral Preference

Dario Braga*, Lorenzo Degli Esposti, Katia Rubini, Oleksii Shemchuk, and Fabrizia Grepioni

Dipartimento di Chimica "G. Ciamician", Università degli Studi di Bologna, via Selmi 2, 40126 Bologna, Italy

Cryst. Growth Des., 2016, 16 (12), pp 7263–7270

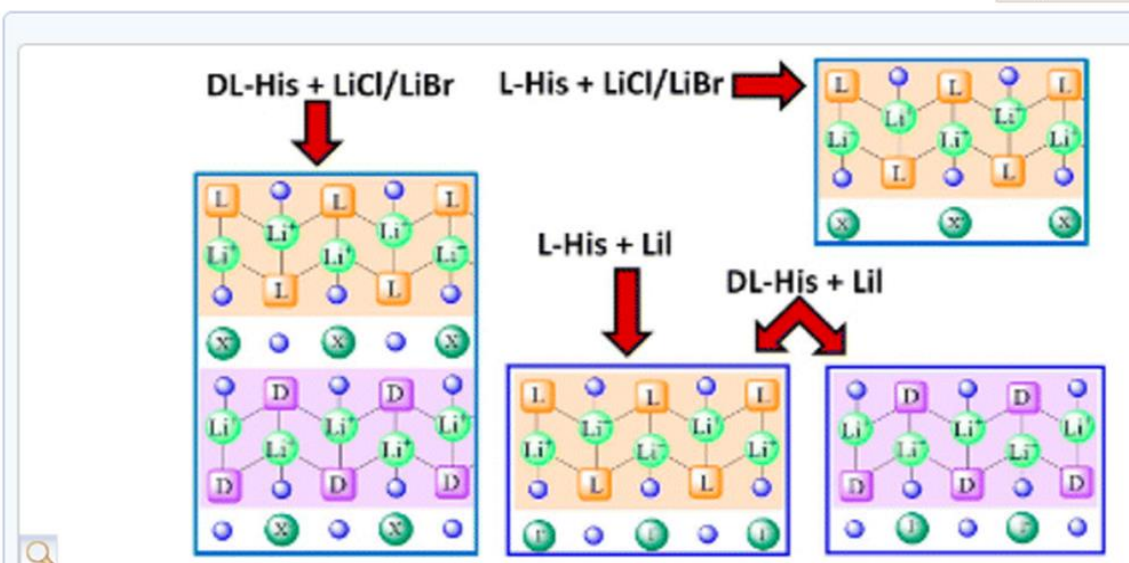
DOI: 10.1021/acs.cgd.6b01426

Publication Date (Web): November 11, 2016

Copyright © 2016 American Chemical Society

Abstract

Jump to a secti



Ionic cocrystals (ICC) of L- and DL-histidine with lithium halides (LiCl, LiBr, LiI) have been prepared by solid state and solution methods, and structurally characterized in order to compare the behavior of enantiopure and racemic crystals in the interaction with inorganic salts. It has been shown that the lithium cations interact selectively with enantiomers of one handedness only, to the extent that the crystals obtained with racemic DL-histidine can be described as a special type of cocrystals made of enantiopure L-histidine and D-histidine chains of the same type as those obtained with enantiopure L-histidine. This chiral preference is even more noticeable in the ICC obtained from DL-histidine and LiI, which is actually a conglomerate of L- and D-ICCs. It is also reported that attempts to prepare ICCs with other alkali/alkaline earth halides invariably yield crystals of the less stable polymorph of L-histidine.

For copyright reasons only the link to the original article is reported here:

<https://pubs.acs.org/doi/abs/10.1021/acs.cgd.6b01426>

3.4.2. Ionic Co-crystals of Racemic and Enantiopure Histidine: An Intriguing Case of Homochiral Preference

The promising results of the co-crystallization of the racemic histidine with lithium halides encouraged us to further investigate the influence of the complexation of D- and L-histidine molecules to metal cations. Since histidine did not form ICCs with all the alkali metals but lithium we decided to co-crystallize it with calcium halides. The interaction of both racemic and enantiopure histidine resulted into formation of the corresponding ionic co-crystals of the general formula $(L\text{-His})_2 \cdot \text{CaX}_2 \cdot n\text{H}_2\text{O}$ ($X = \text{Cl}$ and Br $n=3$, $X = \text{I}$ $n=4$). However, this time the complexation of the racemic histidine to calcium cations had no influence on the chirality: the obtained ICCs accommodated molecules of both chiralities in the coordination sphere of the Ca^{2+} cations. Intrinsic dissolution rate measurements show that the histidine- CaCl_2 co-crystals have a much higher IDR with respect to both enantiopure and racemic histidine solids. A detailed report on the co-crystallization of enantiopure and racemic histidine with calcium halides is given in our paper.



Ionic co-crystals of enantiopure and racemic histidine with calcium halides

[O. Shemchuk](#)^a, [L. Degli Esposti](#)^b, [F. Grepioni](#)^a and [D. Braga](#)^{*a}

⊕ Author affiliations

Abstract

Ionic co-crystals (ICCs) of L- and DL-histidine with CaCl_2 , CaBr_2 and CaI_2 were prepared by mechanochemical and solution methods and were structurally characterized by either single crystal or powder X-ray diffraction methods. The L-histidine molecules bridge Ca^{2+} cations forming enantiopure ribbons in the homochiral crystals $(\text{L-His})_2\text{-CaX}_2\cdot n\text{H}_2\text{O}$ ($X = \text{Cl}$ and Br $n = 3$, $X = \text{I}$ $n = 4$), as well as in the partial dehydration product of $(\text{L-His})_2\text{-CaI}_2\cdot 4\text{H}_2\text{O}$, namely $(\text{L-His})_2\text{-CaI}_2\cdot 3\text{H}_2\text{O}$. In the racemic $(\text{DL-His})_2\text{-CaX}_2\cdot 4\text{H}_2\text{O}$ cases ($X = \text{Cl}$, Br , $X = \text{I}$), molecules of both chiralities are accommodated in the coordination sphere of the Ca^{2+} cation forming ribbons with homochiral rims as in the enantiopure crystals. Intrinsic dissolution rate measurements show that the histidine- CaCl_2 co-crystals have a much higher IDR with respect to both enantiopure and racemic histidine solids.

For copyright reasons only the link to the original article is reported here:

<https://pubs.rsc.org/en/content/articlelanding/2017/ce/c7ce01326d#!divAbstract>

3.4.3. Ionic Co-crystal Formation as a Path Towards Chiral Resolution in the Solid State

As it was already mentioned in chapter 3.3.1, the co-crystallization of DL-histidine and lithium halides led to the formation of racemic co-crystals. In these co-crystals lithium cation exhibited a clear-cut homochiral preference: Li^+ cations were selectively bound to molecules of single handedness thus forming infinite “enantiopure” $(\text{L-His}\cdot\text{Li})_n^{n+}$ / $(\text{D-His}\cdot\text{Li})_n^{n+}$ chains. The co-crystallization with lithium iodide proceeded a step further along the path towards chiral separation, and the conglomerate of $\text{D-His}\cdot\text{LiI}\cdot\text{H}_2\text{O}$ and $\text{L-His}\cdot\text{LiI}\cdot\text{H}_2\text{O}$ was obtained.⁵⁰

A different behaviour was observed for calcium halides: racemic ICCs with DL-histidine were obtained,⁵¹ in which each calcium cation formed an octahedral coordination with histidine molecules of both chiralities.

Taking into account the information given above, it was speculated that the lithium cation tetrahedral coordination could be the key factor in the lithium homochiral preference. In order to test this assumption, we decided to co-crystallize lithium halides with another amino acid proline. One more important aspect we planned to investigate was the possible role of the size of the anion in the chiral resolution since it took place only in the co-crystallization of DL-histidine with lithium iodide.⁵⁰

This time the co-crystallization of both enantiopure and racemic proline with lithium halides was investigated more detailed: different solvents, stoichiometric ratios and synthetic techniques were used. Since the majority of ICCs were obtained in the form of hydrates, the thermal behaviour of the products and its impact on the chirality were also investigated.

Full Paper |  Full Access |

Ionic Co-Crystal Formation as a Path Towards Chiral Resolution in the Solid State

Oleksii Shemchuk, Boryana K. Tsenkova, Prof. Dario Braga, Prof. M. Teresa Duarte , Dr. Vânia André, Prof. Fabrizia Grepioni 

First published: 19 July 2018 | <https://doi.org/10.1002/chem.201802446>

A-Link Università di Bologna

Read the full text >

 PDF  TOOLS  SHARE

Abstract

The preparation and characterization of a whole family of hydrated ionic co-crystals formed by both enantiopure L-proline and racemic DL-proline with LiX (X=Cl, Br, I) are reported. The chiral preference of the lithium cation for homochiral coordination, both in the formation of crystalline conglomerates (with Cl and Br) and racemates (with Cl and I), in which molecules of opposite chirality are confined to distinct crystal layers, is discussed. Dehydration processes for all hydrated crystals have also been investigated.

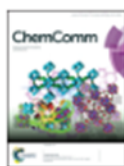
For copyright reasons only the link to the original article is reported here:

<https://onlinelibrary.wiley.com/doi/abs/10.1002/chem.201802446>

3.4.4. Solid-state chiral resolution mediated by stoichiometry: crystallizing etiracetam with ZnCl₂

Based on the information obtained by the co-crystallization of amino acids histidine and proline with lithium and calcium halides it was argued whether the phenomenon of lithium homochiral preference could be explained by a particular phenomenon of lithium cations *per se* or by the tetrahedral geometry around them that could favour the coordination of molecules of the same handedness. In order to find it out it was decided to perform the complexation with a different metal cation favouring a tetrahedral coordination. This time zinc in the form of their ZnCl₂ salt was used, as zinc is known to favour tetrahedral coordination. Instead of using an amino acid we decided to try and to co-crystallize ZnCl₂ with an antiepileptic drug – levetiracetam (enantiopure *S*-etiracetam) and its racemic intermediate – *RS*-etiracetam.

In agreement with our working hypothesis, the complexation of the racemic etiracetam to zinc cations appeared to be enantioselective. Moreover, in this particular case it was possible to use different amounts of ZnCl₂ to reversibly switch between a racemic compound and a conglomerate.



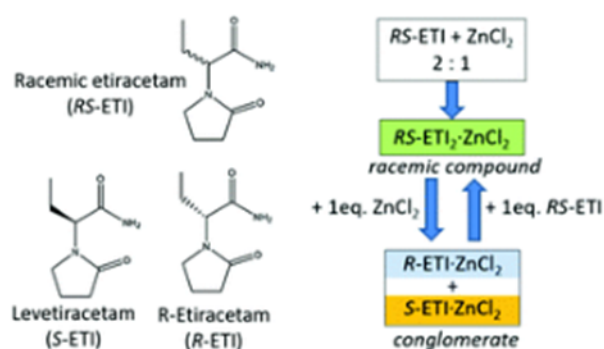
Solid-state chiral resolution mediated by stoichiometry: crystallizing etiracetam with ZnCl_2

Oleksii Shemchuk,^a Lixing Song,^b Koen Robeyns,^b Dario Braga,^a Fabrizia Grepioni^{*a} and Tom Leysens^{*b}

⊕ Author affiliations

Abstract

Chiral resolution of racemic etiracetam was achieved via co-crystallization with ZnCl_2 . Depending on the amount of ZnCl_2 either a stable racemic compound or a stable conglomerate can be obtained. Excess ZnCl_2 triggers the quantitative conversion of the racemate into the conglomerate solid; this unprecedented behaviour was investigated through a racemate/ ZnCl_2 /solvent phase diagram.



For copyright reasons only the link to the original article is reported here:

<http://pubs.rsc.org/en/Content/ArticleLanding/2018/CC/C8CC06199H#!divAbstract>

3.4.4.1 Supplementary Information

The link to the supporting information is reported here:

<http://www.rsc.org/suppdata/c8/cc/c8cc06199h/c8cc06199h1.pdf>

1. Experimental Procedures

S-2-(2-oxopyrrolidin-1-yl)butanamide (Levetiracetam, S-ETI) was purchased from Xiamen Top Health Biochem Tech. Co., Ltd. (RS)-2-(2-oxopyrrolidin-1-yl)butanamide (Etiracetam, RS-ETI) was prepared by racemization of S-2-(2-oxopyrrolidin-1-yl)butanamide. 10g of S-2-(2-oxopyrrolidin-1-yl)butanamide together with catalytic amount (0.05 eq.) of MeONa were added to 10 mL of MeOH. The solution was kept at reflux under continuous stirring for 24h, and then cooled to room temperature. The compound crystallizes spontaneously. After filtration, the compound was washed twice with MeOH. The recovered compound was used as such. All the other reagents were purchased from Sigma and used without further purification.

1.1 Solution Synthesis. Equimolar quantities of the starting materials (S-ETI:ZnCl₂ 1:1 and RS-etiracetam:ZnCl₂ 2:1) were dissolved in 2 mL of ethanol at room temperature. Slow evaporation of the solvent at room temperature resulted in the formation of an oil-like substance, which after several days precipitated as complexes S-ETI·ZnCl₂ and RS-ETI₂·ZnCl₂.

1.2 Solid-state synthesis. Pure complexes of S-ETI·ZnCl₂ and RS-ETI₂·ZnCl₂ were obtained mechanochemically by ball-milling the stoichiometric ratios of the starting materials in an agate jar for 60 min in a Retsch MM200 ball miller, operated at a frequency of 25 Hz, with the addition of a drop of ethanol.

1.3 Slurry synthesis. S-ETI·ZnCl₂ and RS-ETI₂·ZnCl₂ were also obtained by slurring for 2 days, in the minimum quantity of ethanol, methanol or water, the starting materials in the appropriate stoichiometric ratio.

1.4 Thermogravimetric analysis. TG analyses for S-ETI·ZnCl₂ and RS-ETI₂·ZnCl₂ were performed with a TGA/SDTA 851 Mettler Toledo instrument. Samples were placed in open aluminium oxide crucibles annealed at 1100 °C. The heating rate was 2 °C/min over the range 25-350 °C. All experiments were carried out under nitrogen atmosphere.

TGA measurements for RS-ETI, S-ETI and R-ETI·ZnCl₂ / S-ETI·ZnCl₂ conglomerates were performed with a PerkinElmer TGA7 in the temperature range 40-500 °C under N₂ gas flow at a heating rate of 5.00 °C min⁻¹.

1.5 Differential Scanning Calorimetry. DSC measurements for S-ETI·ZnCl₂ and RS-ETI₂·ZnCl₂ were performed on a TA DSC2500 with T0 technology, after calibration with indium. Samples were placed in aluminium perforated T0 pans, under continuous nitrogen flow. A heating ramp at 5°C/min from 30°C to 250°C was applied for all samples.

DSC thermograms for RS-ETI, S-ETI and R-ETI·ZnCl₂ / S-ETI·ZnCl₂ conglomerates were recorded using a Perkin-Elmer Diamond. The samples (1-3 mg range), obtained through kneading were placed in open or Al-pans. All measurements were conducted at a heating rate of 5 or 10°C min⁻¹.

1.6 Ternary Phase Diagram. The ternary phase diagram (TPD) was constructed by slurring RS-ETI and ZnCl₂ in ethanol, varying the molar ratio of the starting materials from 0 to 1. Experiments were carried out in a number of 2 mL sealed vials, and the suspensions were stirred at constant temperature (25 °C) over 48 h. Seeding with all possible solid-state forms was performed to make sure that the system reached thermodynamic equilibrium. Afterwards the samples were filtered by sand core funnel. The solid phases were characterized by XRPD. Concentration of zinc in the supernatant solution could not be determined via HPLC, due to transparency to UV radiation. Hence, to determine the equilibrium compositions, necessary for the determination of the solubility lines, each experimental condition described above was repeated, but this time the samples were not filtered; small portions of solvent were added to the stirring mixtures every 30 minutes, until complete dissolution of the suspended solid was observed. This allowed the construction of the solubility line in

the ternary phase diagram (fig. ESI-1). TPDs were drawn with the software ProSim Ternary Diagram.

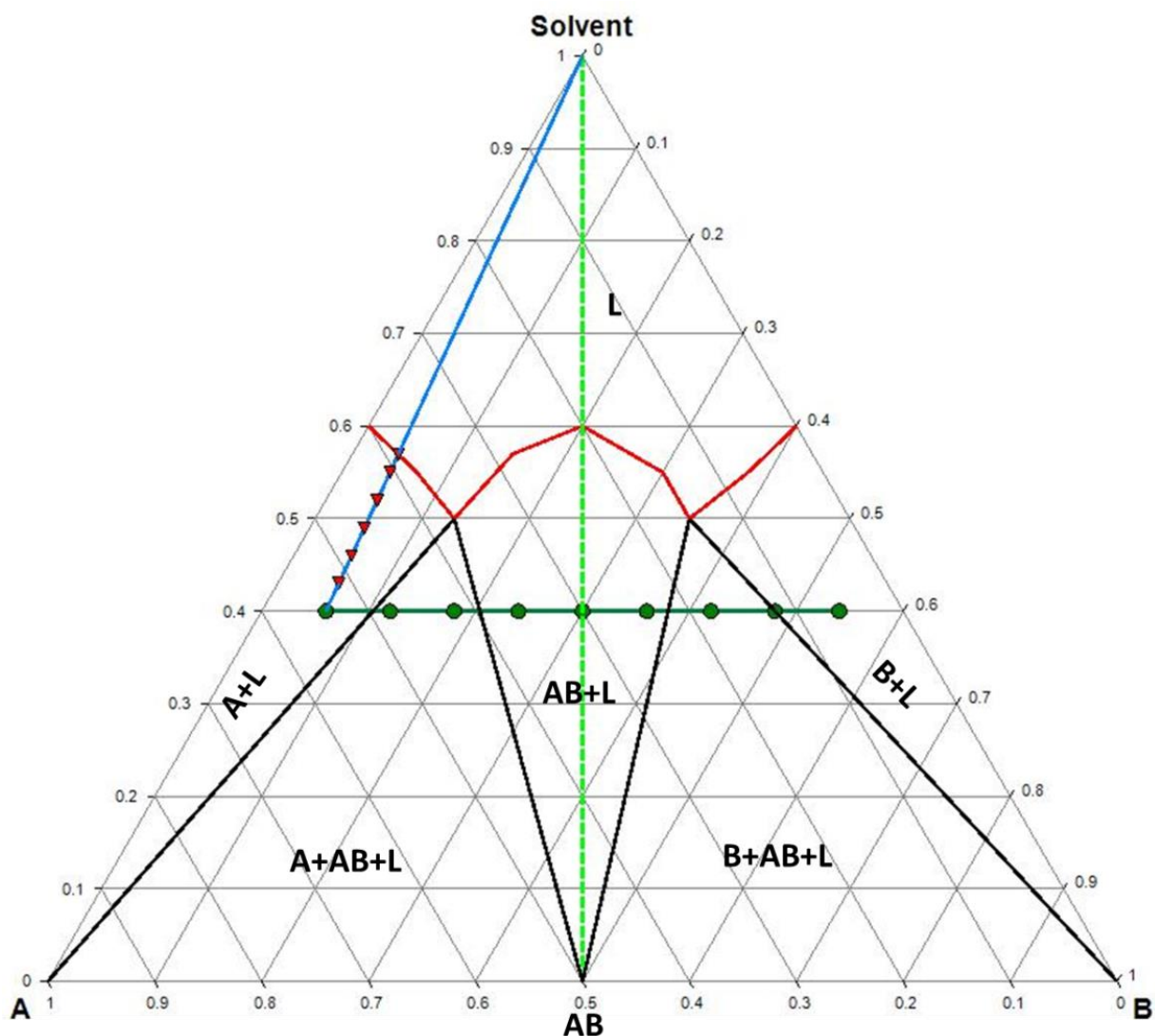


Fig. ESI-1. TPD of a generic co-crystal AB and a solvent; L is the liquid phase. Green dots: experimental ratios of the A and B components slurried in a fixed quantity of the solvent. Red broken line: solubility curve; this was determined by addition of small quantities of solvent to the known mixtures of the starting materials: in this figure the 9:1 of A:B ratio has been chosen as an example. The addition of solvent to the given suspension moves the composition towards the solvent vertex of this TPD (blue line). Each time solvent is added, one moves up a point on this line (red triangles).

2. X-ray diffraction analysis.

2.1 Single Crystal X-ray Diffraction. Single Crystal data were collected at room temperature with an Oxford Diffraction X'Calibur equipped with a graphite monochromator and a CCD detector. Mo-K α radiation ($\lambda = 0.71073 \text{ \AA}$) was used. Unit cell parameters for both complexes discussed herein are reported in Table ESI-1. The structure was solved by the Intrinsic Phasing methods and refined by least squares methods again F^2 using SHELXT-2014⁶⁴ and SHELXL-2018⁶⁵ with OLEX 2 interface.⁷¹ Non-hydrogen atoms were refined anisotropically. Hydrogen atoms were added in calculated positions and refined riding on their respective carbon or nitrogen atoms. The software Mercury 3.10.1⁷² was used for graphical representations and for powder patterns simulation on the basis of single crystal data.

Table ESI-1. Crystal data and details of measurements for S-ETI \cdot ZnCl $_2$ and RS-ETI $_2\cdot$ ZnCl $_2$.

	S-ETI\cdotZnCl$_2$	RS-ETI$_2\cdot$ZnCl$_2$
Chemical formula	C $_{16}$ H $_{28}$ Cl $_4$ N $_4$ O $_4$ Zn $_2$	C $_{16}$ H $_{28}$ Cl $_2$ N $_4$ O $_4$ Zn
M$_r$, g\cdotmol$^{-1}$	612.96	476.69
T / K	293 (2)	293 (2)
Morphology, colour	Block, colourless	Block, colourless
Crystal system	Monoclinic	Monoclinic
Space group	P2 $_1$	C2/c
a / \AA	6.3692 (3)	17.6678 (6)
b / \AA	11.6771 (4)	6.9371 (2)
c / \AA	17.1077 (6)	18.0628 (8)
α / $^\circ$	90	90
β / $^\circ$	98.496 (4)	91.515 (3)
γ / $^\circ$	90	90
V / \AA3	1258.40 (9)	2213.06 (14)
Z	2	4
d / mg\cdotcm$^{-3}$	1.618	1.431
μ / mm$^{-1}$	2.36	1.38
Measd reflns	6011	4853
Indep reflns	4612	2561
Reflns with $I > 2\sigma(I)$	4031	2118
R$_{int}$	0.024	0.027
R[F$^2 > 2\sigma(F^2)$]	0.0435	0.0425
wR(F2)	0.092	0.098

Crystal data can be obtained free of charge from the Cambridge Crystallographic Data Centre via <https://www.ccdc.cam.ac.uk> and have been allocated the accession numbers **CCDC 1857803** (RS-ETI $_2\cdot$ ZnCl $_2$) and **1857804** (S-ETI \cdot ZnCl $_2$).

2.2 X-ray Diffraction from Powder. For phase identification purposes X-ray powder diffraction (XRPD) patterns were collected on a PANalytical X'Pert Pro Automated diffractometer equipped with an X'celerator detector in Bragg-Brentano geometry, using Cu-K α radiation ($\lambda=1.5418$ Å) without monochromator in 3-50° 2 θ range (step size 0.033°; time/step: 20 s; Soller slit 0,04 rad, antiscatter slit: ½, divergence slit: ¼ ; 40 mA*40kV).

2.3 Variable temperature X-ray diffraction.

VT-XRPD diffractograms were collected in the 5-50° 2 θ range on a PANalytical X'Pert PRO automated diffractometer, equipped with an X'celerator detector and an Anton Paar TTK 450 system for measurements at controlled temperature. Data were collected in open air in Bragg-Brentano geometry, using Cu-K α radiation without a monochromator. Thermal programs were selected on the basis of TGA results.

3. Experimental results

3.1 RS-Etiracetam and S-Etiracetam.

Filename: C:\Program Files\Pyris...\Eter_H 15set.pdtd
Operator ID: KR
Sample ID: Eter pan aperto
Sample Weight: 5.400 mg
Comment: heating

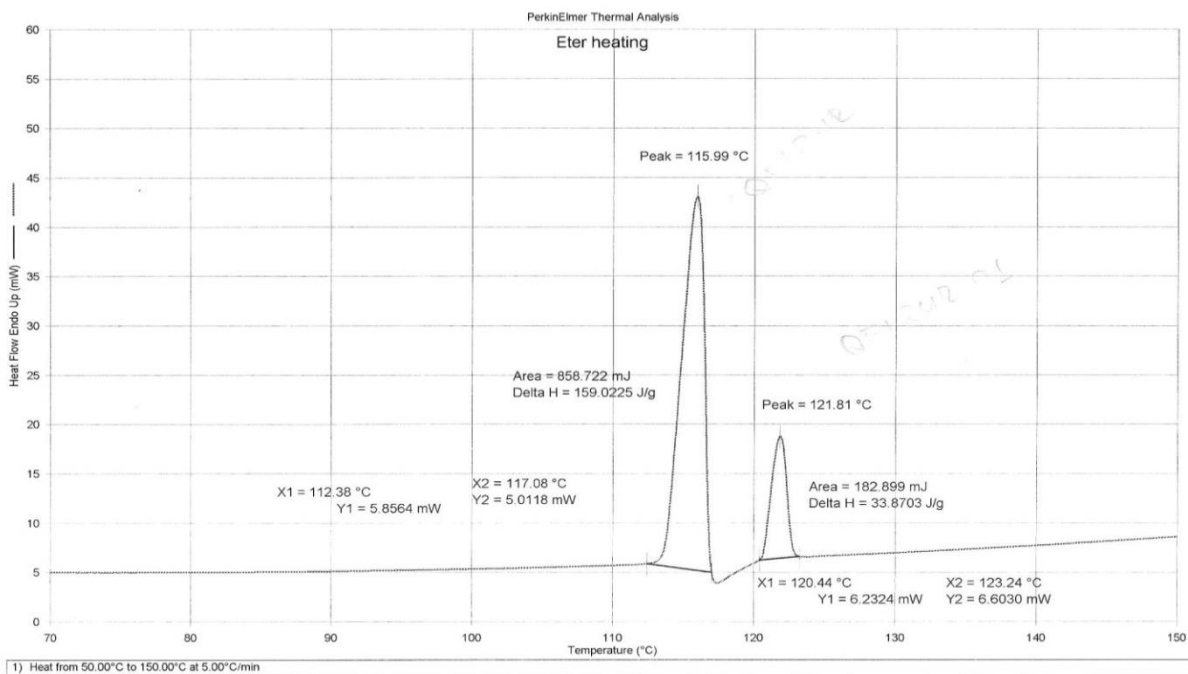


Fig. ESI-2. DSC trace for RS-ETI.

Filename: C:\Documents and Setting...\Eter 14set.pdtd
Operator ID: KR
Sample ID: Eter N2
Sample Weight: 4.620 mg
Comment:

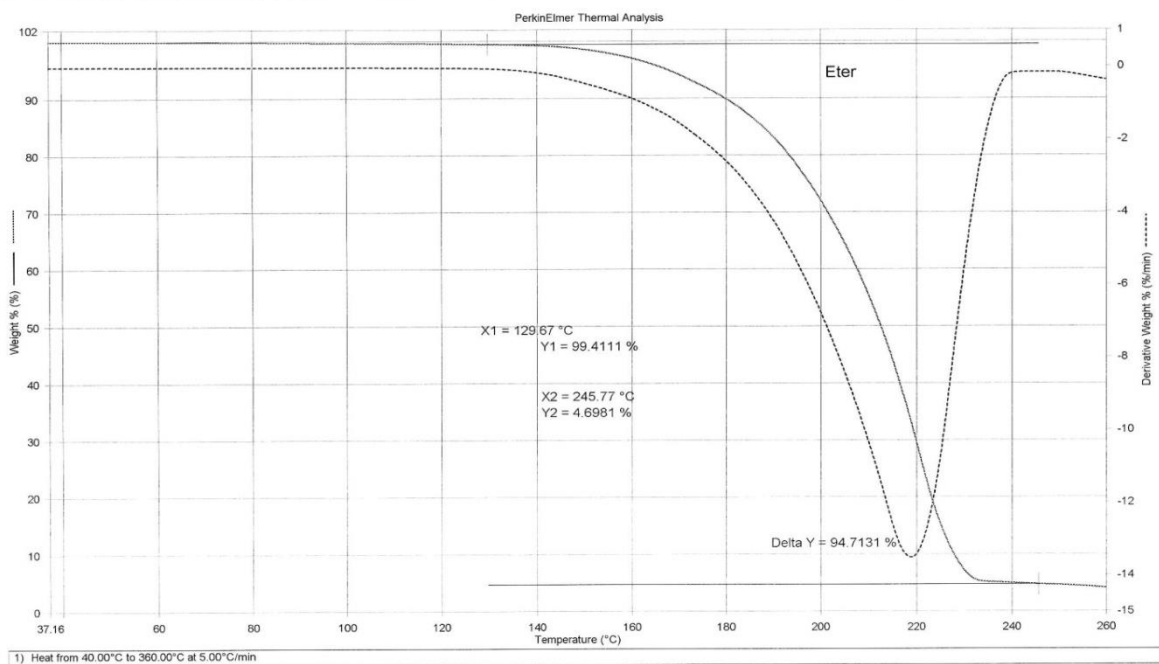


Fig. ESI-3. TGA of RS-ETI.

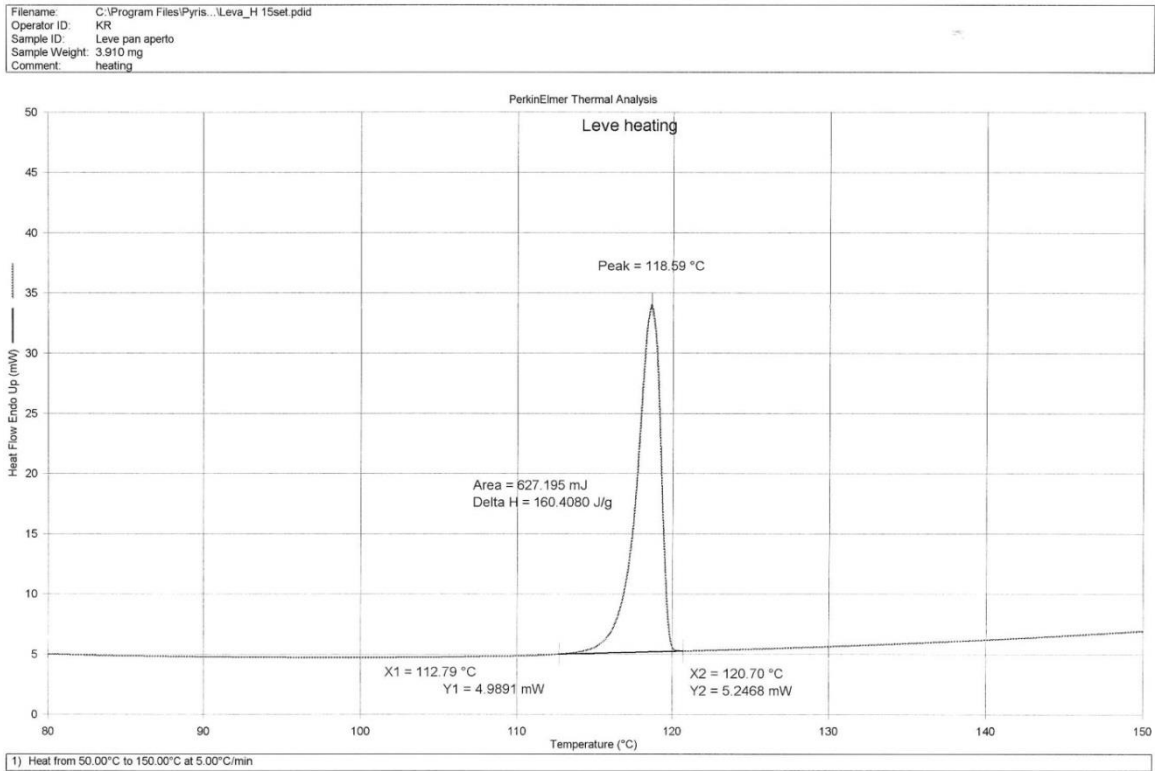


Fig. ESI-3. DSC trace for S-ETI.

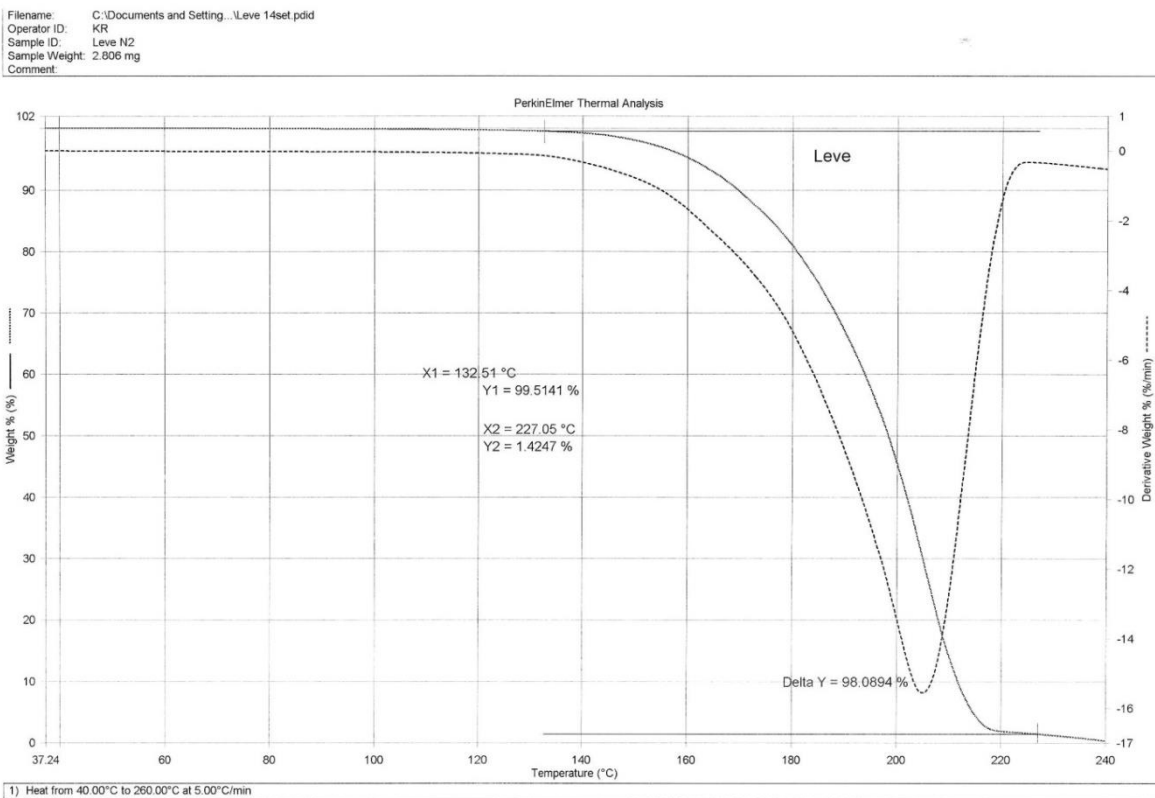


Fig. ESI-4. DSC thermogram of S-ETI.

3.2 RS-ETI₂·ZnCl₂

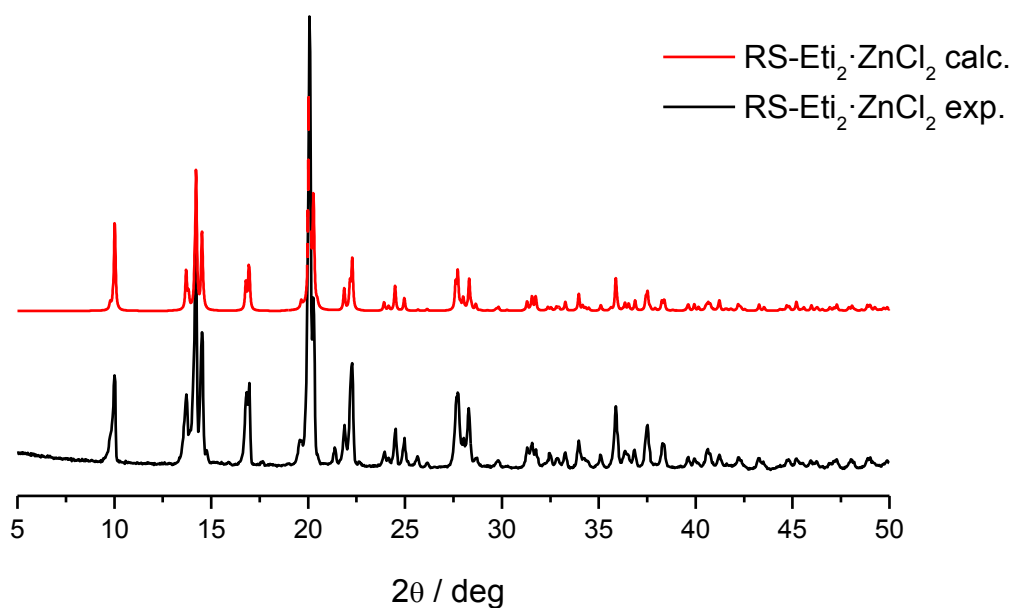


Fig. ESI-5. Comparison between the experimental (crystallization from solution) and calculated XRPD patterns for RS-ETI₂·ZnCl₂.

The TGA shows a degradation process starting at 200°C, with DSC showing a single melting process at 132°C (onset), ca. 40°C lower than the one observed for S-ETI·ZnCl₂ (see below). VT-XRPD confirms (i) the presence of only one form and (ii) the melting of that form at higher temperatures. Recrystallization from the melt is not observed.

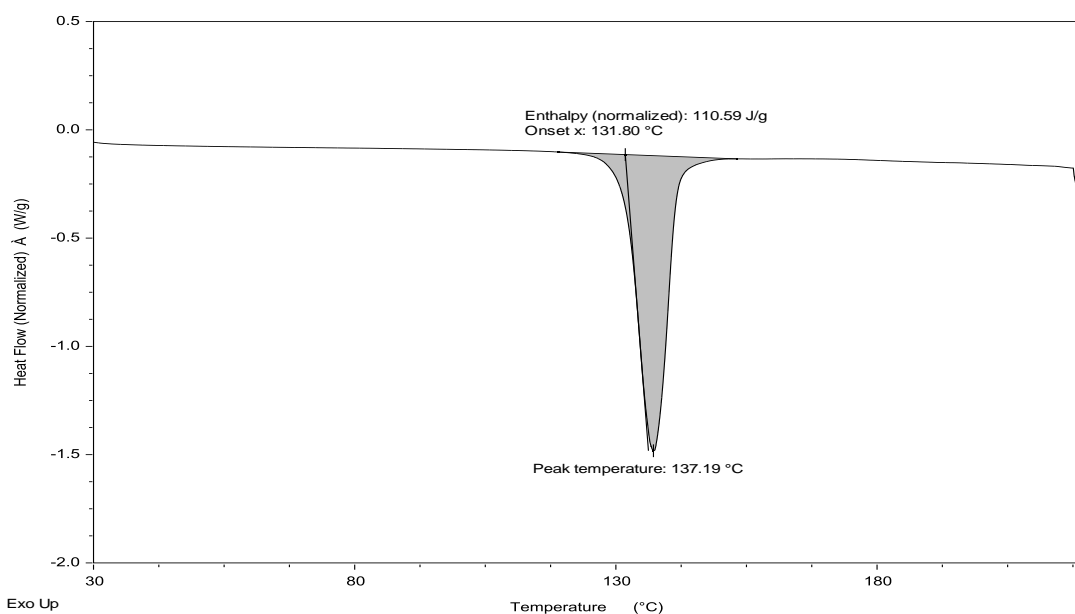


Fig. ESI-6. DSC trace of RS-ETI₂·ZnCl₂.

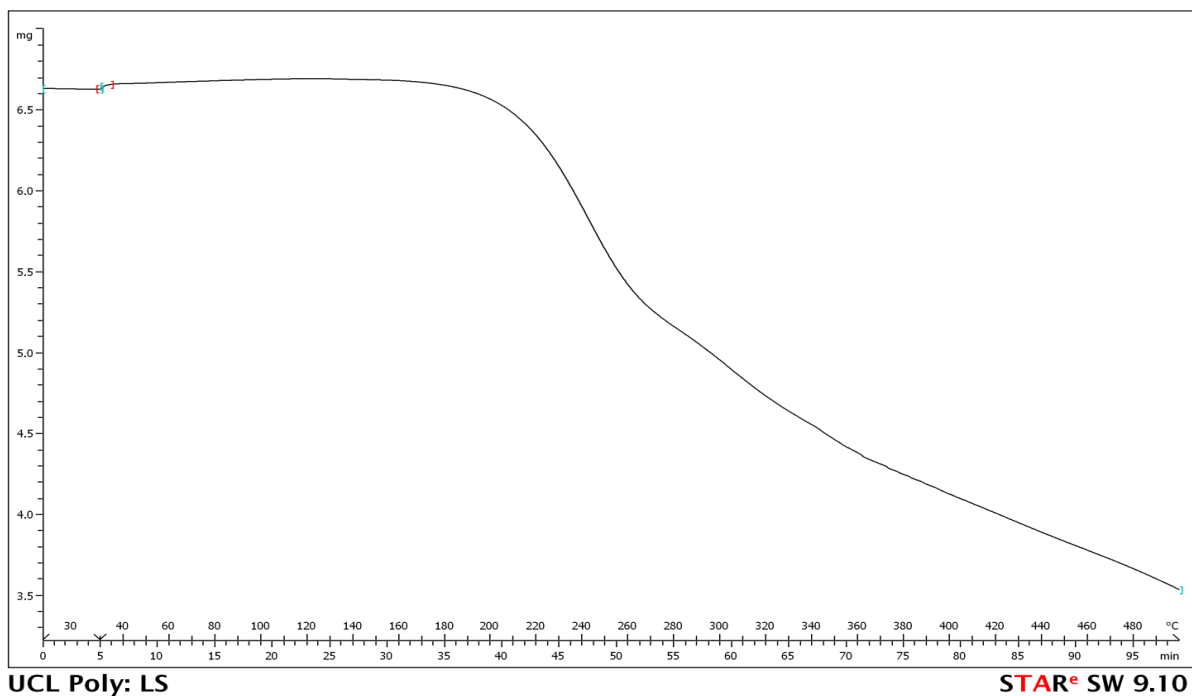


Fig. ESI-7.: TGA of RS-EtI₂·ZnCl₂.

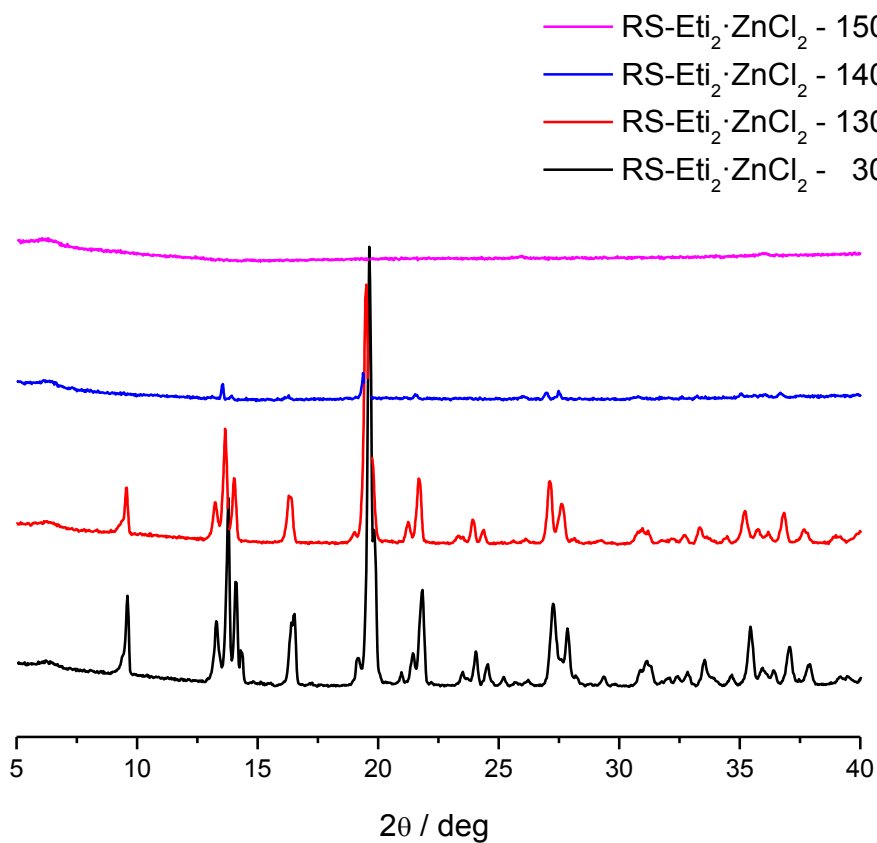


Fig. ESI-8.: VT-XRPD for RS-EtI₂·ZnCl₂.

3.3 S-ETI·ZnCl₂

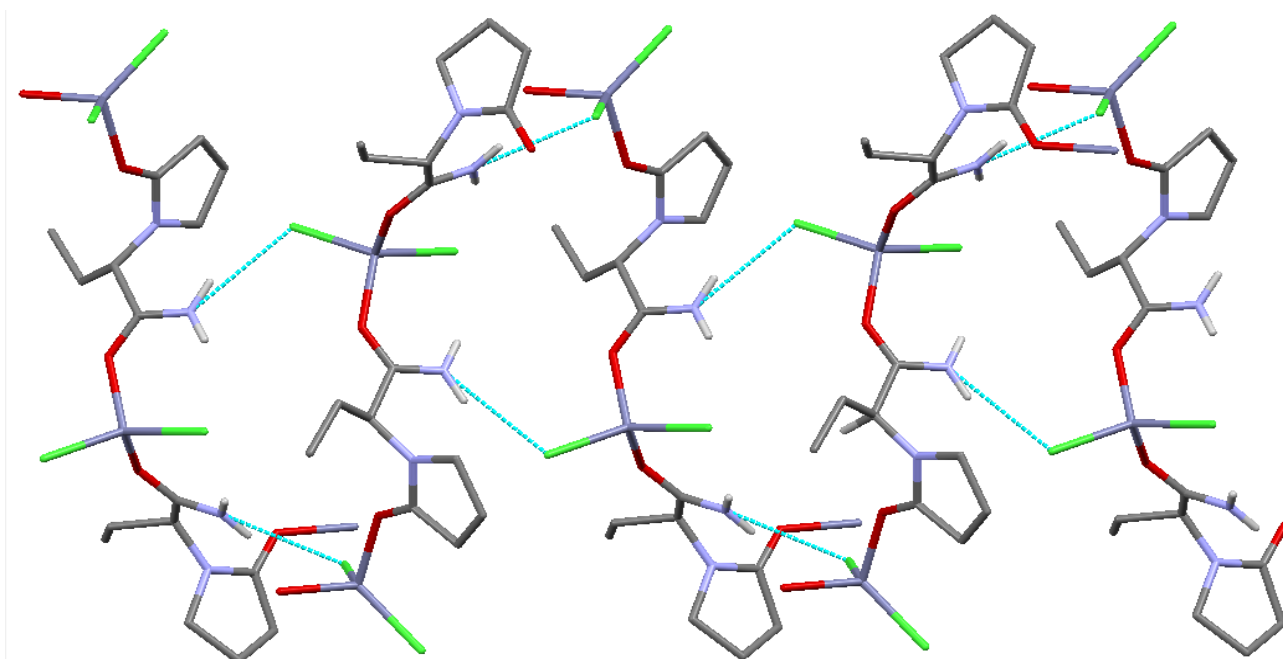


Fig. ESI-9. S-ETI·ZnCl₂. Hydrogen bonds between the chloride anions and the hydrogen atoms of the amido groups that hold together the zig-zag chains formed by ZnCl₂ units bridged by S-etiracetam molecules.

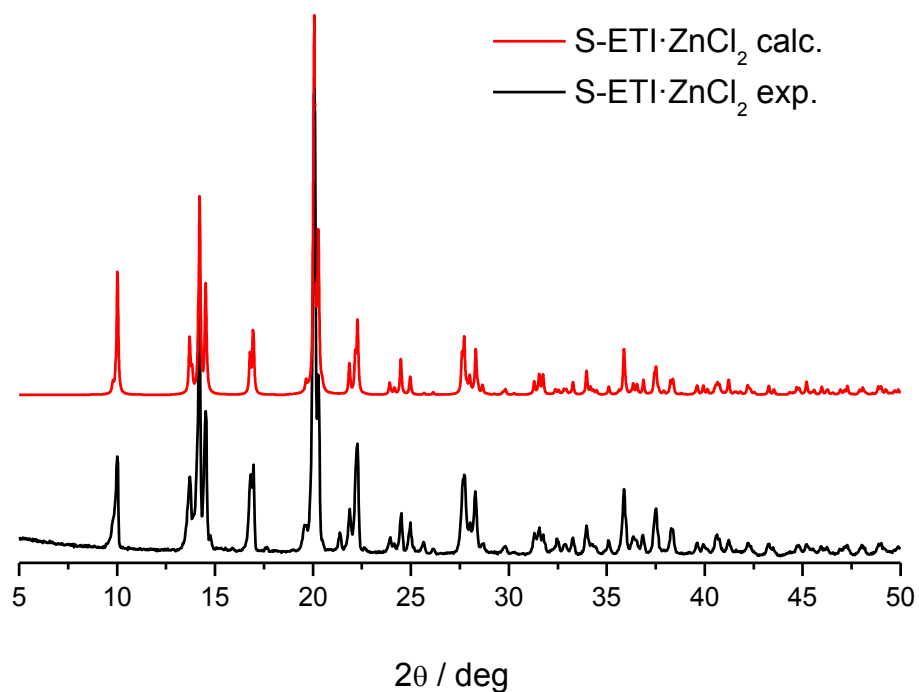


Fig. ESI-10. Comparison between the experimental (crystallization from solution) and calculated XRPD patterns for S-ETI·ZnCl₂.

The TGA trace shows a degradation process starting at 220°C. A small initial mass loss is likely due to removal of residual solvent adsorbed on the surface of the sample. A similar observation can be made on the basis of the DSC trace, which shows an initial endotherm, which can easily be attributed to evaporation of residual solvent; at 176°C (onset) melting is observed. VT-XRPD confirms that only one form is present and melting of that form occurs above 180°C. Recrystallization from the melt is not observed.

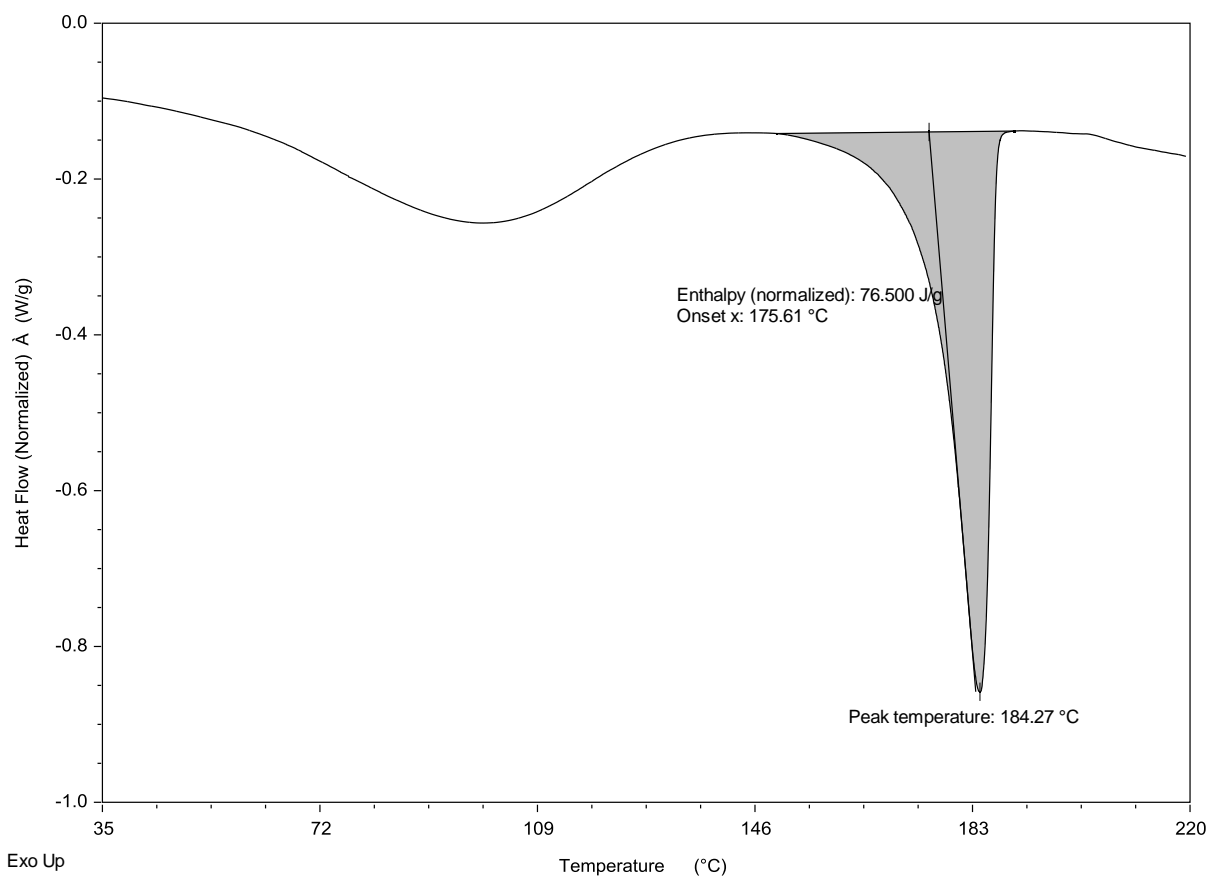
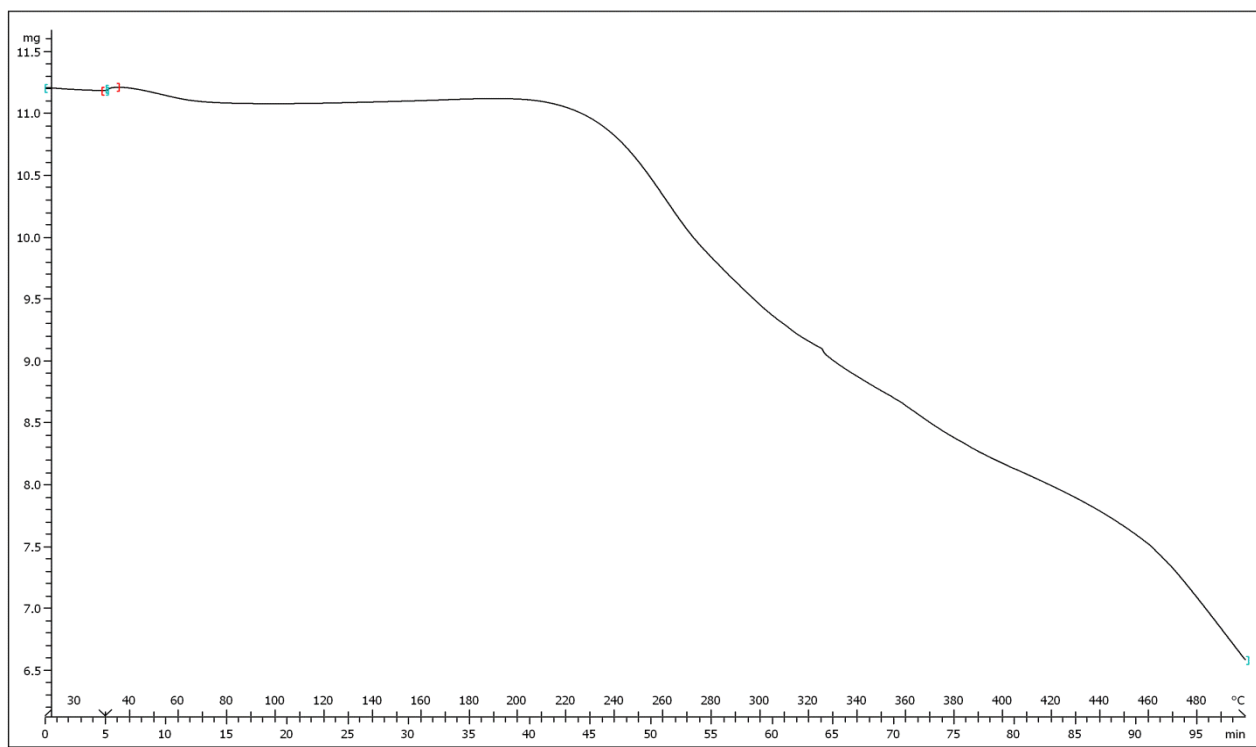


Fig. ESI-11. DSC thermogram of S-ETI·ZnCl₂.



UCL Poly: LS

STAR^e SW 9.10

Fig. ESI-12. TGA analysis of S-ETI·ZnCl₂.

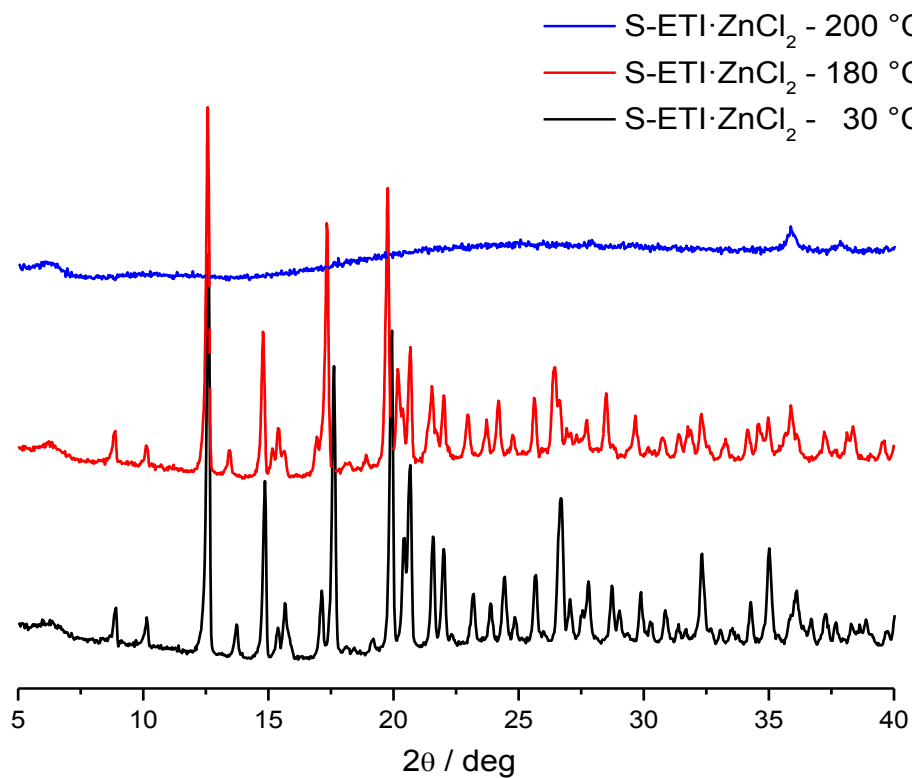


Fig. ESI-13. VT-XRPD for S-ETI·ZnCl₂.

3.4 *R*-ETI·ZnCl₂ / *S*-ETI·ZnCl₂ conglomerate

DSC analysis shows a single endothermic event, attributable to melting, at 156.64°C (onset), that is approximately 20 ° lower than the 176°C observed for the single enantiomer (Fig. ESI-11), as it can be expected for a conglomerate.⁷³

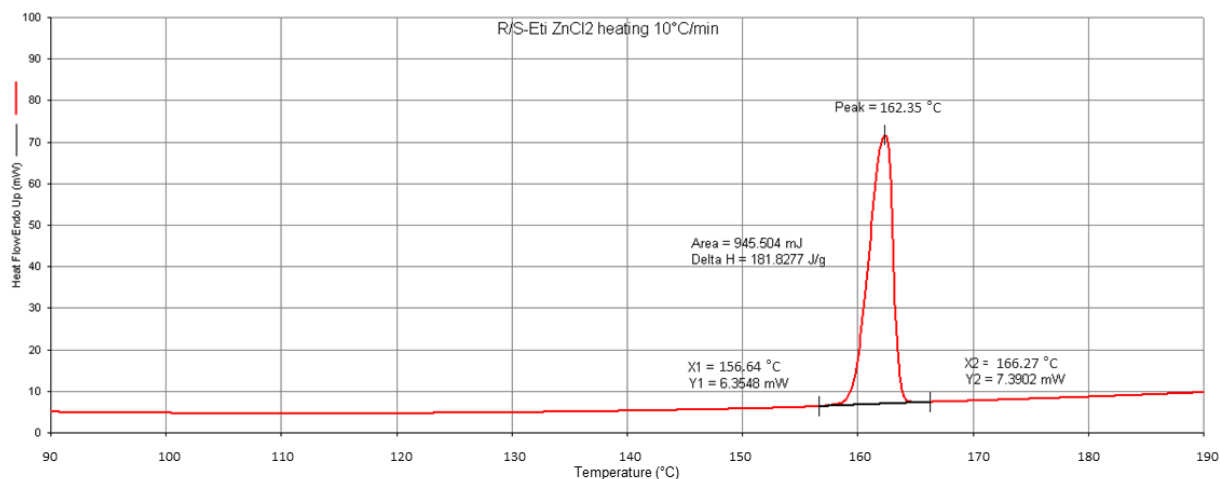


Fig. ESI-14. DSC trace for the *R*-ETI·ZnCl₂ / *S*-ETI·ZnCl₂ conglomerates.

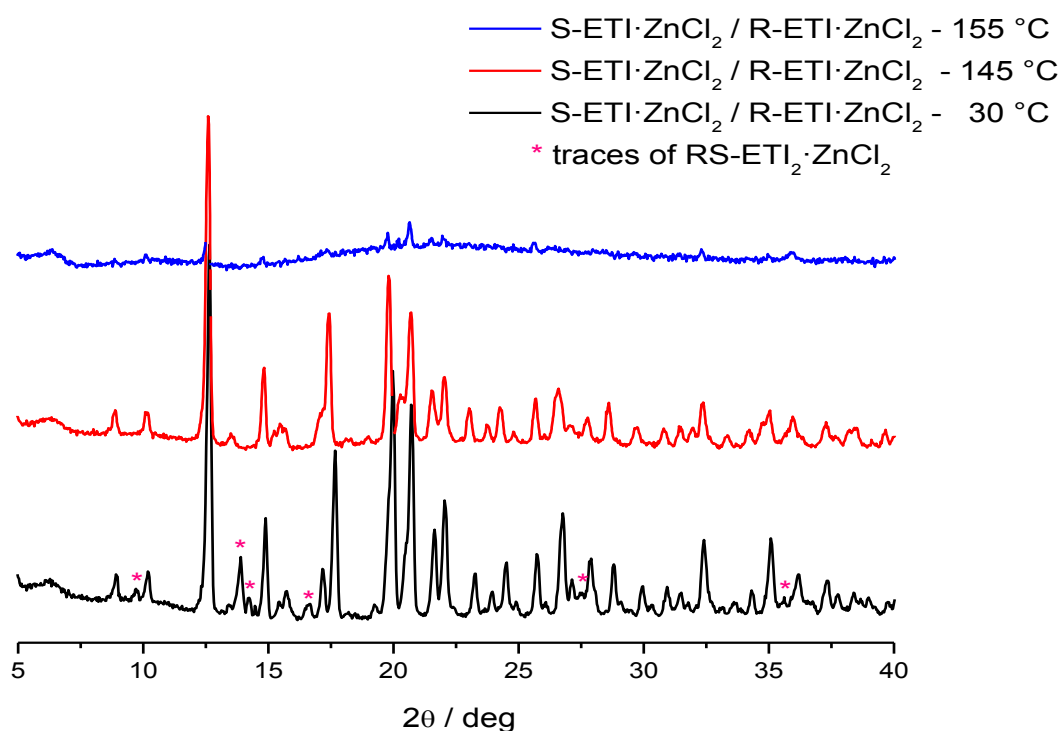


Fig. ESI-15. VT-XRPD for the *R*-ETI·ZnCl₂ / *S*-ETI·ZnCl₂ conglomerate. Some traces of *RS*-ETI₂·ZnCl₂ are present in the sample (the corresponding peaks are marked with asterisks). Upon reaching 145 °C the peaks of the racemic complex are not observed any longer in the diffractograms, whereas the conglomerates are still stable.

4. TPD for the *RS-ETI*:*ZnCl*₂:ethanol system.

To construct a TPD for the *RS-ETI*:*ZnCl*₂ system a series of physical mixtures of starting materials (200 mg of total weight) were prepared (see table ESI-2). To the obtained mixtures 0.35 mL of ethanol were added and slurry experiments performed at 25°C for 48h. The samples with the suspensions were seeded with both starting materials and with *RS-ETI*₂·*ZnCl*₂. Seeding material was prepared by kneading with ethanol (see synthesis).

Table ESI-2. Initial Experimental Data for System of *RS-ETI*:*ZnCl*₂:EtOH at 298 K. 200 mg of total weight of *RS-ETI*:*ZnCl*₂ in 0.35mL of EtOH.

Initial composition <i>RS-ETI</i> : <i>ZnCl</i> ₂ (%)	Initial components			Initial components (mol %)			Solid phase at equilibrium
	<i>RS-ETI</i> (mg)	<i>ZnCl</i> ₂ (mg)	EtOH (ml)	<i>RS-ETI</i>	<i>ZnCl</i> ₂	EtOH	
90:10	182.52	17.48	0.35	0.117	0.013	0.870	<i>RS-ETI</i> + <i>RS-ETI</i> ₂ · <i>ZnCl</i> ₂
80:20	164.55	35.45	0.35	0.105	0.026	0.868	<i>RS-ETI</i> + <i>RS-ETI</i> ₂ · <i>ZnCl</i> ₂
70:30	146.06	53.94	0.35	0.093	0.040	0.867	<i>RS-ETI</i> ₂ · <i>ZnCl</i> ₂
60:40	127.03	72.97	0.35	0.081	0.054	0.865	<i>RS-ETI</i> ₂ · <i>ZnCl</i> ₂
50:50	107.43	92.57	0.35	0.068	0.068	0.863	<i>RS-ETI</i> ₂ · <i>ZnCl</i> ₂
40:60	87.24	112.76	0.35	0.055	0.083	0.861	<i>RS-ETI</i> ₂ · <i>ZnCl</i> ₂ + <i>R-ETI</i> · <i>ZnCl</i> ₂ / <i>S-ETI</i> · <i>ZnCl</i> ₂
30:70	66.43	133.57	0.35	0.042	0.098	0.860	Dissolved
20:80	44.98	155.02	0.35	0.028	0.114	0.858	Dissolved
10:90	22.84	177.16	0.35	0.014	0.130	0.856	Dissolved

Taking into account the fact that the given quantity of starting materials completely dissolved in all the cases where the excess of ZnCl₂ was employed, the experiment was repeated using 500 mg of total weight and 0.3 mL of EtOH (see table ESI-3).

Table ESI-3. Initial Experimental Data for System of RS-ETI:ZnCl₂:EtOH at 298 K. 500 mg of total weight of RS-ETI:ZnCl₂ in 0.3mL of EtOH.

Initial composition RS-ETI:ZnCl ₂ (%)	Initial components			Initial components (mol %)			Solid phase at equilibrium
	RS-ETI (mg)	ZnCl ₂ (mg)	EtOH (mL)	RS-ETI	ZnCl ₂	EtOH	
90:10	456.31	43.69	0.3	0.314	0.035	0.652	RS-ETI ₂ ·ZnCl ₂ + RS-ETI
80:20	411.38	88.62	0.3	0.281	0.07	0.648	RS-ETI ₂ ·ZnCl ₂ + RS-ETI
70:30	365.15	134.85	0.3	0.248	0.106	0.645	RS-ETI ₂ ·ZnCl ₂ + RS-ETI
60:40	317.56	182.44	0.3	0.215	0.143	0.642	RS-ETI ₂ ·ZnCl ₂ + R-ETI·ZnCl ₂ /S-ETI·ZnCl ₂
50:50	268.57	231.43	0.3	0.181	0.181	0.638	RS-ETI ₂ ·ZnCl ₂ + R-ETI·ZnCl ₂ /S-ETI·ZnCl ₂
40:60	218.09	281.91	0.3	0.146	0.219	0.635	R-ETI·ZnCl ₂ /S-ETI·ZnCl ₂
30:70	166.07	333.93	0.3	0.111	0.258	0.631	R-ETI·ZnCl ₂ /S-ETI·ZnCl ₂
20:80	112.44	387.56	0.3	0.074	0.298	0.628	R-ETI·ZnCl ₂ /S-ETI·ZnCl ₂
10:90	57.11	442.89	0.3	0.038	0.338	0.624	Too little quantity of material to perform XRPD analysis

The solubility curve was determined by adding small portions of ethanol to the stirring mixtures every 30 minutes, until the suspended solids were completely dissolved (see table ESI-4).

Table ESI-4. Experimental Data for the Dissolution Points at 298 K

Initial composition <i>RS-ETI:ZnCl₂</i> (%)	EtOH initial (ml)	EtOH added (ml)	Composition at dissolution point			Composition at dissolution point (mol %)		
			<i>RS-ETI</i> (mg)	<i>ZnCl₂</i> (mg)	EtOH (mL)	<i>RS-ETI</i>	<i>ZnCl₂</i>	EtOH
100:0	0.3	3.95	500.00	0	4.25	0.042	0.000	0.958
90:10	0.3	2.95	456.31	43.69	3.25	0.049	0.005	0.946
80:20	0.3	3.55	411.38	88.62	3.85	0.038	0.009	0.953
70:30	0.3	3.75	365.15	134.85	4.05	0.032	0.014	0.955
60:40	0.3	3.95	317.56	182.44	4.25	0.026	0.018	0.956
50:50	0.3	2.3	268.57	231.43	2.6	0.035	0.035	0.929
40:60	0.3	1.2	218.09	281.91	1.5	0.047	0.071	0.882
30:70	0.3	0.7	166.07	333.93	1.0	0.051	0.119	0.830
20:80	0.3	0.5	112.44	387.56	0.8	0.059	0.235	0.707
10:90	0.3	0.1	57.11	442.89	0.4	0.035	0.311	0.655
0:100	0.3	0.2	0	500.00	0.5	0.000	0.300	0.700

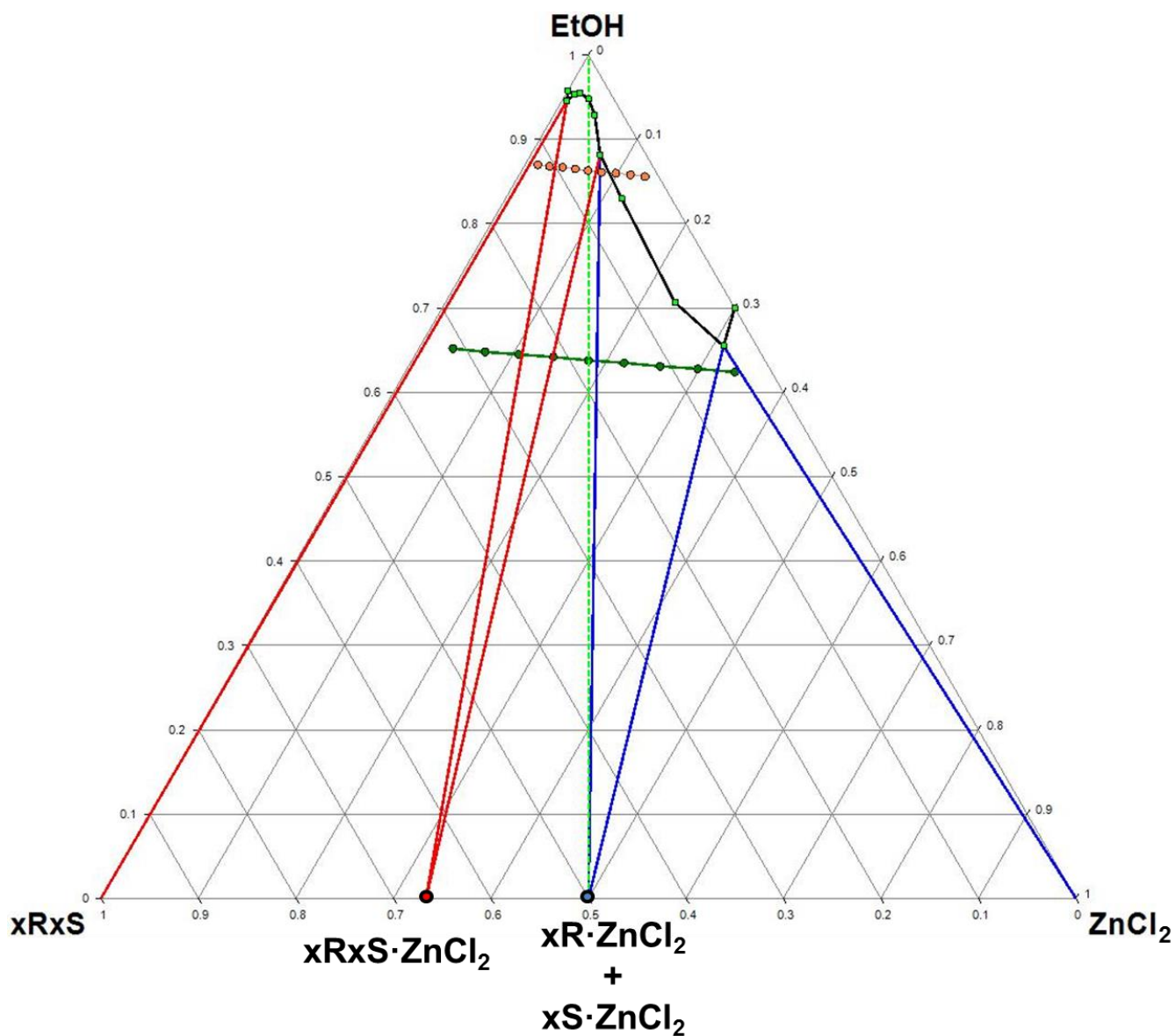


Fig. ESI-16. Complete ternary phase diagram for *RS*-ETI:ZnCl₂:EtOH at 298K (mol%). *RS* corresponds to R- and S-etiracetam correspondingly. *x* corresponds to the molecular ratio of R- and S-etiracetam.

3.5. References

1. D. Braga, F. Grepioni, L. Maini, S. Prosperi, R. Gobetto and M. R. Chierotti, *Chem. Commun.*, 2010, **46**, 7715-7717.
2. D. Braga, F. Grepioni and O. Shemchuk, *Crystengcomm*, 2018, **20**, 2212-2220.
3. S. Aitipamula, R. Banerjee, A. K. Bansal, K. Biradha, M. L. Cheney, A. R. Choudhury, G. R. Desiraju, A. G. Dikundwar, R. Dubey, N. Duggirala, P. P. Ghogale, S. Ghosh, P. K. Goswami, N. R. Goud, R. R. K. R. Jetti, P. Karpinski, P. Kaushik, D. Kumar, V. Kumar, B. Moulton, A. Mukherjee, G. Mukherjee, A. S. Myerson, V. Puri, A. Ramanan, T. Rajamannar, C. M. Reddy, N. Rodriguez-Hornedo, R. D. Rogers, T. N. G. Row, P. Sanphui, N. Shan, G. Shete, A. Singh, C. C. Sun, J. A. Swift, R. Thaimattam, T. S. Thakur, R. Kumar Thaper, S. P. Thomas, S. Tothadi, V. R. Vangala, N. Variankaval, P. Vishweshwar, D. R. Weyna and M. J. Zaworotko, *Cryst. Growth Des.*, 2012, **12**, 2147-2152.
4. N. K. Duggirala, M. L. Perry, O. Almarsson and M. J. Zaworotko, *Chem. Commun.*, 2016, **52**, 640-655.
5. S. Golob, M. Perry, M. Lusi, M. R. Chierotti, I. Grabnar, L. Lassiani, D. Voinovich and M. J. Zaworotko, *J. Pharm. Sci.*, 2016, **105**, 3626-3633.
6. A. R. Buist and A. R. Kennedy, *Cryst. Growth Des.*, 2014, **14**, 6508-6513.
7. N. K. Duggirala, A. J. Smith, L. Wojtas, R. D. Shytle and M. J. Zaworotko, *Cryst. Growth Des.*, 2014, **14**, 6135-6142.
8. J. Yao, J. M. Chen, Y. B. Xu and T. B. Lu, *Cryst. Growth Des.*, 2014, **14**, 5019-5025.
9. A. J. Smith, S. H. Kim, N. K. Duggirala, J. Jin, L. Wojtas, J. Ehrhart, B. Giunta, J. Tan, M. J. Zaworotko and R. D. Shytle, *Mol. Pharm.*, 2013, **10**, 4728-4738.
10. D. Braga, F. Grepioni, L. Maini, D. Capucci, S. Nanna, J. Wouters, L. Aerts and L. Quéré, *Chemical communications*, 2012, **48**, 8219-8221.
11. D. Braga, F. Grepioni, G. I. Lampronti, L. Maini and A. Turrina, *Crystal Growth & Design*, 2011, **11**, 5621-5627.
12. O. Shemchuk, D. Braga, L. Maini and F. Grepioni, *Crystengcomm*, 2017, **19**, 1366-1369.
13. A. J. Smith, S.-H. Kim, N. K. Duggirala, J. Jin, L. Wojtas, J. Ehrhart, B. Giunta, J. Tan, M. J. Zaworotko and R. D. Shytle, *Molecular pharmaceuticals*, 2013, **10**, 4728-4738.
14. K. Honer, E. Kalfaoglu, C. Pico, J. McCann and J. Baltrusaitis, *ACS Sustainable Chem. Eng.*, 2017, **5**, 8546-8550.
15. N. K. Duggirala, A. J. Smith, Ł. Wojtas, R. D. Shytle and M. J. Zaworotko, *Crystal Growth & Design*, 2014, **14**, 6135-6142.
16. H. Oertling, *CrystEngComm*, 2016, **18**, 1676-1692.
17. J. Wouters, F. Grepioni, D. Braga, R. M. Kaminski, S. Rome, L. Aerts and L. Quéré, *CrystEngComm*, 2013, **15**, 8898-8902.
18. D. Braga, L. Maini and F. Grepioni, *Chem. Soc. Rev.*, 2013, **42**, 7638-7648.
19. S. L. James, C. J. Adams, C. Bolm, D. Braga, P. Collier, T. Friscic, F. Grepioni, K. D. Harris, G. Hyett, W. Jones, A. Krebs, J. Mack, L. Maini, A. G. Orpen, I. P. Parkin, W. C. Shearouse, J. W. Steed and D. C. Waddell, *Chem. Soc. Rev.*, 2012, **41**, 413-447.
20. D. Braga, M. Cadoni, F. Grepioni, L. Maini and K. Rubini, *CrystEngComm*, 2006, **8**, 756-763.
21. M. R. Chierotti, L. Ferrero, N. Garino, R. Gobetto, L. Pellegrino, D. Braga, F. Grepioni and L. Maini, *Chem. Eur. J.*, 2010, **16**, 4347-4358.
22. M. U. Schmidt, J. Brüning, J. Glinnemann, M. W. Hützler, P. Mörschel, S. N. Ivashevskaya, J. van de Streek, D. Braga, L. Maini, M. R. Chierotti and R. Gobetto, *Angew. Chem. Int. Ed.*, 2011, **50**, 7924-7926.
23. M. R. Chierotti, K. Gaglioti, R. Gobetto, D. Braga, F. Grepioni and L. Maini, *CrystEngComm*, 2013, **15**, 7598.
24. L. Maini, D. Braga, F. Grepioni, G. I. Lampronti, K. Gaglioti, R. Gobetto and M. R. Chierotti, *CrystEngComm*, 2016, **18**, 4651-4657.
25. O. Shemchuk, D. Braga and F. Grepioni, *Chem. Commun.*, 2016, **52**, 11815-11818.

26. C. R. Groom, I. J. Bruno, M. P. Lightfoot and S. C. Ward, *Acta crystallographica Section B, Structural science, crystal engineering and materials*, 2016, **72**, 171-179.
27. P. R. Willmott, D. Meister, S. J. Leake, M. Lange, A. Bergamaschi, M. Boge, M. Calvi, C. Cancellieri, N. Casati, A. Cervellino, Q. Chen, C. David, U. Flechsig, F. Gozzo, B. Henrich, S. Jaggi-Spielmann, B. Jakob, I. Kalichava, P. Karvinen, J. Krempasky, A. Ludeke, R. Luscher, S. Maag, C. Quitmann, M. L. Reinle-Schmitt, T. Schmidt, B. Schmitt, A. Streun, I. Vartiainen, M. Vitins, X. Wang and R. Wulschleger, *J Synchrotron Radiat*, 2013, **20**, 667-682.
28. A. Bergamaschi, A. Cervellino, R. Dinapoli, F. Gozzo, B. Henrich, I. Johnson, P. Kraft, A. Mozzanica, B. Schmitt and X. Shi, *J Synchrotron Radiat*, 2010, **17**, 653-668.
29. T. Degen, M. Sadki, E. Bron, U. Konig and G. Nenert, *Powder Diffr.*, 2014, **29**, S13-S18.
30. A. Altomare, C. Cuocci, C. Giacobozzo, A. Moliterni, R. Rizzi, N. Corriero and A. Falcicchio, *J. Appl. Crystallogr.*, 2013, **46**, 1231-1235.
31. A. L. Spek, *Acta Crystallogr C Struct Chem*, 2015, **71**, 9-18.
32. A. Cohelo, *Journal*, 2007.
33. P. W. Stephens, *J. Appl. Crystallogr.*, 1999, **32**, 281-289.
34. K. Momma and F. Izumi, *J. Appl. Crystallogr.*, 2011, **44**, 1272-1276.
35. E. Keller, *University of Freiburg, Germany*, 1999.
36. C. F. Macrae, I. J. Bruno, J. A. Chisholm, P. R. Edgington, P. McCabe, E. Pidcock, L. Rodriguez-Monge, R. Taylor, J. van de Streek and P. A. Wood, *J. Appl. Crystallogr.*, 2008, **41**, 466-470.
37. O. Shemchuk, Optimizing physicochemical properties of natural antioxidants and geroprotectors: L-carnosine and melatonin, 2015.
38. G. A. Burdock and I. G. Carabin, *Toxicol. Lett.*, 2004, **150**, 3-18.
39. O. Shemchuk, V. Andre, M. T. Duarte, P. Taddei, K. Rubini, D. Braga and F. Grepioni, *Cryst. Growth Des.*, 2017, **17**, 3379-3386.
40. N. Schultheiss and A. Newman, *Cryst. Growth Des.*, 2009, **9**, 2950-2967.
41. R. Thakuria, A. Delori, W. Jones, M. P. Lipert, L. Roy and N. Rodríguez-Hornedo, *Int. J. Pharm.*, 2013, **453**, 101-125.
42. J. W. Steed, *Trends Pharmacol. Sci.*, 2013, **34**, 185-193.
43. G. Bolla and A. Nangia, *Chem. Commun.*, 2016, **52**, 8342-8360.
44. C. B. Aakeroy, M. E. Fasulo and J. Desper, *Mol. Pharm.*, 2007, **4**, 317-322.
45. J. F. Remenar, S. L. Morissette, M. L. Peterson, B. Moulton, J. M. MacPhee, H. R. Guzmán and Ö. Almarsson, *J. Am. Chem. Soc.*, 2003, **125**, 8456-8457.
46. M. B. Hickey, M. L. Peterson, L. A. Scoppettuolo, S. L. Morrisette, A. Vetter, H. Guzman, J. F. Remenar, Z. Zhang, M. D. Tawa, S. Haley, M. J. Zaworotko and O. Almarsson, *Eur. J. Pharm. Biopharm.*, 2007, **67**, 112-119.
47. S. Basavoju, D. Bostrom and S. P. Velaga, *Pharm. Res.*, 2008, **25**, 530-541.
48. N. Variankaval, R. Wenslow, J. Murry, R. Hartman, R. Helmy, E. Kwong, S.-D. Clas, C. Dalton and I. Santos, *Cryst. Growth Des.*, 2006, **6**, 690-700.
49. M. K. Stanton and A. Bak, *Cryst. Growth Des.*, 2008, **8**, 3856-3862.
50. D. Braga, L. D. Esposti, K. Rubini, O. Shemchuk and F. Grepioni, *Cryst. Growth Des.*, 2016, **16**, 7263-7270.
51. O. Shemchuk, L. D. Esposti, F. Grepioni and D. Braga, *Crystengcomm*, 2017, **19**, 6267-6273.
52. O. Shemchuk, B. K. Tsenkova, D. Braga, M. T. Duarte, V. Andre and F. Grepioni, *Chem. Eur. J.*, 2018, **24**, 12564-12573.
53. C. Rodriguez, J. C. Mayo, R. M. Sainz, I. Antolin, F. Herrera, V. Martin and R. J. Reiter, *J. Pineal Res.*, 2004, **36**, 1-9.
54. E. Varoni, C. Soru, R. Pluchino, C. Intra and M. Iriti, *Molecules*, 2016, **21**, 240.
55. Y. Yan, J.-M. Chen and T.-B. Lu, *CrystEngComm*, 2015, **17**, 612-620.
56. V. N. Anisimov, I. G. Popovich, M. A. Zabezhinski, S. V. Anisimov, G. M. Vesnushkin and I. A. Vinogradova, *Biochim. Biophys. Acta*, 2006, **1757**, 573-589.
57. R. J. Reiter, D. X. Tan, C. Osuna and E. Gitto, *J. Biomed. Sci.*, 2000, **7**, 444-458.

58. A. Korkmaz, R. J. Reiter, T. Topal, L. C. Manchester, S. Oter and D. X. Tan, *Mol. Med.*, 2009, **15**, 43-50.
59. A. Carrillo-Vico, J. M. Guerrero, P. J. Lardone and R. J. Reiter, *Endocrine*, 2005, **27**, 189-200.
60. N. Buscemi, B. Vandermeer, R. Pandya, N. Hooton, L. Tjosvold, L. Hartling, G. Baker, S. Vohra and T. Klassen, *Evid. Rep. Technol. Assess.*, 2004, **108**, 1-7.
61. http://ec.europa.eu/health/scientific_committees/consumer_safety/docs/sccs_o_022.pdf.
62. B. J. Lee, H. G. Choi, C. K. Kim, K. A. Parrott, J. W. Ayres and R. L. Sack, *Arch. Pharm. Res.*, 1997, **20**, 560-565.
63. A. Boultif and D. Louer, *J. Appl. Crystallogr.*, 2004, **37**, 724-731.
64. G. M. Sheldrick, *Acta Crystallographica Section A Foundations and Advances*, 2015, **71**, 3-8.
65. G. M. Sheldrick, *Acta Crystallographica Section C Structural Chemistry*, 2015, **71**, 3-8.
66. A. L. Spek, *Acta Crystallogr. Sect. D Biol. Crystallogr.*, 2009, **65**, 148-155.
67. T. Wada, E. Kishida, Y. Tomiie, H. Suga, S. Seki and I. Nitta, *Bull. Chem. Soc. Jpn.*, 1960, **33**, 1317-1318.
68. A. Parkin, I. D. H. Oswald and S. Parsons, *Acta Crystallographica Section B Structural Science*, 2004, **60**, 219-227.
69. P. A. Agron and W. R. Busing, *Acta Crystallographica Section C-Crystal Structure Communications*, 1986, **42**, 141-143.
70. O. Shemchuk, L. Song, K. Robeyns, D. Braga, F. Grepioni and T. Leyssens, *Chem. Commun.*, 2018, **54**, 10890-10892.
71. O. V. Dolomanov, L. J. Bourhis, R. J. Gildea, J. A. K. Howard and H. Puschmann, *J. Appl. Crystallogr.*, 2009, **42**, 339-341.
72. C. F. Macrae, P. R. Edgington, P. McCabe, E. Pidcock, G. P. Shields, R. Taylor, M. Towler and J. van De Streek, *Journal of Applied Crystallography*, 2006, **39**, 453-457.
73. H. G. Brittain, *Journal*, 2009, **162**.

4. SUMMARY

The aim of this project was to synthesize new multicomponent materials with improved physicochemical properties. The research activity was mainly dedicated to the investigations of solid solutions formed by organic molecules and of molecular and ionic co-crystals. The whole project can be subdivided in three main directions:

1. Investigation of solid solutions consisting of organic molecules.
2. Co-crystallization as a tool to modify physicochemical properties of interest.
3. The effect of co-crystallization on chirality and its possible application for chiral resolution.

4.1. Investigation of solid solutions consisting of organic molecules

The first part of my PhD thesis was dedicated to the investigation of the crystalline solid solutions or organic alloys formed by barbituric and thiobarbituric acids. Initially, a 1 to 1 molecular co-crystal of these acids was obtained. The variation of the stoichiometric ratios of the starting materials resulted in the formation of new crystalline materials – solid solutions ($\text{BA}_x\text{TBA}_{1-x}$, $x < 0.8$). Thus, barbituric and thiobarbituric acids were found to be mutually miscible. All these mixed crystals were isomorphous with those of the parent components and were characterized by a structural disorder of carbonyl and thiocarbonyl groups that permitted the variation of the ratios of their

components. Generally, the BA:TBA solid system was found to be an intriguing system: the crystal packing of the obtained co-crystal was more favoured with respect to the parent homo-molecular crystalline materials. DSC traces of the BA_xTBA_{1-x} solid solutions with an excess of thiobarbituric acid showed that the obtained solids were not stable upon heating: the melting of BA and TBA followed by recrystallization to the BA·TBA co-crystal was observed. Moreover, the melting point of the BA·TBA co-crystal was found to be higher than those of both barbituric and thiobarbituric acids. Therefore, it was concluded that the co-crystal was more thermally stable compared to the parent components. As a matter of fact, this phenomenon is not common since typically the co-crystals' melting points are either in between or lower than those of the starting materials.

4.2. Co-crystallization as a tool to modify physicochemical properties of interest.

This part of my research was dedicated to the synthesis and characterization of molecular and ionic co-crystals. The investigation began with the co-crystallization of cyanuric acid with alkali metal halides. The kneading of equimolar quantities of cyanuric acid with the majority of the tested inorganic salts resulted into formation of ionic co-crystals. The structures of the obtained crystalline solids were solved using XRPD data. Almost all the obtained ionic co-crystals are anhydrous. The co-crystallization of cyanuric acid with sodium chloride resulted in the formation of CA·NaCl. In view of the interest in increasing the solubility of cyanuric acid in water this co-crystal was chosen to test both the intrinsic dissolution rate (the rate at which the compound is released from its crystal lattice into solution) and the thermodynamic solubility.

The latter showed a dramatic difference: it was possible to dissolve about 20 times more cyanuric acid in the form of CA·NaCl with respect to the pure organic compound. The positive effect on the intrinsic dissolution rate of the ICC compared to cyanuric acid itself was also detected though it was not that impressive.

The following step of my investigation was an attempt to co-crystallize hormone melatonin aimed at improvement of its solubility in water. Despite the fact that a number of co-formers were used only three co-crystals of melatonin were obtained: two molecular and one ionic. The latter was obtained by the co-crystallization with calcium chloride and, in principle, it is of higher importance since it was obtained with the co-former that belongs to the GRAS list. The thermodynamic solubility measurements showed that ionic co-crystal formation with CaCl₂ significantly improved the solubility in water.

4.3. The effect of co-crystallization on chirality and its possible application for chiral resolution.

This part of the research combines the issue of chirality with that of ionic co-crystal formation. Initially, we planned to investigate the influence of ICCs formation on the crystal structure of chiral molecules. To this end, both enantiopure and racemic amino acid histidine was co-crystallized with lithium and calcium halides. The results of this research showed that the complexation of DL-histidine by lithium cations was enantioselective: the tetrahedral assembly around the cations favoured molecules of the same handedness. As a result, infinite enantiopure (L-His·Li)_nⁿ⁺ / (D-His·Li)_nⁿ⁺ chains are formed. Moreover, while the co-crystallization of DL-histidine with lithium chloride and bromide resulted into formation of the corresponding racemic ICCs, the

reaction lithium iodide proceeded a step further along the path towards chiral separation: spontaneous chiral resolution took place with the formation of conglomerate of D-His·LiI·H₂O and L-His·LiI·H₂O. In addition to this, it was established that the enantiopure chains observed in both racemic and conglomerate crystals were identical.

The co-crystallization with calcium halides, in turn, did not show any effect on the chirality of the obtained ionic co-crystals. The interaction of both racemic and enantiopure histidine resulted into formation of the corresponding ionic co-crystals of the general formula (L-His)₂·CaX₂·nH₂O (X= Cl and Br n=3, X= I n=4). The co-crystallization of the racemic histidine with calcium halides resulted into the corresponding racemic ICCs which accommodated molecules of both chiralities in the coordination sphere of the Ca²⁺ cations.

Taking in consideration the information obtained by the co-crystallization histidine with lithium and calcium halides, it was speculated that the Li⁺ tetrahedral coordination could be the key factor in the lithium homochiral preference. To put this theory to test, it was decided to co-crystallize lithium halides with another amino acid – proline. It was also planned to investigate was the possible role of the anion in the chiral resolution since different results were obtained via co-crystallization of DL-histidine with LiCl, LiBr and LiI. The co-crystallization of both enantiopure and racemic proline with lithium halides showed similar behaviour to that previously observed in histidine ICCs. Once again in all the cases lithium showed a preference towards amino acids of the same chirality. However, this time we could observe conglomerate formation in the reactions of DL-proline with lithium chloride and bromide while the co-crystallization with lithium iodide led to the formation of the racemic ICC. Later on, a racemate was also obtained with LiCl in one of the trials to recrystallize conglomerate D-Pro·LiCl·H₂O and L-Pro·LiCl·H₂O. These results allowed us to

exclude the role of the anion as a key factor in the spontaneous chiral resolution. Since the majority of ICCs were obtained in the form of hydrates, the thermal behaviour of the products and its impact on the chirality were also investigated. It was found that all the obtained ICCs could be dehydrated. The structure of the obtained ICCs was solved using XRPD data. The enantioselective complexation of proline by lithium cations was retained in the dehydration products. The dehydration of all ICCs was reversible: upon standing at open air the ICCs quickly rehydrated back. The dehydration process retained the racemate/conglomerate choice for the ICCs formed with lithium chloride and iodide, but swapped to the racemate structure when formed with lithium bromide.

Taking into account the information of the co-crystallization results of amino acids histidine and proline with lithium and calcium halides it was speculated that the lithium homochiral preference could be caused by the tetrahedral geometry around lithium cations that could favour the coordination of molecules of the same chirality. To find it out an antiepileptic drug – levetiracetam and its racemic intermediate – *RS*-etiracetam were co-crystallized with $ZnCl_2$ since zinc is known to favour tetrahedral coordination. The complexation of *RS*-etiracetam to zinc cations was also enantioselective. In addition, it was possible to switch from a thermodynamically stable racemic compound to a thermodynamically stable conglomerate using different amounts of zinc chloride.

In conclusion, I would like to say that the obtained results emphasized the fact that co-crystallization with metal ions favouring tetrahedral coordination could be successfully used to obtain chiral selectivity and conglomerate formation from racemic compounds.

ACKNOWLEDGMENT

I would like to express my sincere gratitude to my supervisor—**Prof. Fabrizia Grepioni**, for her full support, expert guidance, understanding and encouragement throughout this project. Actually, this thesis has become a reality with the kind assistance and help of many individuals – **Lorenzo Degli Esposti** and **Boryana Tsenkova** who were working in our research group, **Prof. Teresa Duarte** and **Dr. Vânia André** from the University of Lisbon; **Lixing Song** and **Prof. Tom Leysens** from the Université catholique de Louvain.

My heartfelt gratitude to the whole group of Molecular Crystal Engineering: to **Prof. Dario Braga** for his undying support and inspiration, to **Prof. Lucia Maini** for her kind assistance with structure solution from XRPD, to **Dr. Simone D'Agostino** and to all the PhD students who were or still are working in our research group.

In addition, I express my appreciation to **Dr. Katia Rubini** for her kind assistance with TGA and DSC experiments.

Finally, I would like to thank my family for unconditional love and support. I would not have been able to complete this thesis without their continuous love and encouragement.

I am grateful to COST Action CM1402 Crystallize and to the University of Bologna.